ALMA MATER STUDIORUM · UNIVERSITY OF BOLOGNA

School of Science
Department of Physics and Astronomy
Master Degree in Physics

Fast simulation of the MUonE 2021 Test Run setup

Supervisor: **Submitted by:**

Prof. Domenico Galli   **Eugenia Spedicato**

Co-supervisor:

Dr. Giovanni Abbiendi
Dr. Umberto Marconi

Academic Year 2019/2020

Che cosa sono i fiori?
non senti in loro come una vittoria?
la forza di chi torna
da un altro mondo e canta
la visione. L'aver visto qualcosa
che trasforma
per vicinanza, per adesione a una legge
che si impara cantando, si impara profumando.
Che cosa sono i fiori se non qualcosa d'amore
che da sotto la terra viene
fino alla mia mano
a fare la festa generosa.
Che cosa sono se non
leggere ombre a dire
che la bellezza non si incatena
ma viene gratis e poi scema, sfuma
e poi ritorna quando le pare.
Chi li ha pensati i fiori,
prima, prima dei fiori..

(Senza polvere e senza peso, *Mariangela Gualtieri)*

Abstract

Questa tesi contribuisce allo studio delle prestazioni e a chiarire le possibilità di impiego del calorimetro elettromagnetico per la selezione degli eventi di collisione elastica fra muoni ed elettroni nell'esperimento MUonE. Assieme al sistema di tracciamento il calorimetro costituisce il rivelatore prototipo che sarà utilizzato nel Test Run in programma nel 2021 (TR2021). Il lavoro di tesi ha avuto per obiettivo lo sviluppo del codice di simulazione rapida della risposta del calorimetro, nelle condizioni di misura previste nel TR2021. A partire da eventi di collisione fra muoni di alta energia ed elettroni a riposo, generati in approssimazione NLO, in condizioni cinematiche prefissate, si è sviluppata la procedura che generalizza le condizioni cinematiche di collisione considerando le proprietà cinematiche del fascio: la sua divergenza angolare e la dispersione spaziale o larghezza (beam spot). Gli eventi NLO includono il caso di urto con radiazione di un fotone reale. Si è quindi proceduto allo sviluppo della procedura di propagazione delle particelle nei bersagli sottili e nei volumi del tracciatore (tracker), considerando gli effetti di deflessione delle traiettorie dovuti alla diffusione coulombiana multipla, fino all'arrivo di elettroni, muoni e fotoni irradiati sulla superficie del calorimetro. Per simulare la risposta del calorimetro si è quindi fatto ricorso ad un modello parametrico di sviluppo degli sciami elettromagnetici (fast simulation). L'algoritmo di fast simulation è stato realizzato riferendosi alla parametrizzazione dello sviluppo degli sciami elettromagnetici GFLASH utilizzata nell'esperimento CMS. Il codice di simulazione è stato collaudato con successo, confrontando i risultati ottenuti con quelli attesi, pubblicati dagli autori del modello. È stata quindi studiata la distribuzione dell'energia rilasciata dalle particelle nelle unità sensibili, o celle, del calorimetro. Successivamente, i due codici di simulazione, quello che permette di simulare la propagazione delle particelle nel rivelatore, e quello che consente di simulare la risposta rapida del calorimetro, sono stati integrati in un programma di calcolo con cui è stato possibile realizzare uno studio completo e dettagliato delle caratteristiche degli eventi che ci si aspetta possano essere registrati durante il TR2021. Il programma di simulazione ha consentito di individuare criteri per la selezione degli eventi elastici tra quelli NLO. Sono stati individuati tre diversi criteri di selezione degli eventi, che sembrano consentire una selezione degli eventi d'interesse con elevata efficienza. I criteri sono basati esclusivamente sulle informazioni ottenibili grazie al calorimetro: l'energia ricostruita dello sciame e la posizione del centroide di energia. La tesi chiarisce, almeno in parte, il ruolo prezioso che questo strumento potrà avere nell'esperimento finale.

Abstract

This thesis contributes to the study of the electromagnetic calorimeter performances and to the clarification of its role in the selection of $\mu - e$ elastic scattering events for the MUonE experiment. Together with the tracking system, the calorimeter constitutes the prototype detector for the Test Run scheduled in 2021 (TR2021). One of the main proposals of this thesis is the development of the fast simulation code for the calorimeter response, in the working condition expected in the TR2021. Given a generated set of NLO events, consisting in high energy muons scattering on electrons at rest with prefixed kinematical conditions, it has been developed the procedure which generalizes kinematical scattering conditions considering the kinematical properties of the beam: its angular divergence and its spatial profile (beam spot). NLO events include the case of one real photon radiation. It has been simulated the propagation of particles across light targets and tracking stations, considering the deflection given by multiple Coulomb scattering, until electrons, muons and photons have reached the calorimeter surface. The response of the calorimeter has been simulated by means of a fast simulation algorithm that has been developed relying on an existing parametrization (GFLASH) also used by CMS. The simulation code has been validated successfully, comparing the obtained results with the expected ones, published by the authors of the model. Thus, it has been studied the distribution of the energy released by particles in sensitive units, or cells, of the calorimeter. As a next step, the two simulation codes (the one for the propagation of particles throughout the detector and the one for the calorimeter response) were unified in a single algorithm, through which a complete study of the events topology expected in the TR2021 was carried out. This fast simulation tool enabled to identify selection criteria for elastic events within the full NLO set. Three different criteria were proposed which seem to identify efficiently the interesting events. Selections are mainly based on calorimetric information: the reconstructed shower energy and the centroid position of the cluster. The thesis clarifies, at least in part, the precious role that this detector may have in the final experiment.

Contents

Introduction

It is an incredible fact that a single number can hide a hint on how nature works. The anomalous magnetic moment of the muon $a_\mu = (g-2)/2$ represents one of the open questions in the nowadays physics scenario as the experimental measurement and the theoretical prediction differ of 3.7σ. The E821 experiment at Brookhaven reports the most precise measurement of the anomaly [18], while the theoretical estimation is reported in [13]:

$$a_\mu^{exp} = 116592089\,(63) \times 10^{-11} \quad \text{and} \quad a_\mu^{SM} = 116591810\,(43) \times 10^{-11}. \tag{1}$$

In some months a new result should be announced from the E989 experiment at Fermilab which aims at a precision of 0.14 ppm, a fourfold improvement over the 0.54 ppm achieved from Brookhaven. On the theoretical side, the biggest uncertainty is given by the hadronic vacuum polarization contribution to the anomaly at leading order a_μ^{HLO}. Until now, its calculation has been carried out with a data-driven approach based on the measurement of the hadronic $e^+ - e^-$ cross section in the time-like region. But this method seems to have reached its precision limit and new approaches are needed. In this context, the MUonE collaboration proposes an independent estimation of a_μ^{HLO} from a precise measurement of the hadronic contribution to the running of the QED coupling in the space-like region $\Delta\alpha_{had}(t)$. The selected process is the $\mu-e$ elastic scattering and the experiment will take place at CERN exploiting the available M2 muon beam of 150 GeV. After an introduction of the theory predictions and experimental measurements in Chapter 1, Chapter 2 introduces and explains the proposal and the main problems concerning the MUonE project. In Chapter 3 the original work of the thesis starts with the description of the simulation code for the Test Run 2021 setup. The kinematical properties of the beam are taken into account and applied to the generated MC NLO events before being propagated in the experimental setup. In Chapter 4 it is described how the fast simulation for EM showers was developed. The parametrization is the one proposed in [36] and also used in CMS.The code has been validated and gives consistent results with the CMS reference. The final Chapter 5 shows results obtained by merging the two fast simulation tools and aims to demonstrate how the calorimeter can take an important role in the selection of elastic events discarding the radiative ones.

Chapter 1

Introduction on the Muon and its Anomaly

1.1 An historical overview

In 1936 Carl D. Anderson and Seth Neddermeyer discovered a new particle as a constituent of cosmic-ray showers through a cloud chamber measurement; those data were commented by them in 1937 [1] as

> "the first experimental evidence for the existence of particles of both penetrating and non-penetrating character [...]. Moreover, the penetrating particles in this range do not ionize perceptibly more than the non-penetrating ones, and cannot therefore be assumed to be of protonic mass. [...] The non-penetrating particles are readily interpreted as free positive and negative electrons. Interpretations of the penetrating ones encounter very great difficulties, but at present appear to be limited to the following hypotheses: (a) that an electron (+ or −) can possess some property other than its charge and mass which is capable of accounting for the absence of numerous large radiative losses in a heavy element; or (b) that there exist particles of unit charge, but with a mass (which may not have a unique value) larger than that of a normal free electron and much smaller than that of a proton"

The existence of such a particle was confirmed in 1937 by J.C. Street and E.C. Stevenson, in particular they supported the idea that these were "particles of electronic charge, and of mass intermediate between those of the proton and electron[...]".
Because of its mass, many physicists at that time believed that this new entity could be related to the one theoretically predicted by Yukawa in 1935: the *mesotron* (shortened as *meson*), mediator of the strong nuclear forces.
But, in 1946, an important experiment by M. Conversi, E. Pancini and O. Piccioni [3] shown that those *mesons* were not affected by the nuclear force, being unreactive in the nuclear sense, thus could not correspond to the Yukawa's hypothesis. His predicted

particle, nowadays known as π meson, was finally identified in 1947 by C. Lattes, G. Occhialini and C. F. Powell in a cosmic-ray experiment [4]. They discovered that in some cases an object that appeared to be a meson would stop and then emit another particle of somewhat lower mass. Hence the origin of cosmic ray muons became clear: the majority of π mesons, entering the atmosphere, decay into muons which are able to reach the Earth's surface; with this discovery they managed to differentiate the Yukawa particle, denominated *pion*, from the earlier-discovered *muon*.

After this puzzling path towards a deeper knowledge of that particle, physicists believed that the muon was just the heavier copy of the electron and this remained the feeling until precise measurements of the so-called *anomalous magnetic moment* were performed.
Nowadays muons are classified as leptons in the framework of the Standard Model, a model for the strong, electromagnetic and weak interactions of elementary particles. Leptons are particles of half-integer spin, existing in three generations

$$L_e = \begin{pmatrix} \nu_e \\ e^- \end{pmatrix}_L \quad L_\mu = \begin{pmatrix} \nu_\mu \\ \mu^- \end{pmatrix}_L \quad L_\tau = \begin{pmatrix} \nu_\tau \\ \tau^- \end{pmatrix}_L, \tag{1.1}$$

together withe their correspondent antiparticle. The doublets are composed by one neutral lepton (neutrinos ν) and a charged lepton (electron e, muon μ, tau τ). What really differentiate the three charged leptons is the mass value: $m_e = 0.511$ MeV, $m_\mu = 105.658$ MeV and $m_\tau = 1776.86$ MeV. This is the key parameter which brings to the different behaviors and characteristics of these fermions.
The electron can be studied most precisely because of its stability, but nowadays also the muon can be managed quite well in experiments and it reveals to be a good leptonic candidate for the discovery of physics beyond the Standard Model. Some effects scale with powers of m^2, therefore the τ is the most sensible lepton for this kind of researches but, being more massive, is less stable than the muon.

1.2 Magnetic Moments

The main subject of this thesis work is a specific muon observable, namely its *anomalous magnetic moment*. This quantum property can be described in Quantum Field Theory and is a powerful probe of physics beyond the Standard Model.
In classical mechanics, an electric charge e with mass m orbiting in a magnetic field $\vec{B}$ carries a magnetic dipole moment defined as

$$\vec{\mu}_L = \left(\frac{e}{2m} \right) \vec{L} \tag{1.2}$$

where $\vec{L} = m\vec{r} \times \vec{v}$ is the orbital angular momentum. Because of the magnetic moment, the magnetic field $\vec{B}$ induces a mechanical action on the charge through a torque:

$$\vec{M} = \vec{\mu} \times \vec{B}. \tag{1.3}$$

After Stern-Gerlach experiment in 1922 [6], *spinning* particles, in particular electrons, were proposed in 1925 by G. Uhlenbeck and S. Goudsmit as a necessary request for the explanation of the anomalous Zeeman effect [5]. An *intrinsic* magnetic moment was defined for all of them, where the orbital angular momentum $\vec{L}$ would be replaced by the quantum angular momentum called spin $\vec{S} = \frac{\hbar}{2}\vec{\sigma}$, bringing to

$$\vec{\mu}_s = g_s \left(\frac{e}{2m}\right) \vec{S} = g_s \frac{\mu_B}{\hbar} \vec{S}. \tag{1.4}$$

which is usually defined in terms of *Bohr magneton*

$$\mu_B = \frac{e\hbar}{2m}. \tag{1.5}$$

The equation introduces the so-called *dimensionless gyromagnetic ratio* g_s, linked to the spin, which needed to assume the value of 2 in order to explain the observations. This number plays a key role in the development of the research on the *anomalous magnetic moment*.

When in 1928 Dirac presented its famous theory of the electron [7], the picture became clearer. The relativistic equation for an electron in an external magnetic field takes the form:

$$(i\partial_\mu - eA_\mu)\gamma^\mu \psi = m\psi \tag{1.6}$$

and the extraordinary result was that the g value came out to be equal to 2, consistently with the value measured in earlier experiments, and directly as a natural consequence of his relativistic equation, such that Dirac himself stated that its theory "gave just the properties that one need for an electron. That was an unexpected bonus" for him, "completely unexpected".

This theoretical prediction was then supported by many measurements although with large experimental errors. It required 20 years of experimental efforts to establish that the electron's magnetic moment exceeds the value of 2 by a tiny fraction. As a matter of fact, in 1947 J. Schwinger [8] showed that from a theoretical point of view these "discrepancies can be accounted for by a small additional electron spin magnetic moment" that arises from the lowest-order radiative correction to the Dirac moment. Hence, the "interaction of an electron with an external field is now subjected to a finite radiative correction". His famous QED calculation predicted the one loop radiative contribution to a_e, shown diagrammatically in Fig. (1.1)

$$a_e = \frac{\alpha}{2\pi} \sim 0.00116 \qquad \rightarrow \qquad g_e^{th} = 2 \cdot 001161 \tag{1.7}$$

which is independent from any mass and equal for both a_μ and a_τ. What he remarked was that, in the process of the production of these results, mass and charge renormalization must be applied.

In the same year, this deviation was experimentally confirmed by Kusch and Foley [9], measuring:

$$g_e^{exp} = 2 \cdot (1.00119 \pm 0.00005). \tag{1.8}$$

This result was in agreement with Schwinger's prediction and became one of the first QED triumphs, as a confirmation of the perturbative method.

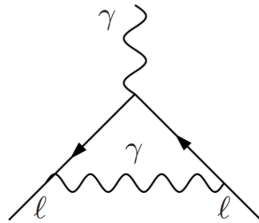It turned out to be convenient to divide the magnetic moment into two parts:

Figure 1.1: Lowest order QED contribution to the electron anomalous magnetic moment calculated by Schwinger (with $l = e$).

$$\mu = (1 + a)\frac{e\hbar}{2m} \tag{1.9}$$

where the first term is the Dirac term while the second is the anomalous Pauli moment, or anomalous magnetic moment. The so-called *anomaly*, defined as:

$$a = \frac{g - 2}{2}. \tag{1.10}$$

quantifies the discrepancy of the g factor from the Dirac predicted value of 2, hence it accounts for all the corrections which need to be applied to the magnetic moment.

1.3   Renormalization, running constants and QED

In Quantum Electrodynamics (QED) calculations can be performed by a perturbation method, based on Feynman diagrams, at subsequent orders of series expansion in powers of the coupling constant. In doing so, one of the main problems is the appearance of many divergent quantities.

Infinities come from the integration over variables (as the momenta of virtual particles)

that are not directly measurable and can therefore reach extremely high or low values. These integrals are generally ill-defined and one can try to put one or more cutoffs on the integration domain and perform a limit to remove them only at the very end of the calculation. If the diagram contribution diverges sending the cutoffs to infinity or to zero, one says that the diagram has respectively an ultraviolet or an infrared divergence. The procedure to actually renormalize a theory, trying to get rid of these infinities, involves a set of advanced mathematical techniques. The basic points are:

1. *Regularization*: The infinities are removed with a suitable technique, that can consist in the introduction of a cutoff Λ.

2. *Redefinition of parameters*: One redefines a finite number of parameters to absorb the infinities. In this process a mass scale μ, called renormalization scale, is introduced.

The infinities of the theory end up in the so-called **bare** parameters, which are those in the absence of vacuum interactions, instead what can be measured are the renormalized or dressed parameters shielded by polarized virtual electron/positron pairs at a given energy scale. The effect on the electron charge is shown in Fig.(1.2): the effective charge results from the shielding of virtual electron-positron pairs, the so-called Vacuum Polarization Effect (VP).
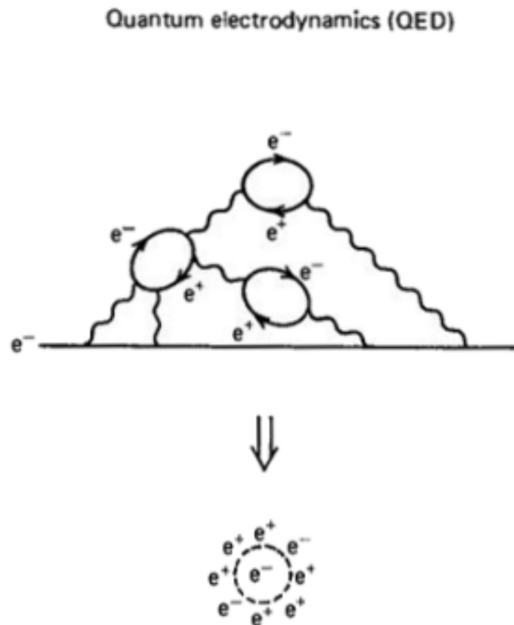

Figure 1.2: Screening of the electric charge in Quantum Field Theory. Feynman's diagrams for the creation of virtual particles are also shown on top.

As a consequence, the physical coupling is not constant: its value depends on the energy scale/distance of the process in which we probe the particle. This phenomenon

is a general feature of quantum field theories known as **running of the coupling constants**. It can be described quantitatively starting from the so-called beta function:

$$\beta(g) = \left(\frac{\mathrm{d}g}{\mathrm{d}\ln\mu} \right) \xrightarrow{QED} \beta(e) = \frac{e^3}{12\pi^2} \tag{1.11}$$

where g is the effective charge of the theory and μ the energy scale. $\beta(e)$ is the one-loop QED beta function taking as the effective parameter the electric charge e. In this theory, the coupling constant is defined as $\alpha_{qed} = e^2/4\pi$ hence, alter some mathematical steps, it is possible to get an equation for $\alpha_{qed} = \alpha$ from (1.11):

$$\frac{\mathrm{d}\alpha}{\mathrm{d}\ln\mu^2} = \frac{\alpha^2}{3\pi}, \tag{1.12}$$

in order to get the running of the parameter we need to integrate considering an arbitrary scale q_0

$$\int_{\alpha(q_0^2)}^{\alpha(q^2)} \frac{1}{\alpha^2} \mathrm{d}\alpha = \int_{q_0}^{q} \frac{1}{3\pi} \mathrm{d}\ln\mu^2$$

$$\frac{1}{\alpha(q^2)} - \frac{1}{\alpha(q_0^2)} = -\frac{1}{3\pi} \ln\left(\frac{q^2}{q_0^2}\right) \tag{1.13}$$

hence the running of the electromagnetic coupling caused by vacuum polarization results in

$$\alpha(q^2) = \frac{\alpha(q_0)}{1 - \frac{\alpha(q_0)}{3\pi} \ln\left(\frac{q^2}{q_0^2}\right)} \tag{1.14}$$

The closer one gets (increasing the energy scale q is equivalent to probing a smaller distance scale), the greater the observed effect of the virtual processes which modify the electric charge. Therefore the electromagnetic coupling *runs*, in particular it increases with energy.

This procedure gives a form of the running coupling constant in the one-loop approximation (Fig. (1.3)) as a result of the renormalization process based on the existence of VP processes.

Contributions to the vacuum polarization loops are given by all charged leptons and quarks, hence it is convenient to express the running of the coupling constant in this way

$$\alpha(q^2) = \frac{\alpha}{1 - \Delta\alpha(q^2)} \tag{1.15}$$

where $\alpha = \alpha(q^2 = 0)$ is the fine structure constant and:

$$\Delta\alpha(q^2) = \Delta\alpha_{lep}(q^2) + \Delta\alpha_{top}(q^2) + \Delta\alpha_{had}(q^2). \tag{1.16}$$

is the shift of the coupling constant when the photon momentum is q^2. The quark contributions are included in $\Delta\alpha_{had}$ except the very small top contribution, which is
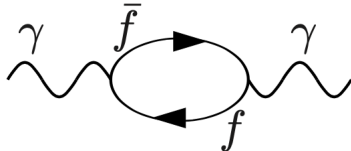
Figure 1.3: One-loop photon self-energy

separated from the other quarks because at *top* energy-scale QCD can be calculated with perturbative methods. This term will be neglected in the following.

Perturbation theory permits to express the contribution from QED to the anomalous magnetic moment (a_μ^{QED}) as a perturbation series in powers of α/π

$$a_{QED} = C_1 \left(\frac{\alpha}{\pi}\right) + C_2 \left(\frac{\alpha}{\pi}\right)^2 + C_3 \left(\frac{\alpha}{\pi}\right)^3 + ... \qquad (1.17)$$

Vacuum polarization enters at the two loop level (fourth order in the electric charge) and it is the only source of difference between the g-factors of the electron and muon, because of their different mass.

1.4 Muon g-2 in the Standard Model

The muon anomaly can be expressed as a sum of three terms inside the SM (representative Feynman diagrams in Fig.(1.4)):

$$a_\mu^{SM} = a_\mu^{QED} + a_\mu^{EW} + a_\mu^{had}. \qquad (1.18)$$

The electromagnetic and weak contributions can be calculated with extreme precision by perturbative calculation. The hadronic one, instead, must rely on experimental data. It is really demanding to measure this contribution and as a matter of fact it presents the biggest uncertainty. The muon anomaly provides a particularly sensitive probe for new physics, more than the electron as the sensitivity goes with m_l^2 ($m_\mu^2/m_e^2 \sim 43000$).

1.4.1 QED contribution

Dealing with the electron, the QED contribution to a_e is largely dominating, as the hadronic and weak ones go with $(m_e/M)^2$ where M is the weak or hadronic scale, far
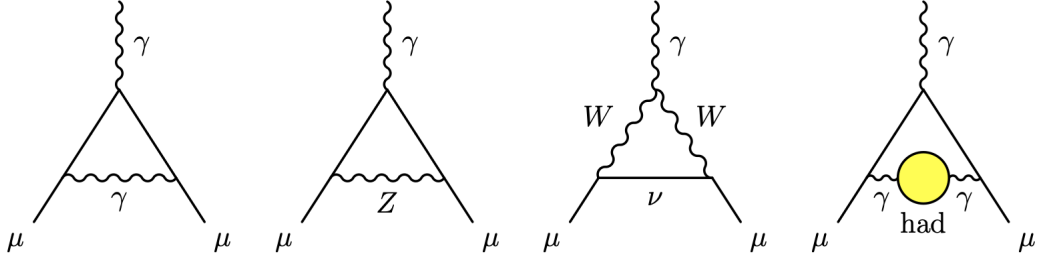
Figure 1.4: Representative diagrams contributing to a_μ . From left to right: leading order QED (Schwinger term), lowest-order weak, lowest-order hadronic.

bigger than the electron mass (order of contribution 10^{-12}). Nowadays, a_e is the most precisely measured quantity [12] and it is a powerful precision test for QED giving the extraordinary agreement with the theoretical evaluation [11]:

$$
\begin{aligned}
a_e^{exp} &= 1\,159\,652\,180.73(28) \times 10^{-12}, \\
a_e^{SM} &= 1\,159\,652\,180.91() \times 10^{-12}.
\end{aligned}
\tag{1.19}
$$

The measured value of a_e is an extremely important result, as it gives the possibility to extrapolate a high level accuracy value for the fine structure constant α, which results in [11]:

$$
\alpha^{-1}(a_e) = 1\,370\,359\,991.50(33) \times 10^{-12}.
\tag{1.20}
$$

Dealing with the muon, the difference in mass with respect to the electron plays a key role in the determination of the anomaly. It is possible to divide a_μ^{QED} in three main contributions:

$$
a_\mu^{QED} = A_1 + A_2(m_\mu/m_e) + A_2(m_\mu/m_\tau) + A_3(m_\mu/m_e, m_\mu/m_\tau)
\tag{1.21}
$$

which take into account the presence of internal loops (Fig.(1.5)) with leptons different from the muons.

In Eq. (1.21), A_1 represents the universal term, which is equal for all the three charged leptons. This term is the dominant one in the electron anomaly reported in Eq.1.19. A_2 enters at two-loop level including loops with lepton flavour different from the external lines, and A_3 includes diagrams with an extra loop, thus having at least three loops. Therefore, there are mass dependent contributions, which are negligible in the electron anomaly.

Each coefficient A_j can be expanded in perturbation theory as a series in α/π:

$$
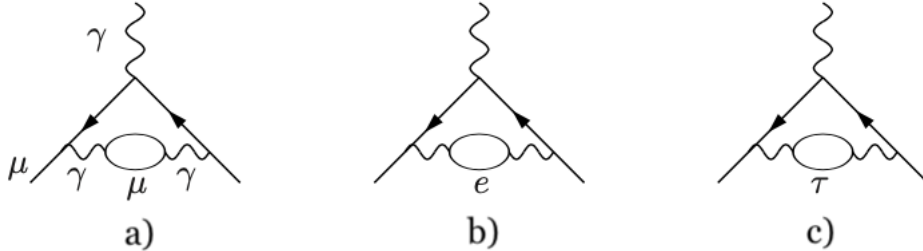A_j = \sum_{i=j}^{N} A_j^{(2i)} \left(\frac{\alpha}{\pi}\right)^i
\tag{1.22}
$$

11

Figure 1.5: Two loop (α^4) diagrams representing leptonic VP contributions. (b) and (c) contribute to the mass dependent corrections to a_μ ($A_2^{(4)}$). (a), having the same lepton flavour in the loop and in the external lines, contributes to the universal term ($A_1^{(4)}$)

where $i \leq j$ according to the given definition.

Currently the QED contribution to a_μ has been calculated to five loops, obtaining [13]:

$$a_\mu^{QED} = 116\,584\,718.931(7)(17)(6)(100)(23) \times 10^{-11} \tag{1.23}$$

where the uncertainties are due to the tau-lepton mass, the α^4 term, the α^5 term, the estimate of the α^6 term, and the value of α taken from the measurement of the Cesium atom $\alpha^{-1} = 137.035999046(27)$ [13], which provides a new determination of the constant independent of the electron magnetic anomaly a_e (Eq. (1.20)), from which α was traditionally extracted.

1.4.2 Electroweak contribution

In Eq.(1.18), a_μ^{EW} collects all the loops involving $W^\pm$, Z or Higgs bosons (Fig.1.6 represents the leading order contributions). Their contribution is not dominant as those terms are suppressed by a factor of $(\alpha/\pi) \cdot (m_\mu^2/m_W^2) \sim 4 \times 10^{-9}$. The current calculations, including two loops and leading three loops, obtain [11]:

$$a_\mu^{EW} = 153.6(1.0) \times 10^{-11}. \tag{1.24}$$

1.4.3 Hadronic contribution: time-like approach

Hadronic loop contributions to a_μ^{SM} give rise to its main theoretical uncertainties, mainly from the leading hadronic vacuum polarization term a_μ^{HLO} and from the hadronic light-by-light contribution a_μ^{HLBL}.
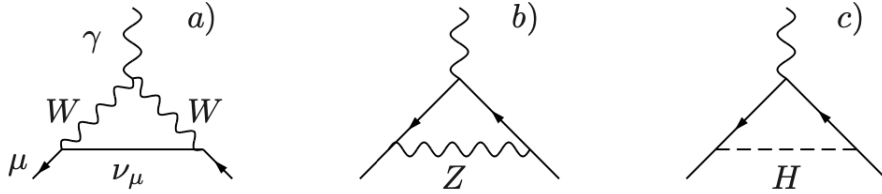
12

Figure 1.6: The leading weak contributions to a_μ.

Hadronic Vacuum Polarization   On a perturbative level, we may obtain the hadronic vacuum polarization term replacing internal lepton loops of the QED VP term by quark loops (Fig.1.7). But due to the non-perturbative nature of QCD at low energies, pQCD
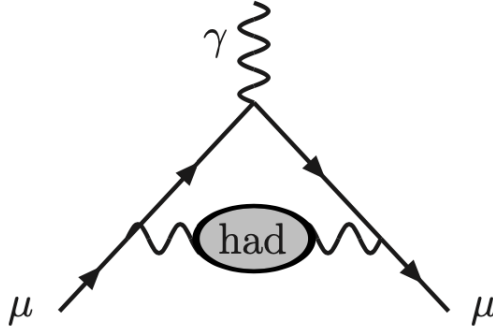

Figure 1.7: The leading hadronic contribution to a_μ.

cannot be applied, therefore a semi-phenomenological approach is needed to compute a_μ^{HVP} via dispersion relations together with the optical theorem and experimental data of the hadron production cross section e^+e^- annihilation.

Because of the analyticity of the vacuum polarization function, this last obeys the dispersion relation

$$\frac{\Pi_\gamma^{had}(q^2)}{q^2} = \int_0^\infty \frac{ds}{s} \frac{1}{\pi} \operatorname{Im} \Pi_\gamma^{had}(s) \frac{1}{q^2 - s}, \tag{1.25}$$

which represents the one from the hadronic contribution. Because of optical theorem, the imaginary part of the vacuum polarization amplitude can be related to the total cross section of a process which in the **time-like** approach is the e^+e^--annihilation

$$\operatorname{Im}\Pi_\gamma^{had}(s) = \frac{s}{4\pi\alpha}\sigma_{had}^0(e^+e^- \to had) = \frac{\alpha}{3}R_{had}(s), \tag{1.26}$$

with

$$R_{had}(s) = \frac{\sigma_{had}^0}{4\pi\alpha^2/3s}. \tag{1.27}$$

13

The dispersion relation in Eq.(1.25) needs the bare cross section for e^+e^- annihilation, that is different from the measured one which is corrected for initial state radiation, effects of the electron vertex loop and VP correction to the photon propagator. The reason is that taking into account the physical σ_{had} would produce double counting of VP effects.

Undressing the cross section requires to replace the running $\alpha(s)$ with the classical α, such that:

$$\sigma_{had}^0 = \sigma_{had} \left(\frac{\alpha}{\alpha(s)} \right)^2 , \tag{1.28}$$

giving as a result in Eq1.27

$$R_{had}(s) = \frac{\sigma_{had}}{4\pi\alpha(s)^2/3s}. \tag{1.29}$$

The lowest order hadronic contribution to the anomaly can be calculated through the dispersion relation

$$a_\mu^{HLO} = \frac{\alpha}{\pi} \int_0^\infty \frac{ds}{s} \frac{1}{\pi} \operatorname{Im} \Pi_{had}(s) K(s) \tag{1.30}$$

which can be written as

$$a_\mu^{HLO} = \left(\frac{\alpha m_\mu}{3\pi} \right)^2 \left(\int_{m_{\pi^0}^2}^{E_{cut}^2} ds \frac{R_{had}^{data}(s)\hat{K}(s)}{s^2} + \int_{E_{cut}^2}^\infty ds \frac{R_{had}^{pQCD}(s)\hat{K}(s)}{s^2} \right) \tag{1.31}$$

with a cut E_{cut} in the energy of a few GeV, separating the non-perturbative low energy part from the perturbative high energy tail. The high energy part is calculable by perturbative QCD and gives negligible contribution to the final uncertainty.

The Eq.1.31 is written in terms of the rescaled kernel function

$$\hat{K}(s) = \frac{3s}{m_\mu^2} K(s). \tag{1.32}$$

The term $1/s^2$ in Eq.1.31 enhances the low energy region; due to resonances (especially the ρ resonance) and threshold effects at low energies, $R_{had}(s)$ in Eq.(1.31) is highly fluctuating (Fig.1.8), therefore this constitutes the main difficulty of the method.

The main channel is $e^+e^- \to \pi^+\pi^-$, with the ρ resonance showing up at ~ 770 MeV. With increasing energy more channels open up and the measurement of $R_{had}(s)$ gets harder.

There are two methods used to measure the cross section:

1. The *direct scan mode*, where the beam energy is adjusted to provide measurements at different center-of-mass (CM) energies (Fig.(1.9.b));

2. The *radiative return method*, where a collider is operating at a fixed CM energy (Fig.(1.9a)). Here the high statistics allow for an effective scan over different masses
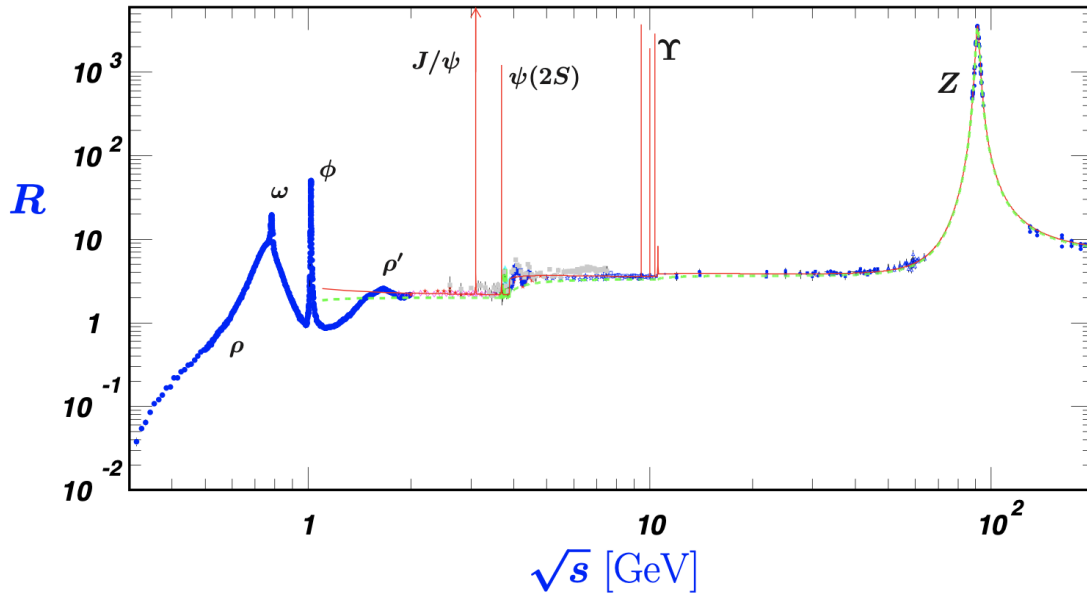
Figure 1.8: Experimental data (in blue) of R(s). The green curve represents a naive quark-parton model prediction, while the red one follows the 3-loop pQCD calculation [11].

of the hadronic system through the emission of initial state photons, whose spectrum can be calculated and, in some cases, measured directly. Hence $\sigma_{had}(s')$ is measured at energies $\sqrt{s'}$ lower than the fixed $\sqrt{s}$ at which the accelerator is running.
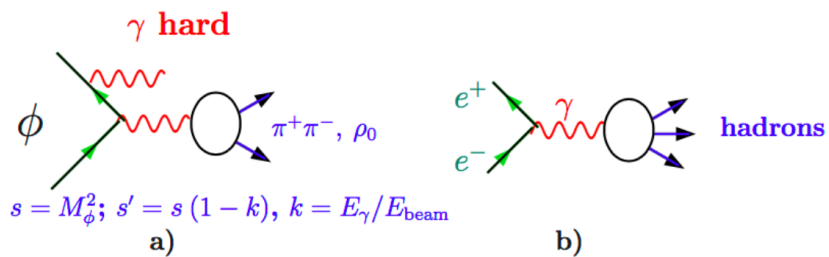

Figure 1.9: a) Principle of the radiative return; b) Direct scan mode [10].

This second method is particularly interesting for meson machines like $\Phi-$ and $B-$ factories with high event rates. Important results have been achieved by KLOE (at the DAΦNE collider in Frascati) and BaBar (at the PEPII collider at SLAC) by measuring the $\pi^+\pi^-$ cross section which is the channel which dominates in σ_{had}.

15

It is important to remark that there are some discrepancies between results from different experiments and this strongly affects the precision of the combined cross sections used for the evaluation of the dispersion integrals [13]. As an example, the most precise $\pi^+\pi^-$ measurements, by KLOE and BaBar, do not agree within the given uncertainties. There is a hope to solve the discrepancy by looking at other experiments, but their results are not precise enough, lying between those of KLOE and BABAR, and overlapping reasonably with both as it can be seen in Fig.(1.10).

For the direct scan mode, precise results below 1.4 GeV from the CMD-2 and SND
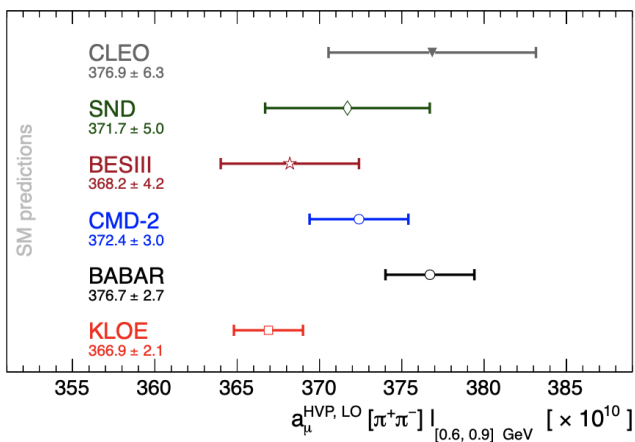

Figure 1.10: Comparison of results from different experiments of $a_\mu^{HLO}(\pi^+\pi^-)$ evaluated between 0.6 GeV and 0.9 GeV [13].

detectors at BINP (Novosibirsk) have been obtained at VEPP-2M, and more recently from CMD-3 and SND at VEPP-2000 up to 2 GeV.

In Fig.(1.11), the recent evaluations of a_μ^{HLO} are shown; the recent review in [13] gives the recommended estimate of:

$$a_\mu^{HLO} = 693.1(40) \times 10^{-10} \tag{1.33}$$

which should provide a realistic evaluation of the current precision of data-driven HVP evaluations. The final error is evaluated as the quadratic sum of experimental uncertainties, systematic errors including the tension between different experimental results and the error related to the pQCD calculation.

Higher-order vacuum polarization contributions are not negligible and need to be considered for the evaluation of a_μ^{HVP}. The main contributions come from diagrams (a) and (b) in Fig.(1.12), while the (c)'s one is very small [13].

The state-of-the-art evaluation of the NLO contribution reported in [13] is
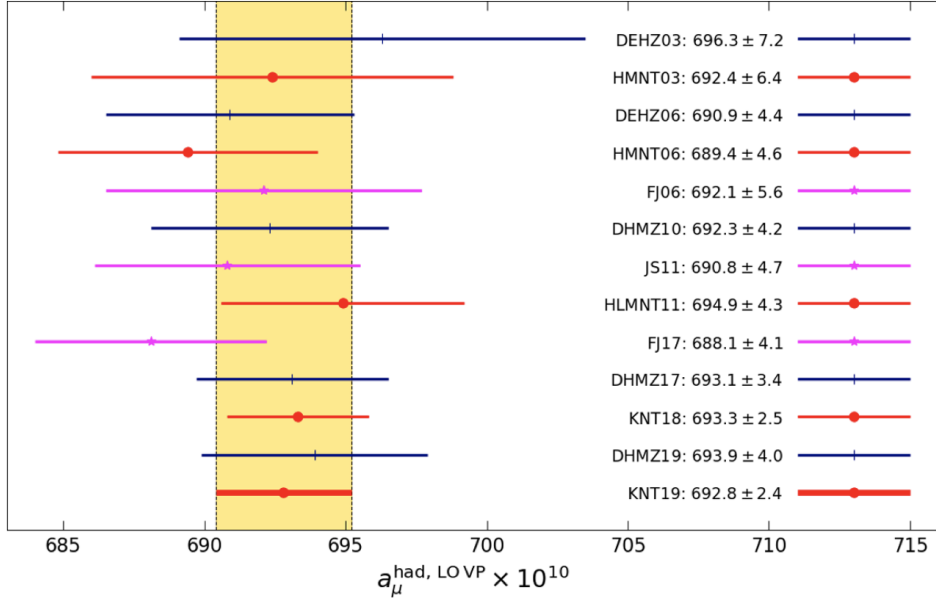
$$a_\mu^{HNLO} = -9.83(7) \times 10^{-10}. \tag{1.34}$$

16

Figure 1.11: Comparison of recent and previous evaluations of a_μ^{HLO} determined from $e^+e^- \to hadrons$ cross section data.
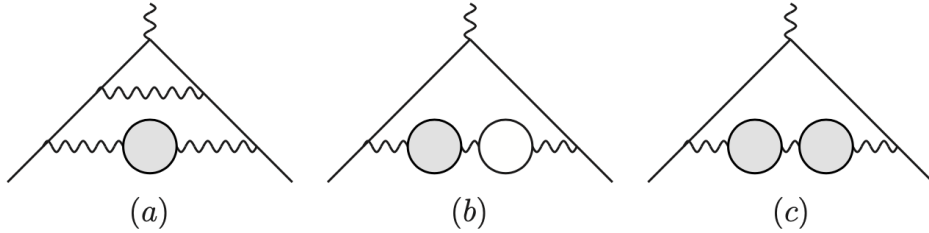

Figure 1.12: Higher-order interactions in vacuum polarization processes. The gray blobs refer to hadronic VP, the white one in diagram (b) to leptonic VP.

Beyond NLO, it is necessary to take into account also NNLO contributions for the aimed accuracy in the value of $g-2$, which have been estimated in [13] to be:

$$a_\mu^{HNNLO} = 1.24(1) \times 10^{-10}. \tag{1.35}$$

These results lead to the sum:

$$a_\mu^{HVP} = a_\mu^{HLO} + a_\mu^{HNLO} + a_\mu^{HNNLO} = 684.5(40) \times 10^{-10}. \tag{1.36}$$

Hadronic Light-by-Light Scattering The last important process which enters in the evaluation of the hadronic contribution to a_μ is the Hadronic Light-by-Light (LbL)

term. It is characterized by a quark loop with four photons attached. This is a problematic term because of its big uncertainties, even if its absolute value is much smaller than the VP contribution. Fig.(1.13) shows a lowest order LbL diagram, where three out of four photons are virtual.

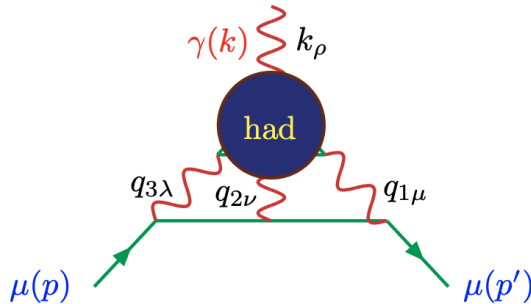Until some years ago this term could not be determined from data, only model depen-

Figure 1.13: Diagram of the hadronic light-by-light interaction process.

dent estimates of the total contribution were made and the large model uncertainties needed to be reduced and better controlled. This is an important issue as those errors are comparable with that of the leading order VP contribution and therefore important, even if the LbL term contributes only marginally to the central value of a_μ^{had}. Recently a new data-driven approach has been developed, based on a dispersive relation, providing a model-independent description of HLbL scattering which allowed to reduce the uncertainty (for more details [16]).

The current estimates reported in [13] are

$$a_\mu^{HLBL} = 92(19) \times 10^{-11} \tag{1.37}$$

and

$$a_\mu^{HLBL,NLO} = 2(1) \times 10^{-11}, \tag{1.38}$$

which have been obtained taking into account the independent data-driven dispersive estimates and the model-dependent ones.

1.4.4 Hadronic contribution: Lattice QCD

There was a remarkable progress in the last years in the evaluation of a_μ^{HVP} with Lattice QCD (LQCD), even if the results are not yet competitive with the dispersive ones obtained with time-like data. As a matter of fact, in LQCD the current uncertainties reach the level of $2 - 3\%$ against $0.5 - 0.6\%$ error of e^+e^- measurements.

In Fig.(1.14) recent results by the various lattice QCD groups (in blue) are reported with those obtained from the data-driven methods (in red). LQCD results seem promising

with the development of theory and calculation in the next future, but nowadays those are still not accurate enough.

The current *lattice world average* reported in [13] is:

$$a_\mu^{HLO}(LQCD) = 711.6(184) \times 10^{-10} \tag{1.39}$$

consistent with the data-driven method giving Eq.1.33 but with a much larger uncertainty.

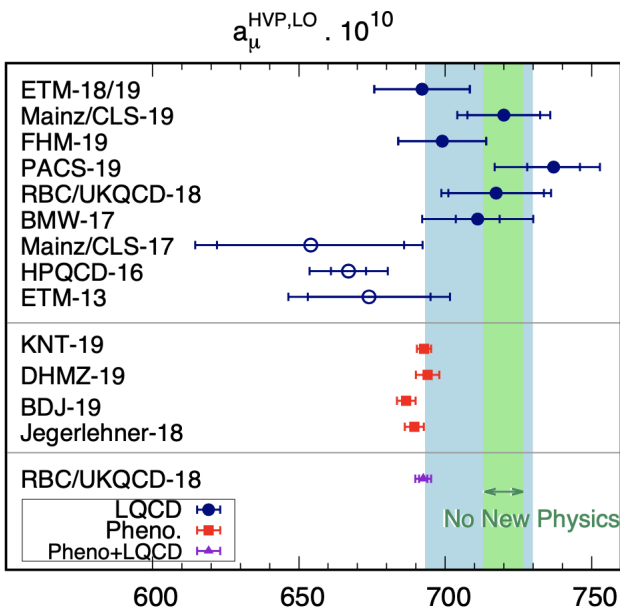Figure 1.14: Recent results for a_μ^{HLO} in units of 10^{-10}. The full blue circles are lattice results included in the *lattice world average*. The average is indicated by a light blue band, while the green band indicates the "no new physics" scenario. The unfilled blue circles are older lattice results or superseded by more recent calculations. The red squares indicate results obtained from the data-driven methods [13].

1.4.5 SM prediction: summing up

Taking into account all these contributions (QED, EW and QCD), the obtained theoretical estimation for the anomalous magnetic moment of the muon within the SM is [13]

$$a_\mu^{SM} = a_\mu^{QED} + a_\mu^{EW} + a_\mu^{HVP,LO} + a_\mu^{HVP,NLO} + a_\mu^{HVP,NNLO} + a_\mu^{HLBL} + a_\mu^{HLBL,NLO} =$$
$$= 116591810(43) \times 10^{-11}$$

(1.40)

where the error is dominated by the hadronic vacuum polarization contributions.

1.5 Experimental measurement of $g - 2$

Numerous experiments in the last six decades have been involved in the measurement of muon's anomaly: from CERN I $(1958 - 1962)$ reaching a 0.4% precision, to BNL $(1990 - 2003)$ which is actually the most precise measurement, achieving 0.5 ppm (Fig.(1.15)). The E821 experiment at Brookhaven obtained the measurement:

$$a_\mu^{exp} = 116592089(63) \times 10^{-11}.$$

(1.41)

The experiment consisted in the injection of muons into a storage ring (Fig.(1.16))in stable orbits with a cyclotron frequency ω_c. Muons, in a strong magnetic field, because of their anomalous magnetic moment, are affected by a spin precession with a frequency ω_s such that:

$$\vec{\omega}_c = -\frac{q\vec{B}}{m\gamma}, \quad \vec{\omega}_s = -\frac{gq\vec{B}}{2m} - (1 - \gamma)\frac{q\vec{B}}{\gamma m}$$

(1.42)

giving as a result of the difference of the two frequencies the *anomalous precession frequency* ω_a

$$\vec{\omega}_a = \vec{\omega}_s - \vec{\omega}_c = -\left(\frac{g-2}{2}\right)\frac{q\vec{B}}{m} = -a_\mu \frac{q\vec{B}}{m},$$

(1.43)

which takes this form also in the presence of an $\vec{E}$ field thanks to a good choice of the momentum: the so-called *magic* momentum of 3.094 GeV/c.

Therefore, a_μ in Eq.1.41 was determined by a precision measurement of ω_a and B [18].

Nowadays, the world is awaiting the result of Fermilab's current Muon $g - 2$ E989 experiment (red dashed line in Fig.(1.15)). It is very promising as its goal is to measure the muon's anomaly to 0.14 ppm, a fourfold improvement over the 0.54 ppm precision of Brookhaven E821. As a matter of fact, the E989 experiment is designed to repeat the BNL measurement with the same technique, reusing the BNL magnet, but with many
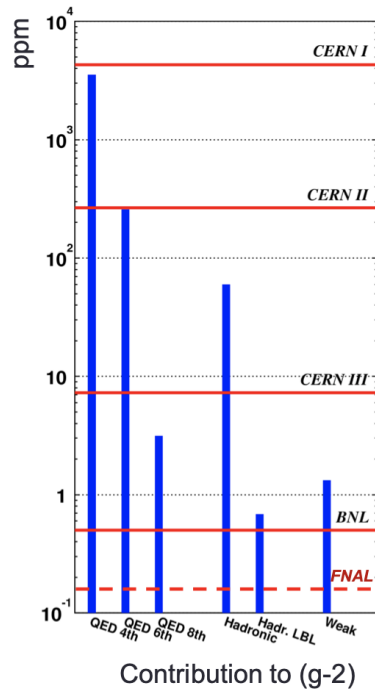
Figure 1.15: Plot showing the precision needed (y axis) to evaluate the different contributions entering in a_μ and what precision all the different experiments involved in past decades were able to achieve.

Figure 1.16: Experimental setup at BNL for E821.

improvements on the experimental setup and with a 20 times higher number of muons, in order to reduce the statistical uncertainty [19].

An alternative and innovative approach is proposed at J-PARC in Japan for the Muon $g - 2$/EDM experiment. It will feature an ultra-cold muon beam, with a factor of

10 lower muon momentum, injected into a compact storage ring, 20 times smaller in diameter and with a highly uniform magnetic field compared with previous and ongoing mu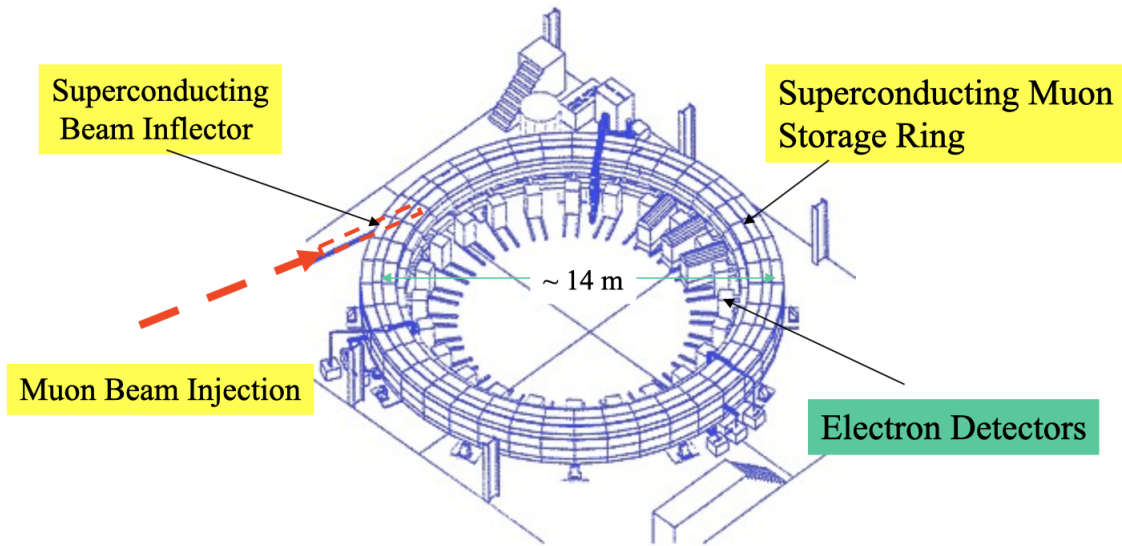on $g - 2$ experiments (Fig.1.17). The innovation is the unprecedented quality of the storage magnetic field $\vec{B}$ which is fundamental for the calculation of a_μ as seen in Eq.1.43. The initial goal is to reach the statistical uncertainty of BNL E821, with much smaller systematic uncertainties from sources different from the current method [20].
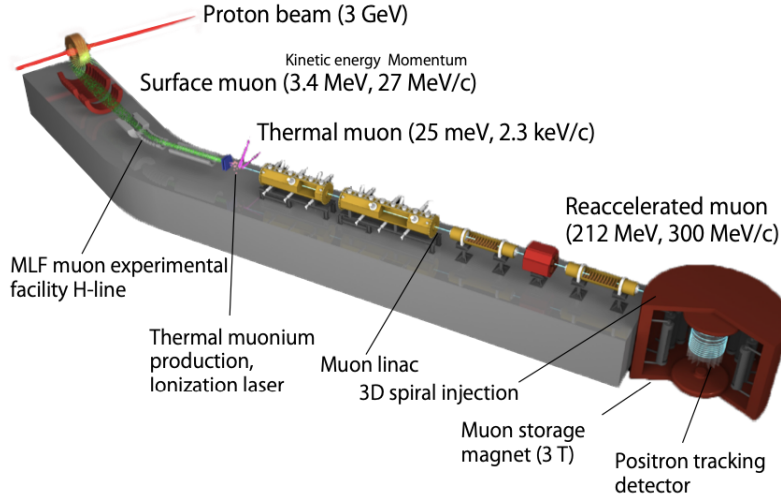
Figure 1.17: Experimental setup at J-PARC for Muon $g - 2$/EDM experiment.

1.6 Theory versus Experiment: Hint of New Physics?

The history of this observable is not over, looking at the values in Eq.(1.40) and Eq.(1.41) there is a discrepancy between the two:

$$\Delta a_\mu = a_\mu^{exp} - a_\mu^{th} = 279(76) \times 10^{-11} \tag{1.44}$$

which corresponds to a deviation of 3.7σ.
The reason of that difference would lie in one of these three possible causes:

1. Theoretical evaluations could be wrong or underestimate the uncertainty. The hadronic light-by-light term could be responsible for the disagreement, but its latest improved calculations have smaller uncertainties that could not explain it. Otherwise, there could be an issue in the evaluation of the Hadronic VP term, given by the data-driven method.

2. The experimental measurements could have underestimated systematic uncertainties.

3. This discrepancy is true and it is produced by new physics beyond the Standard Model (BSM).

In order to understand if new physics comes into play, it is important to improve the precision on the experimental measurement, as J-PARC and E989 at Fermilab aim to do, or find innovative ways for the measurement of the Hadronic VP term. In [21] it is highlighted that the scenario where Δa_μ arises from hypothetical errors in the evaluation of the hadronic cross section $\sigma_{had}(s)$ (Eq.1.29), rather than new physics, leads to several consequences.

The same cross section data are used as input into dispersion relations to calculate the hadronic contribution to the running QED coupling evaluated at the Z-pole, $\Delta\alpha_{had}^{(5)}(M_Z^2)$, which is an important component of the global fits to the EW sector of the SM. The commonly used result for HVP from dispersive approach leads to a consistent global EW fit, but generates the Δa_μ discrepancy.

Starting from the hypothesis that Δa_μ is given by missing contributions in $\sigma_{had}(s)$, the corresponding shifted values in $\Delta\alpha_{had}^{(5)}(M_Z^2)$ would modify EW fit predictions of W boson mass M_W, $sin^2\theta_{eff}^{lep}$ and Higgs boson mass M_H. Being consistent with the measured values of the EW observables, the only region of energy where the missing contributions could be is at ~ 0.7 GeV; but, in order to solve the $g-2$ discrepancy, the hadronic cross section would need to be improbably larger than its current robust measurement. Nevertheless, the experimental measurement of the anomaly has been confirmed in the last years by some LQCD calculations (e.g. [22]), therefore alternative confirmations of the dispersive estimated of a_μ^{HVP} are needed to solve this dichotomy between dispersive approach and recent LQCD evaluations. If the adjustment of the HVP term would turn out to reconcile experiment and SM prediction, it would thus not necessarily weaken the case for physics beyond the SM, but to some extent shift it from $g-2$ to the EW fit [23]. On the other way, if that Δa_μ discrepancy is real, it points out to new physics as low-energy Supersymmetry (SUSY) where the missing contribution to the anomaly is given by the existence of supersymmetric partners. Furthermore, in the SUSY framework, the discrepancy is sensitive to many parameters difficult to measure at LHC, thus it would give more stringent bounds and constrains on those. Therefore, muon $g-2$ is a powerful discriminator amongst model of physics and, because of that, its measure would be extremely important for the physics of next generation.

Chapter 2

The MUonE experiment

The largest contribution to the theoretical uncertainty of a_μ is the one of the hadronic vacuum polarization term a_μ^{HVP}. Through the dispersive approach, which exploits e^+-e^- annihilation data and pQCD, it is possible to evaluate this contribution; nevertheless, in the low energy region where the data-driven method is applied, it is difficult to evaluate the integral with high precision because of resonances and threshold effects. This is the main difficulty of the method, thus, being LQCD not competitive yet, it is fundamental to find a new approach to increase the precision and keep on understanding what is behind the discrepancy between the theoretical evaluations and the experimental measurement. This is what the MUonE collaboration aims to do; their innovative proposal is to evaluate the HVP term through the high precision measurement of the effective electromagnetic coupling α^{QED} in the space-like region where the vacuum polarization is a smooth function [25].

2.1 Hadronic contribution: space-like approach

In the time-like approach, a_μ^{HLO} is defined by Eq.1.30, where $\mathrm{Im}\Pi_{had}$ is proportional to $\sigma_{had}(e^+e^-)$. Through some mathematical steps [24], the time-like equation can be redefined as a space-like integral

$$a_\mu^{HLO} = \frac{\alpha}{\pi} \int_0^1 dx (x-1) \bar{\Pi}_{had}[t(x)] \tag{2.1}$$

where

$$\bar{\Pi}_{had}(t) = \Pi_{had}(t) - \Pi_{had}(0) \tag{2.2}$$

and

$$t(x) = -\frac{x^2 m_\mu^2}{1-x} < 0 \tag{2.3}$$

is a space-like squared $4-$momentum.

The running of the coupling constant in Eq.1.15 is expressed as a function of $\Delta\alpha(q^2)$ which can be defined as

$$\Delta\alpha(q^2) = -\text{Re}(\bar{\Pi}(q^2)) = -\text{Re}(\bar{\Pi}_{lep}(q^2)) - \text{Re}(\bar{\Pi}_{had}(q^2)). \tag{2.4}$$

In the space-like region of momenta, the value of q^2 is negative $(q^2 < 0)$, giving as a result the imaginary part of $\bar{\Pi}_{had}(q^2)$ equal to zero. Therefore

$$\bar{\Pi}_{had}(q^2) = \text{Re}(\bar{\Pi}_{had}(q^2)) = -\Delta\alpha_{had}(q^2) \tag{2.5}$$

and Eq.2.1 becomes

$$a_\mu^{HLO} = \frac{\alpha}{\pi} \int_0^1 dx(1-x)\Delta\alpha_{had}[t(x)]. \tag{2.6}$$

The hadronic shift $\Delta\alpha_{had}[t(x)]$ cannot be calculated in perturbation theory as it involves QCD contributions at low-energy scales. However, its expression considering LO processes can be determined starting from the effective coupling

$$\alpha(t) = \frac{\alpha}{1 - \Delta\alpha(t)} = \frac{\alpha}{1 - \Delta\alpha_{lep}(t) - \Delta\alpha_{had}(t)} \tag{2.7}$$

with $\alpha(t=0) = \alpha$, giving as a result

$$\Delta\alpha_{had}(t) = 1 - \Delta\alpha_{lep}(t) - \frac{\alpha}{\alpha(t)}. \tag{2.8}$$

The leptonic contribution can be calculated in perturbation theory, thus it is possible to subtract it in order to get the hadronic. This is not true anymore at higher order calculations, resulting in a more complex expression which needs the implementation of Monte Carlo simulations.

The change from annihilation (s-channel) to scattering (t-channel) process simplifies the evaluation of the anomaly. While the calculation's precision of the time-like integral in Eq.1.31 was compromised by the fluctuations of $R_{had}(s)$, now the hadronic contribution to the effective coupling is a quite smooth function of the variable x free of any resonance poles, as shown in the left plot of Fig.(2.1), and this simplify the evaluation of the integral. The range $x \in [0,1]$ corresponds to $t \in [-\infty, 0]$ where $x = 0$ when $t = 0$. The expected integrand in Eq.(2.6) is shown as a function of the variable x in the right plot of Fig.(2.1), the value of $\Delta\alpha_{had}$ at the peak $x_{peak} \approx 0.914$ is: $\Delta\alpha_{had}(t_{peak}) \approx 7.86 \times 10^{-4}$ where $t_{peak} \approx -0.108$ GeV^2.

This new method which involves the dispersive integral in the space-like region is at the base of the MUonE project and the main idea would be described in details in the next section.
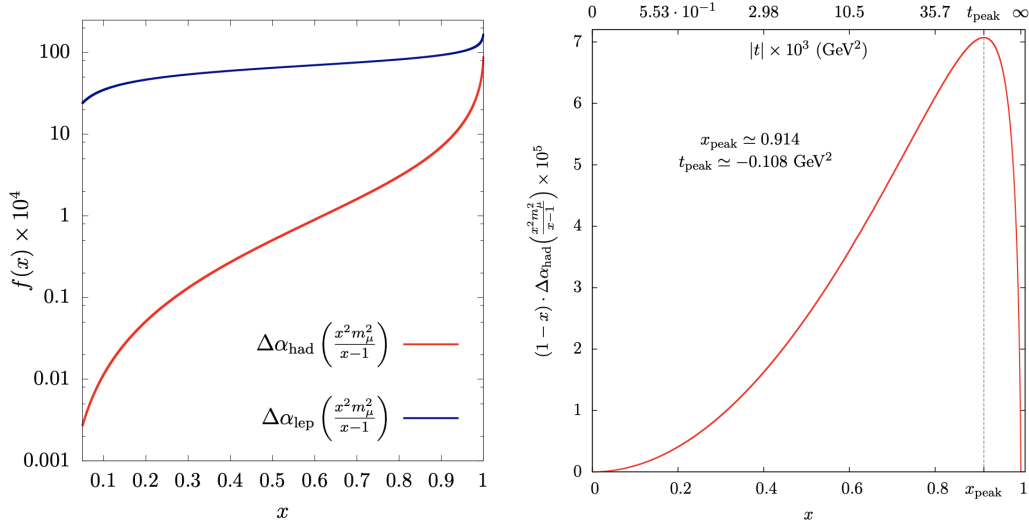
Figure 2.1: Leptonic and hadronic contribution to the running of α^{QED} on the left as a function of x and the integrand $(1-x)\Delta\alpha_{had}[t(x)]$ as a function of x and t on the right.

2.2 Experimental Proposal

The MUonE experiment aims at an independent and very precise measurement of the leading hadronic contribution to the muon magnetic moment a_μ^{HLO}, through a novel method involving the dispersive integral in the space-like region of Eq.2.6, as proposed in [27]. This approach requires the measurement of the hadronic contribution to the running of α in the space-like region $\Delta\alpha_{had}(t)$. In the past, few direct measurements of that term were computed and the most precise was obtained by OPAL [26] from small-angle Bhabha scattering. There are some intrinsic limitations related to this process, an example is the mixing of s and t channels which complicates the extraction of $\Delta\alpha_{had}(t)$ from data limitating the accuracy on a_μ^{HLO}. The MUonE proposal is to exploit the t-channel μe elastic scattering cross section at low energy, overcoming some difficulties concerning Bhabha scattering physics.

MUonE has to measure, with an unprecedented precision, the shape of the differential cross section of $\mu - e$ elastic scattering, using the intense muon beam available at CERN, with energy of 150 GeV, on atomic electrons of a light target. The reasons why it is an extremely appealing proposal are listed in the following points:

1. Differently from Bhabha scattering, it is a pure t-channel process, where the dependence on t of the differential cross section is proportional to $|\alpha(t)/\alpha|^2$ [27]:

$$\frac{d\sigma}{dt} = \frac{d\sigma^0}{dt}\left|\frac{\alpha(t)}{\alpha}\right|^2,\tag{2.9}$$

enabling an easier extraction of the running of $\alpha(t)$.

26

2. The highly energetic muons from CERN M2 beam allow to access the region of the peak of the integrand function (Eq.2.6) shown in Fig.(2.1).

3. The boosted kinematics of the collision guarantees the containment of all the events in a single homogeneous detector, as the angular deflection stays in a 50 mrad cone.

4. The kinematics of the elastic scattering is well known and determined by angular observables. This permits to identify the signal region through the correlation of muon and electron scattering angles, shown in Fig.(2.2). It is evident from that picture that for $\theta_e < 5$ mrad there is an ambiguity region where $\theta_e \sim \theta_\mu$ and which needs to be treated carefully in order to have the right μ/e identification.
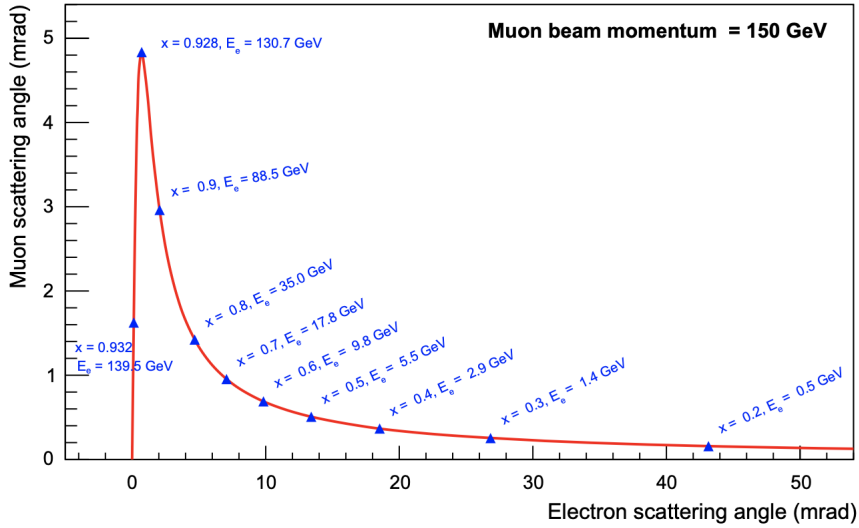

Figure 2.2: Correlation plot of the scattering angles of muons and electrons from elastic scattering events given a 150 GeV muon beam.

2.2.1 Precision requested for the measurement

The challenge of the experiment is to achieve a statistical and systematic uncertainty in the measurement of the μe differential cross section at the level of 10ppm, this permits to have the new space-like determination of a_μ^{HLO} competitive with the present time-like approach. A competitive determination requires a precision of the order of 10^{-2} in the measurement of the hadronic running, which translates into a precision of 10^{-5} in the shape of the differential cross section.

The aimed accuracy requires an excellent control of many effects:

27

1. on the theoretical side, the effect of radiative corrections to the μe cross section, which requires NLO [28] and NNLO calculations [13]. In order to extract with high precision $\Delta\alpha_{had}(t)$, a Monte Carlo code accurate to the NNLO level of radiative contributions must be available;

2. on the experimental side, there are different effects which need to be taken into account:

   (a) the detector resolution for the signal/background selection;

   (b) the control of multiple Coulomb scattering effect which breaks the muon-electron angular correlation of Fig(2.2) and the planarity;

   (c) uniformity of sensors' efficiency;

   (d) tracker alignment and the knowledge of the longitudinal dimension of the tracking stations;

   (e) the knowledge of the mean energy of the beam which needs to be calibrated with a physical process.

   More details on those would be given in the section dedicated to the experimental apparatus.

2.2.2 Extraction of the hadronic contribution

The experimental workflow is articulated in precise steps:

1. preparing the detector in order to have good quality data (good efficiency of detection, reconstruction, readout, calibration etc.);

2. a selection of signal events which helps in the rejection of background ones (mainly nuclear processes due to $\mu - N$ scattering which induce the production of $e^+ - e^-$ couples), suppression of radiative events and reduction of some detector effects;

3. precise measurement of the scattering angles of the outgoing muons and electrons (θ_e, θ_μ);

4. shape of the differential cross section for the elastic scattering events;

5. a template fit for the extrapolation of the hadronic contribution $\Delta\alpha_{had}(t)$ on the observable;

6. evaluation of the hadronic VP contribution a_μ^{HLO} through the master integral in Eq.2.6.

The average beam intensity for energies at 150 GeV is of $\sim 1.3 \times 10^7$ muons/s. Assuming 2 years of data taking and a running time of $\Delta t_0 \sim 2 \times 10^7$ s/year with a target thickness of $d = 60$ cm, the integrated luminosity is of 1.5×10^7 nb^{-1}. This permits the collection of the statistics required to achieve the aimed accuracy for MUonE, which amounts to

$$N_{tot} = L \cdot \sigma_{\mu e} \sim 3.7 \times 10^{12}. \tag{2.10}$$

where $\sigma_{\mu e}$ is the process cross section.

A modular detector is proposed, composed by a sequence of N detection stations ($N = 40$), each one made of one target layer (~ 1.5 cm of Beryllium or Graphite) and silicon microstrip tracking detectors, for an overall length of 1 m (Fig.2.3). At the end of the
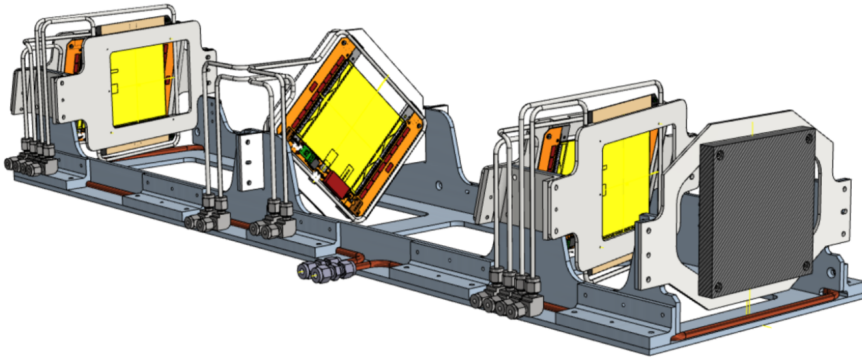

Figure 2.3: Drawing of a MUonE tracking station.

tracking region, an electromagnetic calorimeter (ECAL) is set to measure the electron energy followed by a muon detector. Those two will help the tracker to identify the electron and muon tracks and to suppress physical and beam backgrounds. This identification is needed for building up the shape of the differential cross section which will define the counting ratio $R(\theta_i)$:

$$R(\theta_i) = \frac{d\sigma_{data}(\Delta\alpha_{had}(t) \neq 0)/d\theta_i}{d\sigma_{MC}(\Delta\alpha_{had}(t) = 0)/d\theta_i} = \frac{dN_{data}(\Delta\alpha_{had}(t) \neq 0)/d\theta_i}{dN_{MC}(\Delta\alpha_{had}(t) = 0)/d\theta_i}. \tag{2.11}$$

In Eq.2.12, the observables θ_i are the scattering angles of the outgoing muon and electron ($i = e, \mu$) from the elastic scattering process, $d\sigma_{data}(\Delta\alpha_{had}(t) \neq 0)/d\theta_i$ and $dN_{data}(\Delta\alpha_{had}(t) \neq 0)/d\theta_i$ are respectively the differential cross section and the observed event yield of the elastic scattering, while $d\sigma_{MC}(\Delta\alpha_{had}(t) = 0)/d\theta_i$ and $dN_{MC}(\Delta\alpha_{had}(t) = 0)/d\theta_i$ are the corresponding MC predictions obtained with $\alpha(t) = \Delta\alpha_{lep}(t)$ where the hadronic running $\Delta\alpha_{had}(t)$ is switched off. The differential cross sections respect the two angles are shown in Fig.(2.4) from [25] with the expected events for the MUonE
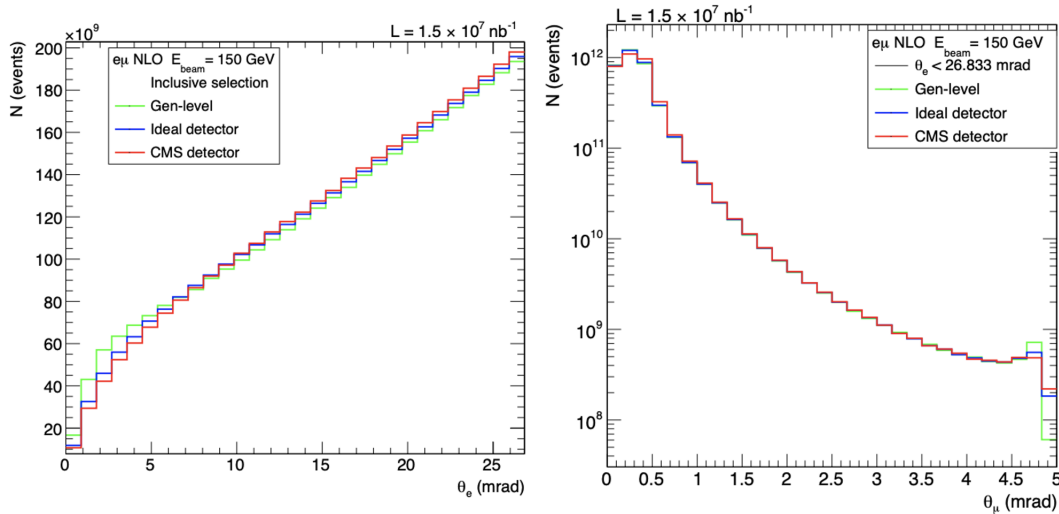
Figure 2.4: Electron (left) and muon (right) angular distributions. Entries correspond to the expected events for the nominal MUonE integrated luminosity [25].

integrated luminosity of 1.5×10^7 nb^{-1}.

From Eq.2.9, $R(\theta_i)$ at LO results in

$$R(\theta_i) = \left| \frac{\alpha(t)}{\alpha} \right|^2 = \frac{1}{|1 - \Delta\alpha_{lep}(t) - \Delta\alpha_{had}(t)|^2}, \tag{2.12}$$

which can be used for the extraction only if just leading order events are considered. The MUonE proposal imposes a knowledge of the differential cross section at the NNLO level, hence, taking into account higher order contributions, this expression cannot be used for the final extrapolation of the hadronic contribution. It would be carried out by a template fit method on the ratio $R(\theta_i)$ in Eq.2.11 which is deeply described in the Letter of Intent [25] and requires an implementation of the theoretical NLO and NNLO prediction into a Monte Carlo event generator code.

2.3 $\mu - e$ elastic scattering theory

2.3.1   Kinematics

Elastic $\mu - e$ scattering process in Fig.(2.5) is represented by

$$\mu^{\pm}(p_1)e^-(p_2) \rightarrow \mu^{\pm}(p_3)e^-(p_4) \tag{2.13}$$

where p_1, p_2 and p_3, p_4 are the 4-momenta respectively of the initial and final state particles. In a fixed target experiment, the electron is initially at rest, thus in the
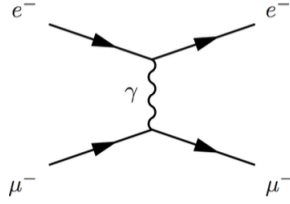
Figure 2.5: Feynman diagram for $\mu - e$ elastic scattering process.

laboratory system (LAB) Mandelstam variables s and t are defined as

$$
\begin{aligned}
s &= (p_1 + p_2)^2 = (p_3 + p_4)^2 = m_\mu^2 + m_e^2 + 2m_e E_\mu, \\
t &= (p_2 - p_4)^2 = (p_1 - p_3)^3 = 2m_e^2 - 2m_e E_e', \\
s + t + u &= 2m_\mu^2 + 2m_e^2.
\end{aligned}
\tag{2.14}
$$

For any given value of the incoming muon momentum, there exists a maximum four-momentum transfer $q_{max}^2 = -t_{min}$:

$$
t_{min} = -\frac{\lambda(s, m_\mu^2, m_e^2)}{s}
\tag{2.15}
$$

where $\lambda(a, b, c)$ is the Källen function defined as

$$
\lambda(a, b, c) = a^2 + b^2 + c^2 - 2ab - 2ac - 2bc.
\tag{2.16}
$$

Given the M2 CERN muon beam, at a reference value $E_\mu = 150$ GeV it is found

$$
t_{min} = -(380 \text{ MeV})^2.
\tag{2.17}
$$

The parameters for the Lorentz transformation between LAB and center-of-mass system (CMS) are

$$
\begin{aligned}
\gamma &= \frac{E_\mu + m_e}{\sqrt{s}} = \frac{s + m_e^2 - m_\mu^2}{2m_e \sqrt{(s)}}, \\
\beta &= \frac{p_\mu}{E_\mu + m_e} = \frac{\lambda^{1/2}(s, m_\mu^2, m_e^2)}{s + m_e^2 - m_\mu^2};
\end{aligned}
\tag{2.18}
$$

The CMS energy corresponding to the muon beam energy is $\sqrt{s} \sim 0.405541$ GeV and the Lorentz γ factor $\gamma \sim 370$.

Thus the elasticity condition which relates the scattering angles θ_e and θ_μ (LAB frame) results

$$
tan\theta_\mu = \frac{2tan\theta_e}{(1 + \gamma^2 tan^2\theta_e)(1 + g_\mu^*) - 2},
\tag{2.19}
$$

31

where

$$g_\mu^* = \frac{\beta}{\beta_\mu^*} = \frac{E_\mu m_e + m_\mu^2}{E_\mu m_e + m_e^2} \tag{2.20}$$

and β_μ^* is the muon velocity in the CMS. The elasticity curve in Fig.(2.2) is Eq.2.19 in the $\theta_e - \theta_\mu$ plane and it is the fundamental constrain for MUonE to allow the discrimination of elastic scattering events and background processes.

The energy and scattering angle of the electron in the LAB are defined as:

$$E_e' = m_e \frac{1 + \beta^2 \cos^2 \theta_e}{1 - \beta^2 \cos^2 \theta_e}, \quad \cos \theta_e = \frac{1}{\beta} \sqrt{\frac{E_e' - m_e}{E_e' + m_e}}. \tag{2.21}$$

The elastic scattering kinematics, if the incident particle has a mass bigger than the particle at rest, as it happens for muon and electron, gives a maximum scattering angle for the outgoing muon:

$$\sin \theta_\mu^{max} = \frac{m_\mu}{m_e} \rightarrow \theta_\mu^{max} = 4.8 \text{ mrad}, \tag{2.22}$$

while the recoiling electron can be emitted at larger angles according to its energy, i.e. $0 \leq \theta_e \leq \sim 32 \text{ mrad}$ for the electron energy $E_e' \gtrsim 1\text{GeV}$ (arbitrary cut at 1 GeV). Therefore, when both scattering angles are lower than 4.8 mrad there is an ambiguity between muon and electron which must be resolved with μ/e discrimination.

While for elastic processes the t is equal for electron and muon, going at higher orders allowing for additional emission of photons in the final state, the momentum transferred needs to be distinguished for electron and muon:

$$\begin{aligned} t_e &= (p_2 - p_4)^2 = 2m_e^2 - 2m_e E_e', \\ t_\mu &= (p_1 - p_3)^2. \end{aligned} \tag{2.23}$$

2.3.2 Differential cross section

Starting at LO in QED there is a single diagram with t-channel exchange of a photon (Fig.(2.6.a)). In order to obtain the LO differential cross section, the first step is the integration of the squared matrix element $M_n^{(0)}$ over the two-particle (e and μ) phase space:

$$d\sigma^0 = \int d\Phi_n M_n^{(0)} = \int d\Phi_n |A_n^{(0)}|^2, \tag{2.24}$$

where $A_n^{(0)}$ is the LO amplitude of the $\mu e \rightarrow \mu e$ process and $n = 2$. It brings to the definition of the differential cross section

$$\frac{d\sigma^0}{dt} = \frac{1}{\lambda(s, m_\mu^2, m_e^2)} \left[(s - m_\mu^2 - m_e^2)^2 + st + \frac{1}{2}t^2 \right]. \tag{2.25}$$

(a) LO QED diagram

(b) HVP contribution at NLO
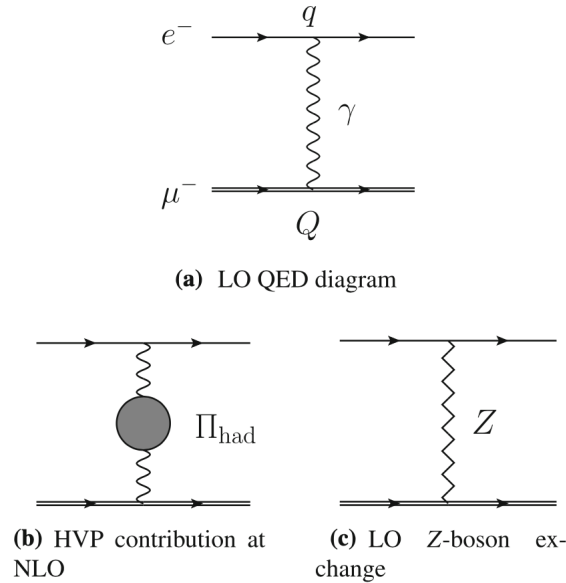
(c) LO Z-boson exchange

Figure 2.6: LO contributions from QED, hadronic VP and Z-boson exchange [31].

This calculation is valid both for positive and negative muons, which will be available as beam particles at the CERN North Area where the M2 beam is situated.

The definition of the LO differential cross section is not enough for the aimed 10 ppm
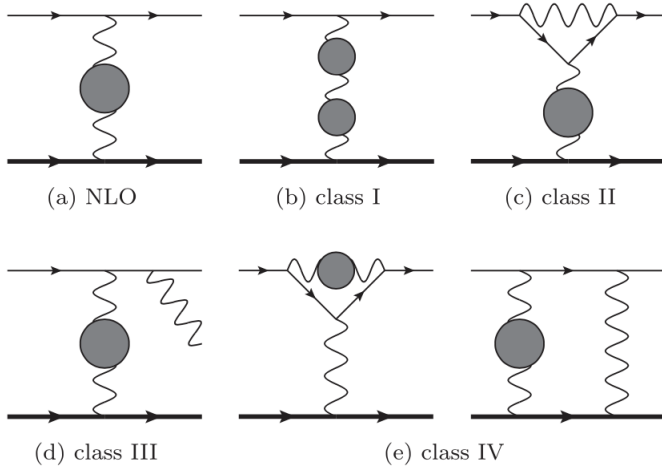

(a) NLO

(b) class I

(c) class II

(d) class III

(e) class IV

Figure 2.7: (a) Diagram which contributes to the hadronic correction to μe scattering at NLO. (b)-(e) Some diagrams contributing to the four classes of hadronic corrections at NNLO. The gray blobs indicate hadronic vacuum polarization insertions [29].

accuracy, NLO and NNLO corrections need to be considered, thus Eq.2.25 have to be modified.

Electroweak contributions due to the exchange of Z bosons (Fig.(2.6.c)) are strongly suppressed because of the large mass M_Z, however the interference between $\gamma - Z$ can not be neglected and those LO weak corrections need to be taken into account in the

calculation. The vacuum polarization contributions considered are from leptons and hadrons, represented by the insertion of the leptonic and hadronic bubble in the photon propagator Fig.(2.6.b). Their diagrams, with the ones with real photon emissions, and their interference need to be taken into account both at NLO and NNLO level (Fig.(2.7)). A detailed study with a MC code has been developed by theoretician [28] and then used by the MUonE collaboration for the inclusion of higher-order contributions to the μe elastic scattering process by computing the full set of NLO corrections to the process in the SM, both from QED and purely weak effects. On the NNLO side, recent studies have been made on the full set of contributions and more details can be found in [13].

NLO QED corrections

There are two kinds of NLO QED events: i) when the photon is virtual, $2 \to 2$ processes which include one-loop virtual corrections; ii) when the photon is real, $2 \to 3$ bremsstrahlung processes $\mu e \to \mu e + \gamma$. The NLO cross section is split into two contributions:

$$
\begin{aligned}
d\sigma^{(1)} = d\sigma_{\mu e \to \mu e} + d\sigma_{\mu e \to \mu e \gamma} = \\
= d\sigma_{NLO}^{virtual} + d\sigma_{NLO}^{real} = \\
= \int d\Phi_n M_n^{(1)} + \int d\Phi_{n+1} M_{n+1}^{(0)}
\end{aligned}
\tag{2.26}
$$

where $n = 2$.

The study carried out in [28], which includes all the electroweak (QED+pure weak)

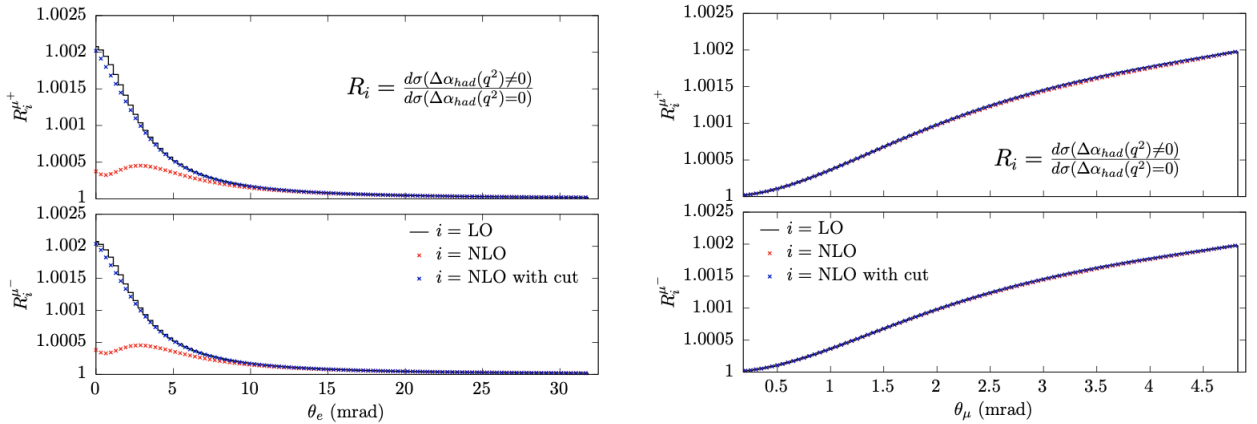Figure 2.8: Upper panels have plots for $\mu^+ e^- \to \mu^+ e^-$ process while lower for $\mu^- e^- \to \mu^- e^-$. On the left, the ratios R_i are shown as a function of the electron scattering angle, on the right as a function of the muon one.

effects, showed some results for the quantities:

$$R_i = \frac{d\sigma_i(\Delta\alpha_{had.}(t) \neq 0)}{d\sigma_i(\Delta\alpha_{had.}(t) = 0)} \qquad (2.27)$$

which represent the ratio of a generic cross section σ_i including the contribution of $\Delta\alpha_{had}(t)$ to the running of α and the same cross section without it, giving the sensitivity of a given observable (e.g. scattering angles) to the signal of interest. In Fig.(2.8) the chosen observables are θ_e, θ_μ and both the processes $\mu^\pm e^- \to \mu^\pm e^-$ are considered. LO and NLO results are shown, where the energy of the outgoing electron is requested to be greater than 1 GeV. The signal visible at LO on the electron angle is almost completely washed out by photon radiation effects at NLO. Therefore, in addition events with a selection cut on the acoplanarity $\pi - (\phi_e - \phi_\mu)$ between the scattered electron and muon are shown. This cut enhances the sensitivity to the hadronic correction helping in the selection of elastic scattering events.

From the distributions as a function of the electron angle, it is clear how the sensitivity is largely recovered by the application of cuts, removing the contribution of radiative processes; while the distribution as a function of the muon angle is particularly robust under those and also under cuts, being less affected by real photon emission.

Cuts would be useful to recover the elasticity condition. The correlation plot $\theta_e - \theta_\mu$,
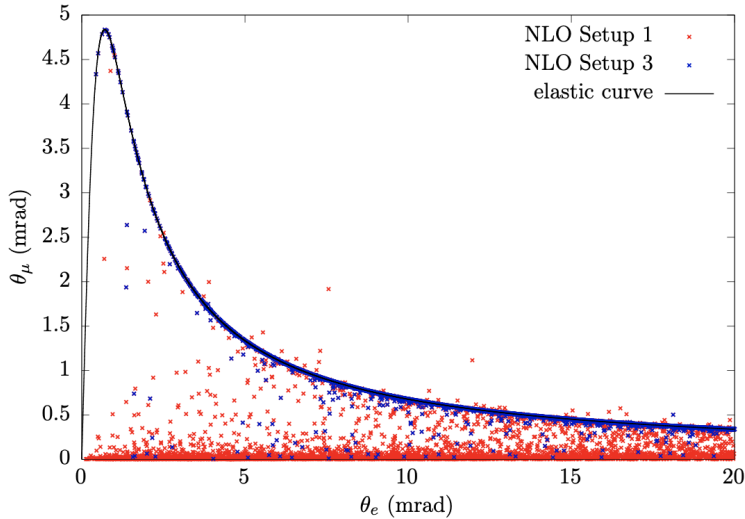

Figure 2.9: Scattering angle of the electrons VS scattering angle of the muons. The line in blue represents the elastic correlation, while the dots are NLO events with (in red) and without (in blue) a cut on the acolpanarity.

which helps in the selection of signal events, is strongly affected by radiative processes in particular at low muon angles; in Fig.(2.9), NLO Setup 1 corresponds to NLO events

35

with $E_e > 0.2$ GeV while NLO Setup 3 have an additional condition on the acoplanarity which helps in recovering the correlation.

2.4 Experimental apparatus

Muons with momentum ~ 150 GeV$/c$, from the CERN M2 muon beamline, impinge on atomic electrons of Beryllium or Graphite targets. In order to measure the scattering angles, a dedicated tracking system is needed to reconstruct the two particles' paths. The apparatus is mainly divided in three parts as represented in Fig.(2.10):

1. tracking system;

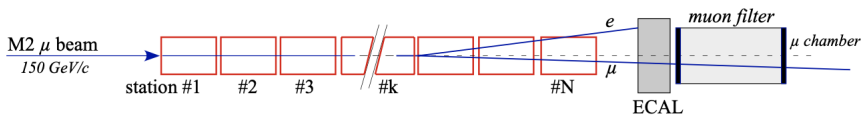2. electromagnetic calorimeter;

3. muon filter.

Figure 2.10: Set up of the MUonE experimental apparatus.

2.4.1 Tracking system

Several requirements are needed to performe the tracking:

1. maximize the coverage of the region of interest of the process having a uniform detector;

2. minimize the Multiple Coulomb Scattering (MCS) in order to reduce the smearing of the true particle trajectories, outgoing from the scattering process;

3. increase the collection of data;

4. a good angular resolution.

The q^2 range of interest corresponds to $E_e \gtrsim 1$ GeV that, having a muon beam of momentum 150 GeV$/c$, consists in a maximum scattering angle of 30 mrad. Hence, an active area of 10×10 cm^2 with 1 m stations is sufficient to contain all the kinematics and it can be achieved with a single silicon sensor, guaranteeing the uniformity of the

detection efficiency needed for detectors in high beam rate environment.

In order to minimize the MCS, the total thickness of the target (60 cm) is subdivided into 40 slices. Therefore the tracking apparatus is divided into 40 stations (one station in Fig.(2.11)), each of length 1 m with a target layer 1.5 cm thickness.

Dividing the apparatus in such modules, the same muon beam is 're-used': it interacts
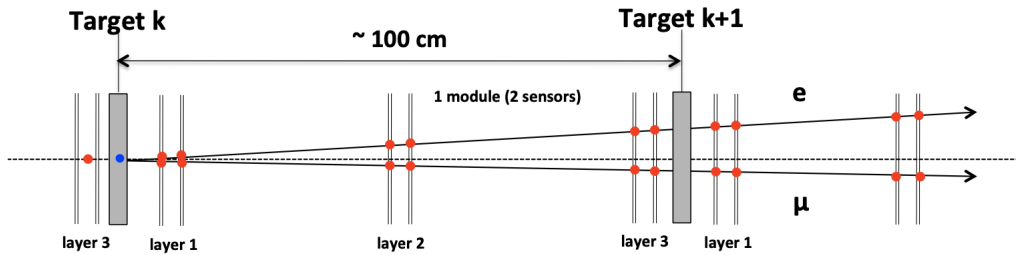

Figure 2.11: An overview of one station, which is repeated 40 times in the final apparatus.

several times with different targets, increasing the collection of data. This permits also to exploit the tracking stations for the monitoring of the beam direction, having a better control on the system.

A fundamental point is the detector angular resolution. This requirement has a strong impact on the capability of distinguishing muons from electrons, as angular information would be extremely important for this aim. As a matter of fact, there exists an ambiguity region whose extension is determined by the angular resolution itself. Fig.(2.12) groups the distributions of the two scattering angles θ_{left} and θ_{right}, assigned randomly at the two particles, with different angular resolution. It is clear from those plots how the width of the curves and of the region of ambiguity, where $\theta_e \sim \theta_\mu$, are strongly related to this parameter. This highlights the fact that the tracking system itself is not enough for a good particle identification (PID), for this aim the presence of an ECAL and a muon detector could be of fundamental importance.

The angular resolution is related to the spatial resolution of the tracker planes, an angular resolution of 0.02 mrad corresponds to a spatial resolution of 20 μm, which can be achieved with state-of-the-art silicon detectors.

The sensitive planes in a single station are three, each of them embedded with two sensors to measure the orthogonal coordinates to the beam direction (x, y). The middle plane is rotated to solve reconstruction ambiguities.

The choice of the silicon detector has been made looking at the sensors and electronics (needed for the trigger) available on the market, already designed for current experiments. The chosen one is the one for the CMS Outer Tracker (OT), being developed for the LHC high-luminosity upgrade, in particular the 2S modules of the CMS OT in
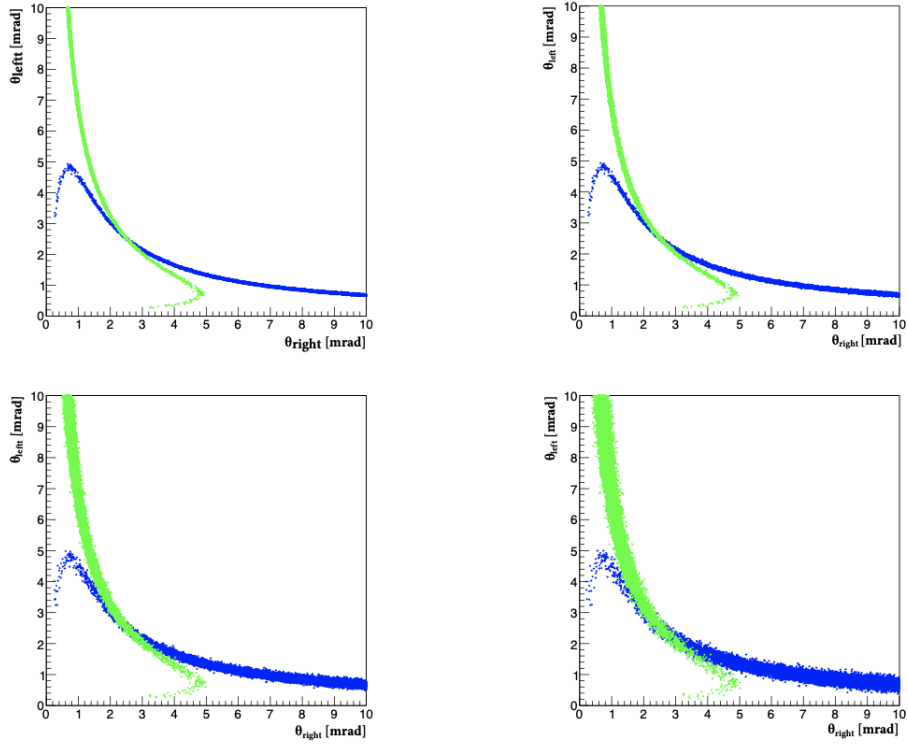
Figure 2.12: Distribution of two measured scattering angles for events simulated with different angular resolution: i) top-left ideal angular resolution (only MCS effect); ii) top-right angular resolution of 0.02 mrad; iii) bottom-left angular resolution of 0.06 mrad; iv) bottom-right angular resolution of 0.1 mrad. In green the point with correct $\mu - e$ identification, while in blue with the wrong ID [25].

Fig.(2.13). The main characteristics are:

1. the whole coverage of the active area: 10 cm × 10 cm;

2. sensor thickness of 320 µm, with strip pitch of 90 µm and segmentation in 5 cm long strips;

3. 1016 strips at each side of the sensor which are read out by 8 ASIC chips (CBC) giving 2032 channels for an high-rate read out;

4. two closely-spaced silicon sensors reading the same coordinate are mounted together (with a gap of 1.8 mm) on the module and read out by common front-end CBC ASICs to correlate the hits from the two sensors (triggering purpose).
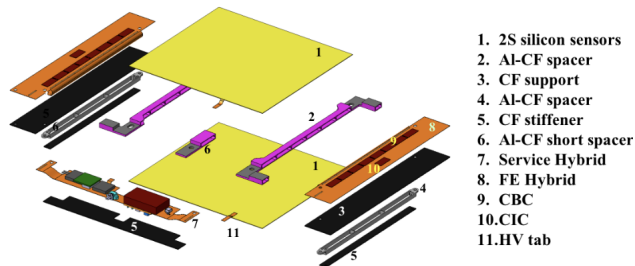
Figure 2.13: An exploded view of the CMS 2S module with the different components.

2.4.2 Electromagnetic Calorimeter

The ECAL does not cover the whole acceptance of the elastic scattering, but the choice of adding it to the apparatus is motivated by the following reasons:

1. PID is necessary particularly in the region of ambiguity ($\theta_e \sim \theta_\mu$) where the information of the angle of scattering given by the tracking system is not enough. Feasible techniques exploit the measurement of the electron scattering angle, obtained by the impact point of the EM shower, or the measurement of the electron energy, which allows to determine the kinematics of the elastic scattering;

2. Electron energy measurement gives a countercheck of the results, helping in the control of systematic effects and the background;

3. Event selection which can be based on energy thresholds or on the number of showers present for the same event (e.g. if the event is $e + \gamma$ it could results in two different showers).

The proposed calorimeter is homogeneous and placed after the 40 tracking stations. It is composed by lead tungstate ($PbWO_4$) crystals with a section of 2.85×2.85 cm^2 and of length $\sim 25\ X_0$, read out by solid state sensors. The points of strength of this material are the fast light scintillation emission time, the good light yield and the compact dimension. As a matter of fact, the ECAL transverse dimension would be of the order of 1×1 m^2 which is enough to contain the angular region where the identification is ambiguous (in particular for $\theta_e \leq 5$ mrad). With that area, full containment is achieved fo electron with energy $E \gtrsim 30$ GeV, while angular acceptance is for $E \gtrsim 10$ GeV.

Another important role of the calorimeter could be to help in getting rid of background events, as electron-positron pair production and nuclear interactions within the targets, and radiative processes ($\mu e \rightarrow \mu e + N\gamma$).

Chapter 3

Fast simulation of the kinematical properties of the beam

The M2 muon beam for the MUonE experiment, available at the CERN North Area, has an optimal momentum value of 160 GeV with $\sigma_p = 6$ GeV/c. As it is shown in the Letter Of Intent (LOI) [25], the beam spot at the entrance of the experiment has a spread of $\sigma_x = 26$ mm on the x axis and of $\sigma_y = 27$ mm on the y one (Fig.(3.1)), while the angular divergence is $\sigma_{x'} = 0.27$ mrad on the XZ plane and $\sigma_{y'} = 0.20$ mrad on the YZ plane (Fig.(3.2)). The beam parameters have been used to simulate the interaction of muons
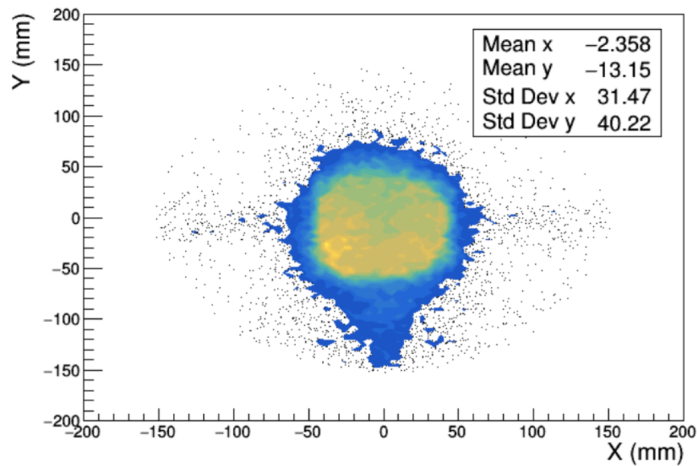
Figure 3.1: Beam Spot size at MUonE with $\sigma_x = 26$ mm and $\sigma_y = 27$ mm .

and the response of the detector, in particular of the electromagnetic calorimeter.
This chapter describes how in this thesis work the beam spot size and divergence have been considered and applied on the MC events simulated with the full set of NLO corrections [28]. It will highlight the effects that these kinematical properties of the beam
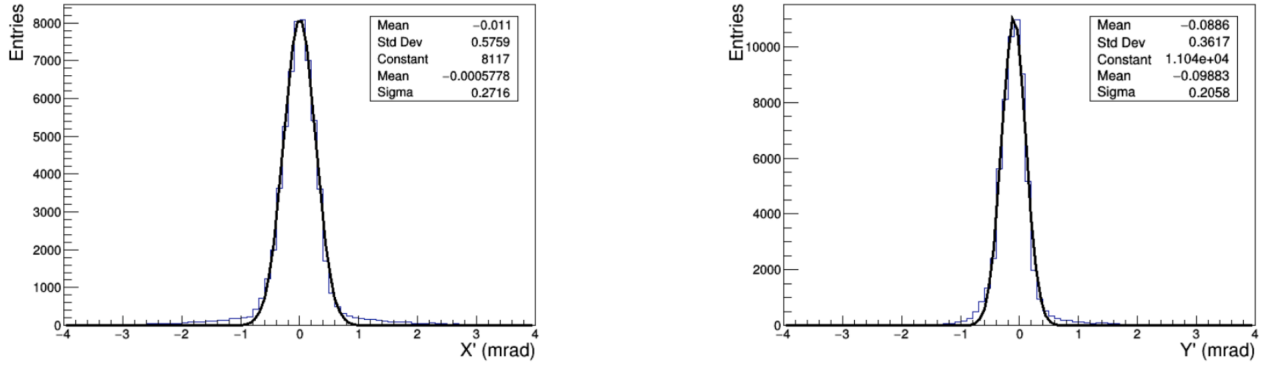
Figure 3.2: Beam divergence at MUonE with $\sigma_{x'} = 0.27$ mrad and $\sigma_{y'} = 0.20$ mrad.

have on some observables as the momenta of the incoming and outgoing particles, the polar angles and the coordinates of the impact points at the entrance of the calorimeter. The events generated with the NLO MC code have particular characteristics:
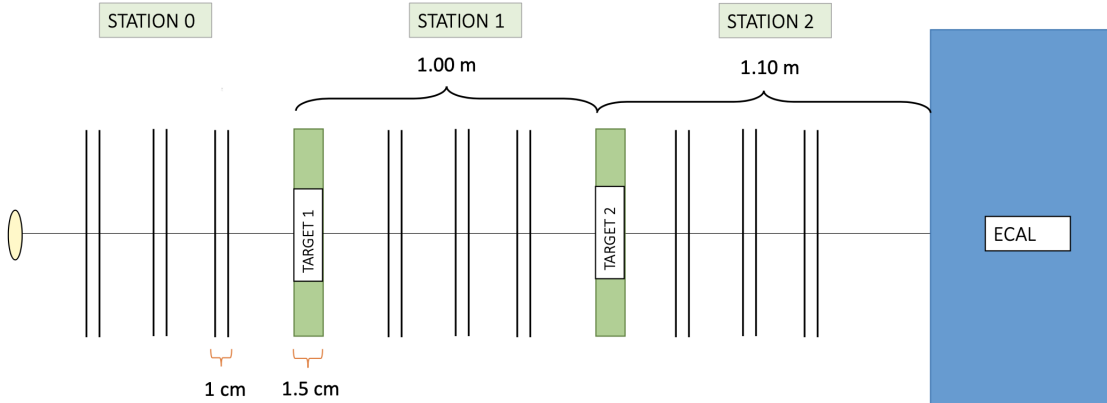
Figure 3.3: Setup for the TestRun 2021 of the MUonE experiment. The stations are composed by silicon trackers while targets are made of Beryllium.

- The momentum is along the *z-axis*;

- The energy distribution of the incoming muon has a Gaussian spread of 3% around the central value of 150 GeV ;

- The generation was done without any simulation of the beam size and divergence;

- The electron energy has a generation cut at $E_e > 0.2$ GeV.

41

Since the experiment is designed to cover the angular region up to $\theta_e \sim 30$ mrad, a preselection cut has been applied, accepting events with the electron scattering angle $\theta_e < 50$ mrad.

These events need to be propagated inside the experimental setup in order to evaluate detector effects, in particular the Multiple Coulomb Scattering (MCS) of the material budget. No energy loss effects (e.g. bremsstrahlung) have been considered instead, hence particles conserve their energies all along their paths. The considered setup is shown in Fig.(3.3) which is the one proposed for the TestRun 2021. It consists in three stations (Station 0, 1, 2) made of six 2S modules with an active area of 10×10 cm^2 needed for tracking particles and two Beryllium targets in which muons interact. ECAL is located downstream the tracking region, at a distance $d = 10$ cm from the last silicon sensor.

3.1 Multiple Coulomb scattering
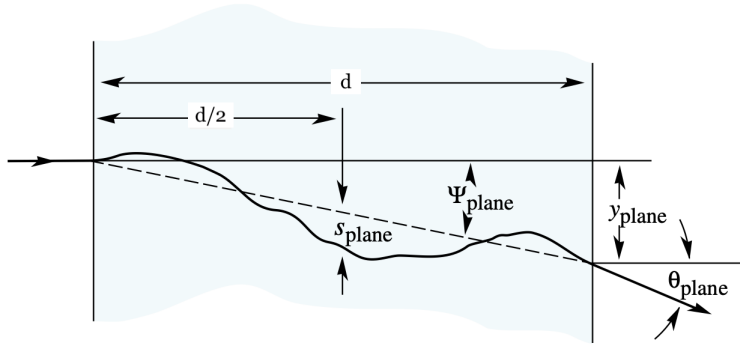
Figure 3.4: The particle is incident in the plane of the figure and affected by MCS. The main quantities used for the description are shown.

Charged particles traversing a material are deflected by many small-angle scatterings with the atoms of the medium. The net scattering and displacement distributions are Gaussian according to the central limit theorem and are well-represented by the theory of Moliére [35].

Defining [11]:

$$\theta_0 = \theta_{plane}^{RMS} = \frac{1}{\sqrt{2}}\theta_{space}^{RMS},\tag{3.1}$$

it is enough for many application to use a Gaussian approximation for the generation of the exit projected angle θ_{plane} in Fig.(3.4), with a RMS given by:

$$\theta_0 = \frac{13.6}{E\,(\text{MeV})}\sqrt{\frac{d}{X_0}}\left[1 + 0.038 \cdot \ln\frac{d}{X_0}\right]\tag{3.2}$$

where E is the energy of the particle, X_0 is the radiation length inside the material and d the thickness of the traversed medium.

Coordinates of the exit points turn out to be displaced with respect the impact points since particles trajectories are perturbed by the medium. In order to account for this effect, looking at Fig.(3.4), the RMS lateral deviation y_{plane} is found to be:

$$y_{plane}^{RMS} = \frac{1}{\sqrt{3}} d\, \theta_0. \tag{3.3}$$

In this thesis work, every time that a charged particle traverses a target or a silicon layer, the effect of the MCS is simulated with the generation of the $i-th$ exit angles on the X and Y plane, θ_{XZ}^i and θ_{YZ}^i, according to a Gaussian distribution with sigma θ_0:

$$\begin{aligned} \theta_{XZ}^i &\to \text{Gauss}(\,\theta_{XZ}^{i-1},\,\theta_0), \\ \theta_{YZ}^i &\to \text{Gauss}(\,\theta_{YZ}^{i-1},\,\theta_0). \end{aligned} \tag{3.4}$$

While the exit coordinates x_{out}^i and y_{out}^i are generated according to a Gaussian distribution with sigma y_{plane}^{RMS}:

$$\begin{aligned} x_{out}^i &\to \text{Gauss}(x_{in}^i,\, \frac{1}{\sqrt{3}} d\, \theta_0), \\ y_{out}^i &\to \text{Gauss}(y_{in}^i,\, \frac{1}{\sqrt{3}} d\, \theta_0), \end{aligned} \tag{3.5}$$

where x_{in}^i and y_{in}^i are the entering coordinates in the material.

3.2   Simulation of the beam divergence

The muon beam has a small angular divergence, hence the direction of the incoming muons, ideally $\vec{P}_{in} = (P_x, P_y, P_z) = (0, 0, P_z)$, needs to be rotated of an angle in agreement with the angular divergence of the beam. Therefore, a change of the reference system is required with a redefinition of the momenta of all the outgoing particles from the interactions in the targets: muons, electrons and radiative photons. The redefinition of the momenta in the new reference system can be realized through a rotation matrix R. First of all, the incoming muon momentum is modified such that $\vec{P}_{in} = (0, 0, P_z) \to \vec{P}_{in}' = (P_x', P_y', P_z')$ with the generation of two random angles:

$$\begin{aligned} \theta_x &\to \text{Gauss}(0, \sigma_{x'}) \\ \theta_y &\to \text{Gauss}(0, \sigma_{y'}) \end{aligned} \tag{3.6}$$

from a Gaussian centered in zero and with two-dimensional spread determined by the beam divergences $\sigma_{x'} = 0.27$ mrad and $\sigma_{y'} = 0.20$ mrad. The new components of the

incoming muon momentum are calculated according to:

$$\begin{cases} P'_z = \sqrt{\frac{|\vec{P}_{in}|}{1+tan^2(\theta_x)+tan^2(\theta_y)}} \\ P'_x = P'_z \tan(\theta_x) \\ P'_y = P'_z \tan(\theta_y) \end{cases} \tag{3.7}$$

maintaining the absolute value of the momentum constant ($|\vec{P}'_{in}| = |\vec{P}_{in}|$). This vector will now determine the angles ψ and φ defining the rotation matrix R.

As a matter of fact, in order to have the momenta of the outgoing particles in the
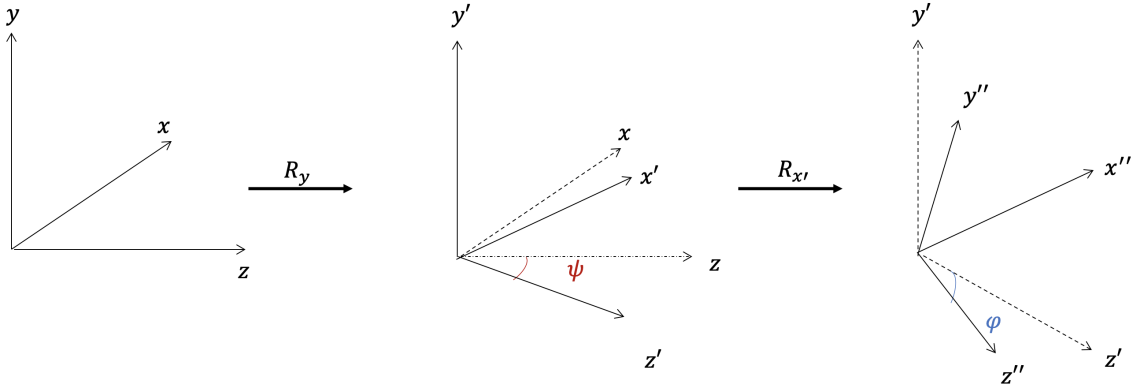
Figure 3.5: Rotation of the reference system due to the angular divergence of the beam. The first rotation R_y is around the y axis of an angle ψ, while the second R'_x is around the new x' axis of an angle φ.

reference system of the divergent beam, the matrix is defined as the product of two rotations:

1. the first one clockwise of an angle $\psi = \arctan(\frac{P'_x}{P'_z})$ around the y axis;

2. the second one clockwise of an angle $\varphi = \arctan(\frac{P'_y}{PT'_z})$ around the new x' axis, where $PT'_z = \sqrt{P'^2_x + P'^2_z}$.

as shown in Fig.(3.5).
The first rotation matrix R_y is defined as:

$$R_y = \begin{pmatrix} \cos\psi & 0 & \sin\psi \\ 0 & 1 & 0 \\ -\sin\psi & 0 & \cos\psi \end{pmatrix} \tag{3.8}$$

hence, in the new reference system a given vector $\vec{p} = (x, y, z)$ results in $\vec{p}\,' = (x', y', z')$

$$\begin{pmatrix} x' \\ y' \\ z' \end{pmatrix} = \begin{pmatrix} \cos\psi & 0 & \sin\psi \\ 0 & 1 & 0 \\ -\sin\psi & 0 & \cos\psi \end{pmatrix} \begin{pmatrix} x \\ y \\ z \end{pmatrix}. \tag{3.9}$$

Now, the matrix $R_{x'}$ of the second rotation

$$R_{x'} = \begin{pmatrix} 1 & 0 & 0 \\ 0 & \cos\varphi & \sin\varphi \\ 1 & -\sin\varphi & \cos\varphi \end{pmatrix} \tag{3.10}$$

will act on $\vec{p}\,' = (x', y', z')$ in such a way that $\vec{p}\,'' = (x'', y'', z'')$ results as the new vector in the reference frame of the divergent beam:

$$\begin{pmatrix} x'' \\ y'' \\ z'' \end{pmatrix} = \begin{pmatrix} 1 & 0 & 0 \\ 0 & \cos\varphi & \sin\varphi \\ 1 & -\sin\varphi & \cos\varphi \end{pmatrix} \begin{pmatrix} x' \\ y' \\ z' \end{pmatrix}. \tag{3.11}$$

It is now possible to define the rotation matrix which transforms a given vector in the initial reference frame $\vec{p} = (x, y, z)$, into the new one in the system of the divergent beam:

$$R = R_{x'} R_y = \begin{pmatrix} \cos\psi & 0 & \sin\psi \\ -\sin\varphi \sin\psi & \cos\varphi & \sin\varphi \cos\psi \\ -\cos\varphi \sin\psi & -\sin\varphi & \cos\varphi \cos\psi \end{pmatrix}. \tag{3.12}$$

As a result, the coordinates of the new vector come from the action of the matrix on the vector $\vec{p}$ such that $\vec{p}\,'' = R\,\vec{p}$ giving

$$\begin{cases} x'' = \cos\psi\,\boldsymbol{x} + \sin\psi\,\boldsymbol{z} \\ y'' = -\sin\varphi \sin\psi\,\boldsymbol{x} + \cos\varphi\,\boldsymbol{y} + \sin\varphi \cos\psi\,\boldsymbol{z} \\ z'' = -\cos\varphi \sin\psi\,\boldsymbol{x} - \sin\varphi\,\boldsymbol{y} + \cos\varphi \cos\psi\,\boldsymbol{z}. \end{cases} \tag{3.13}$$

To be a real rotation matrix, it needs to belong to $SO(3)$, therefore it has to be special orthogonal and it can be checked verifying the property $AA^T = I$ which characterizes all the orthogonal matrices:

$$RR^T = \begin{pmatrix} cos\,\psi & 0 & sin\,\psi \\ -\sin\varphi \sin\psi & \cos\varphi & \sin\varphi \cos\psi \\ -\cos\varphi \sin\psi & -\sin\varphi & \cos\varphi \cos\psi \end{pmatrix} \cdot \begin{pmatrix} \cos\psi & -\sin\varphi \sin\psi & -\cos\varphi \sin\psi \\ 0 & \cos\varphi & -\sin\varphi \\ \sin\psi & \sin\varphi \cos\psi & \cos\varphi \cos\psi \end{pmatrix} =$$

$$= \begin{pmatrix} c^2\psi + s^2\psi & -c\psi\,s\varphi s\psi + s\psi\,s\varphi c\psi & -c\psi\,c\varphi s\psi + s\psi\,c\varphi c\psi \\ -s\varphi\,s\psi\,c\psi + s\varphi c\psi\,s\psi & s^2\varphi s^2\psi + c^2\varphi + s^2\varphi c^2\psi & s\varphi\,s^2\psi\,c\varphi - s\varphi c\varphi + s\psi\,c^2\psi c\varphi \\ -c\varphi\,s\psi\,c\psi + c\varphi c\psi\,s\varphi & c\varphi\,s^2\psi s\varphi - s\varphi c\varphi + c\varphi c^2\psi s\varphi & c^2\varphi s^2\psi + s^2\varphi + c^2\psi c^2\varphi \end{pmatrix} =$$

$$= \begin{pmatrix} 1 & 0 & 0 \\ 0 & 1 & 0 \\ 0 & 0 & 1 \end{pmatrix} \tag{3.14}$$

45

Furthermore, it implies that $det\,R = 1$:

$$det\,R = \cos^2\psi\,\cos^2\varphi + \sin^2\varphi\,\sin^2\psi + \sin^2\varphi\,\cos^2\psi + \sin^2\psi\,\cos^2\varphi =$$
$$= \cos^2\psi\,(\cos^2\varphi + \sin^2\varphi) + \sin^2\psi\,(\sin^2\varphi + \cos^2\varphi) \qquad (3.15)$$
$$= 1,$$

hence R is a rotation matrix belonging to $SO(3)$.

The correctness of the rotation R has been verified by checking that its application
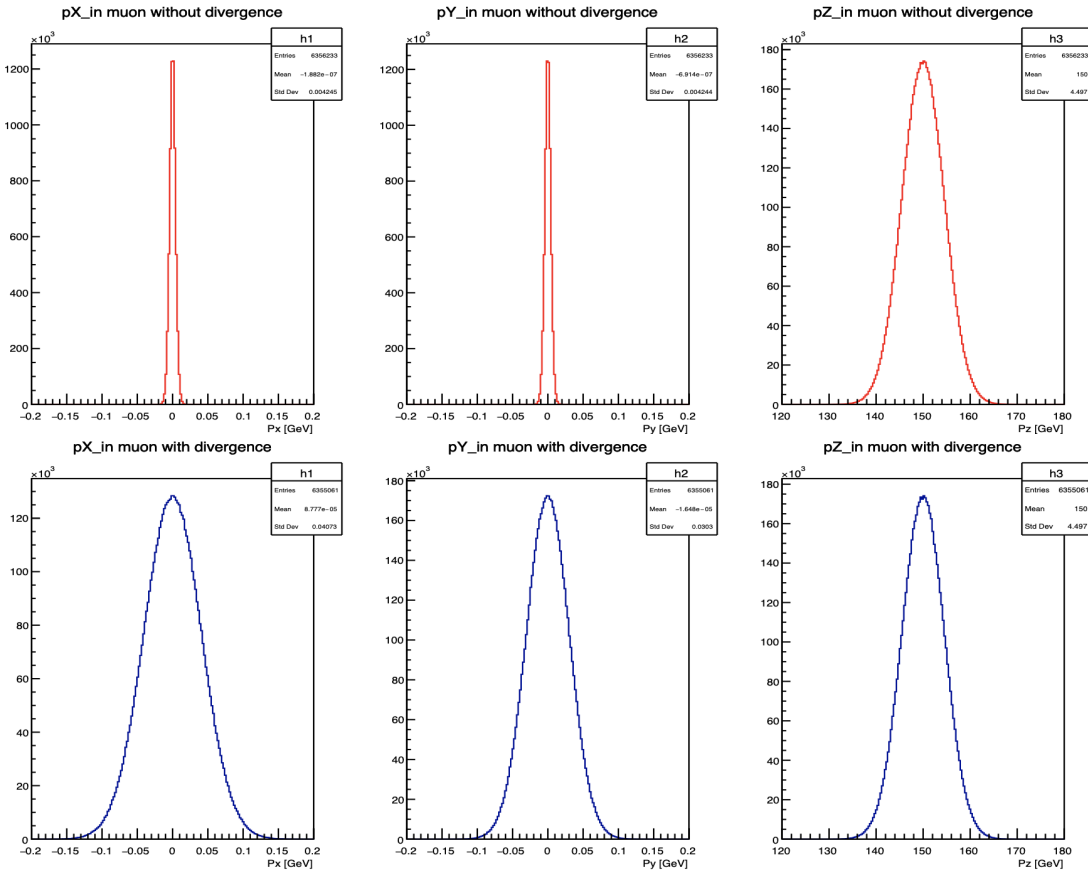
Figure 3.6: Distributions of the three components of the incoming muon momentum from the NLO events without (top plots) and with (bottom plots) the simulation of the angular divergence of the beam. Beam muons are simulated to interact randomly in one of the two targets.

to the initial muon momentum $P_{in} = (0, 0, P_z)$ gives the same result as the smeared momentum P'_{in} obtained initially with Eq(3.7). Then the rotation obtained in this way event-by-event has been applied to the momenta of all the outgoing particles in order to have them in the reference system of the divergent beam.

46

Fig.(3.6) shows the distributions of the momentum components for the incoming muons before and after applying the simulation of the beam divergence. They refer to muons interacting either in Target 1 or 2, therefore the spread in p_x and p_y is given by MCS due to the passage across Station 0, if the interaction happens in Target 1, or across Station 0, Target 1 and Station 1, if the interaction happens in Target 2. The effect of the beam divergence is of the order of $30 - 40$ MeV on the transverse components, therefore there is no visible effect on the distribution of the p_z component.

3.3   Simulation of the Beam Spot

Incoming muons are assumed to interact in one of the two Beryllium targets. In order to simulate realistic scenarios, the target will be selected in a random way, and the depth at which the interaction occurs will be chosen randomly with a uniform distribution. The reference point $z_0 = 0$ is taken at the beginning of the Station 0, which is distant $z_1 = 1.00$ m from the next one. The distance between the calorimeter and the last silicon layers is $z_2 = 0.10$ m.

In order to include the spread of the beam in the x and y direction, two random

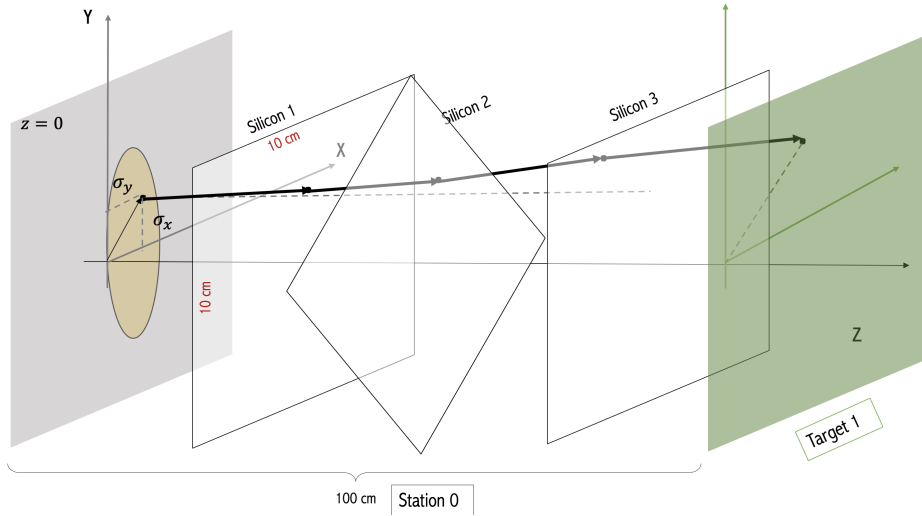Figure 3.7: The picture shows an event where the beam spot size (yellow) is taken into account, it influences the value of the impact coordinates of the particles.

coordinates are generated with Gaussian distributions centered in the origin and with spread $\sigma_x = 2.6$ cm and $\sigma_y = 2.7$ cm:

$$\begin{aligned} x_R &\to \mathrm{Gauss}(0, \sigma_x) \\ y_R &\to \mathrm{Gauss}(0, \sigma_y). \end{aligned} \tag{3.16}$$

47

Muons in Station 0 are propagated from this initial random position (x_R, y_R) and then all along the tracking stations until the interaction in one of the two targets happens (Fig.(3.7)). Only events where the muon interacts at a radius $r_\mu < 5$ cm will be considered in order to take into account the sensors' dimensions. After that, propagation keeps on with the outgoing particles (e, μ and eventually γ) until the ECAL is reached. As aforementioned, in this propagation step the effect of the MCS was implemented for the charged leptons, modifying the direction of their momenta. While photons, when produced, are propagated as a straight line all along the tracker.

The simulation of the beam spot size has a significant effect on some observables. Fig.(3.8) shows the distributions of the particle positions at the entrance of the calorimeter without (top row) and with (bottom row) the simulation of the beam spot and divergence. Neglecting the beam profile, the distributions are determined just by the $\mu - e$ scattering process and the MCS. The size of the beam and the angular divergence give a contribution bringing to a wider distribution for all the three types of particle.
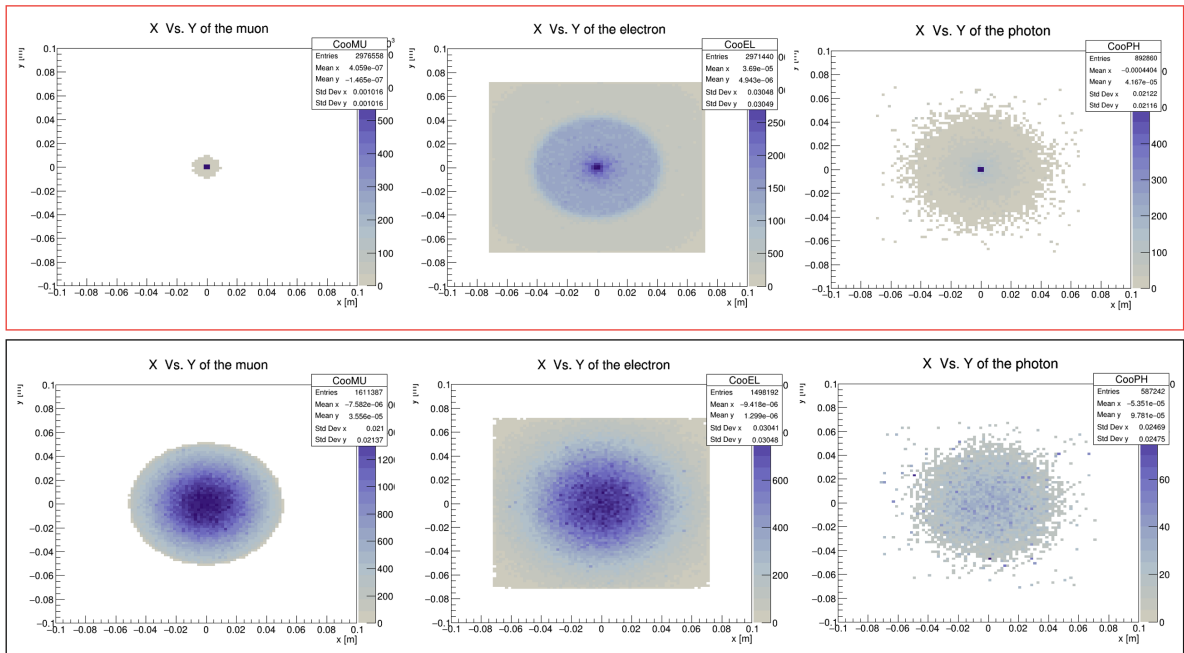

Figure 3.8: Distributions of the coordinates for the outgoing muons, electrons and photons at the entrance of the ECAL. In the top box the distributions without the effect of the kinematical properties of the beam, in the bottom one with the effects applied.
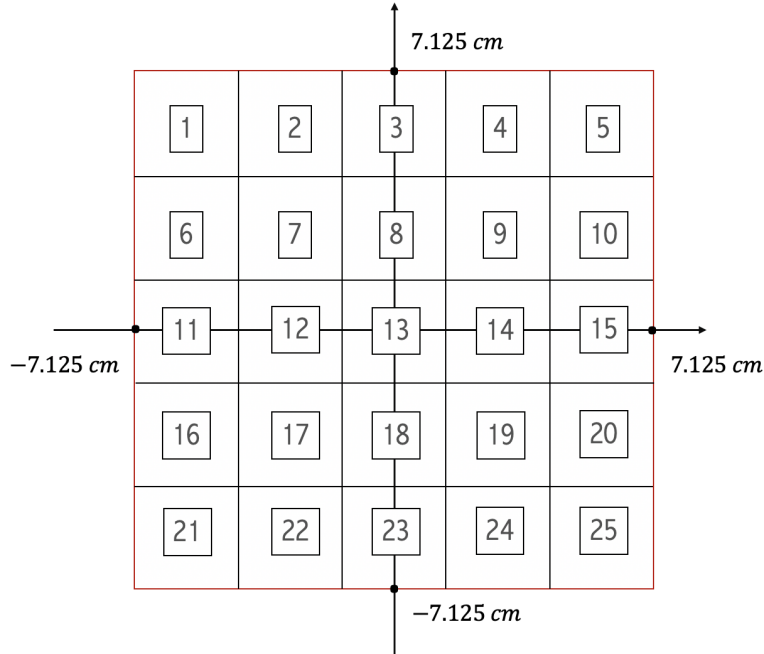
3.4 Relevant observables

Figure 3.9: Sketch of the transversal face of the MUonE ECAL foreseen at the TestRun 2021. It is a 14×14 cm^2 array of 25 $PbWO_4$ crystals.

Now that we know how to simulate the kinematical properties of the beam and the propagation step for the particles produced in the NLO collissions, we want to understand their properties at the entrance of the ECAL. We aim to establish to what extent the calorimeter would help in the separation and discrimination of the outgoing particles. We require events to satisfy the following geometrical conditions:

1. A cut on electron's scattering angle is applied at the generated level requiring it to be less than 50 mrad.

2. The silicon sensors have a surface of 10×10 cm^2, the incoming muons are imposed to be inside the sensors' fiducial volume;

3. ECAL has a surface of 14×14 cm^2 (Fig.(3.9)), the restriction is imposed on the impact points of the impinging particles.

In this work, events are taken into account only when an electron impacts the ECAL. Observables used to characterize events selected according to the previous criteria are:

- Angles of electrons and muons in the XZ and YZ planes;

- The polar angles of outgoing electrons and muons;

- The impact coordinates of outgoing electrons, muons and photons;

- The energy of the outgoing particles.

Interactions can occur in Target 1 or in Target 2, therefore it is important to consider the two situations individually in order to understand the different topologies of the events in the two cases.

In Fig.(3.10) the distributions of the angles on the XZ and YZ planes for both the

Figure 3.10: Distribution of the angles on XZ and YZ planes for muons (left plots, in red) and electrons (right plots, in blue). Events coming from Target 1 are represented in green, while from Target 2 in black.

electrons and muons are presented. There are more events coming from the second target, due to the geometry of the setup which impose different angular acceptances for events produced in the two stations. Target 1 is farther than Target 2 from the ECAL, therefore outgoing particles with larger angles produced in the first target are more likely to go outside the calorimeter acceptance.

Not all the events which have been generated are useful for the final measurement, in particular, all the ones with electron energy less than $\sim 1\,\mathrm{GeV}$ are more subjected to
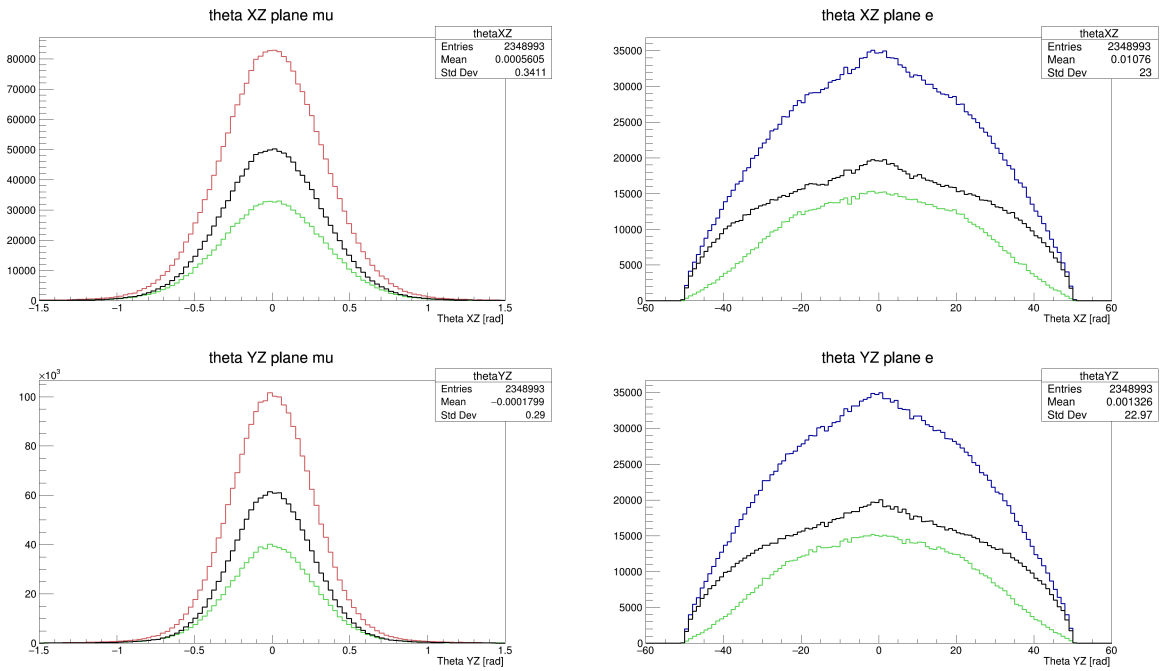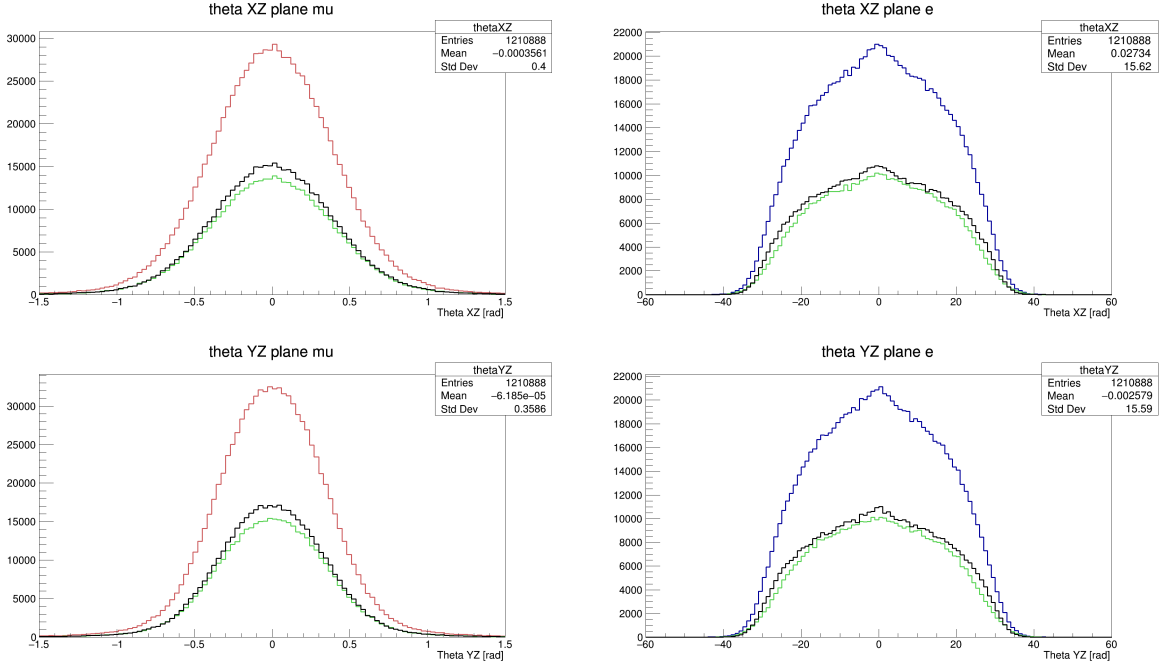
Figure 3.11: Distribution of the angles on XZ and YZ planes for muons (left plots, in red) and electrons (right plots, in blue) with a cut on the energy measured by the calorimeter at $E_{ECAL} \geq 1$ GeV. Events coming from Target 1 are represented in green, while from Target 2 in black.

experimental perturbations and related systematics. In addition, they are not interesting for the physical case under study, since events at large electron's scattering angle do not provide information about the running. Therefore, it it is useful to impose a cut on the energy measured by the calorimeter to $E_{ECAL} \geq 1$ GeV. As it is shown in Fig(3.11) events generated in Target 2 are reduced: a large fraction of electrons produced at the first target and at large angles fly off the calorimeter acceptance; when produced at the second target they can be mainly rejected by applying the energy threshold.

In Fig.(3.12), plots of the polar angles with respect to the *z-axis* are shown for muons and electrons arriving at the ECAL. The distinction of events coming from Target 1 and 2 is made and here no energy cut is imposed. It is interesting to notice the effect of the geometrical acceptance in the distribution of the electron's polar angle: figure shows that there are two bumps for electrons coming from Target 1 and 2 at different angles. Given the proximity of Target 2 to the ECAL, the distribution increases up to about ~ 50 mrad, while for Target 1 the maximum is around ~ 25 mrad. There is no difference in the muon angle distribution, as this is much smaller than the acceptance of the detector (order of 1 mrad versus 10 mrad).

51

Figure 3.12: Distributions of the polar angle of muon (top panel) and electron (bottom panel) trajectories at the calorimeter entrance. The green histograms represent particles from Target 1, the black histograms from Target 2. The sum of the two contributions is in red for muons and in blue for electrons.

Fig.(3.13) shows the effects of the energy cut $E_{ECAL} \geq 1$ GeV on the muon and electron
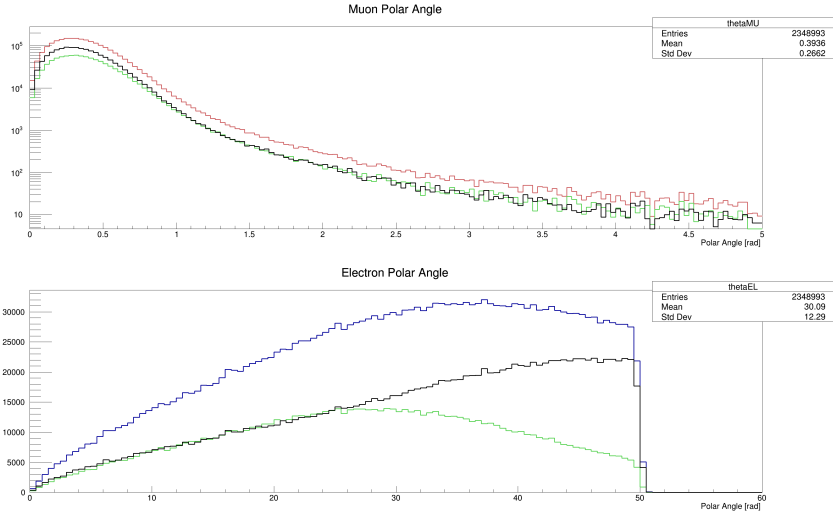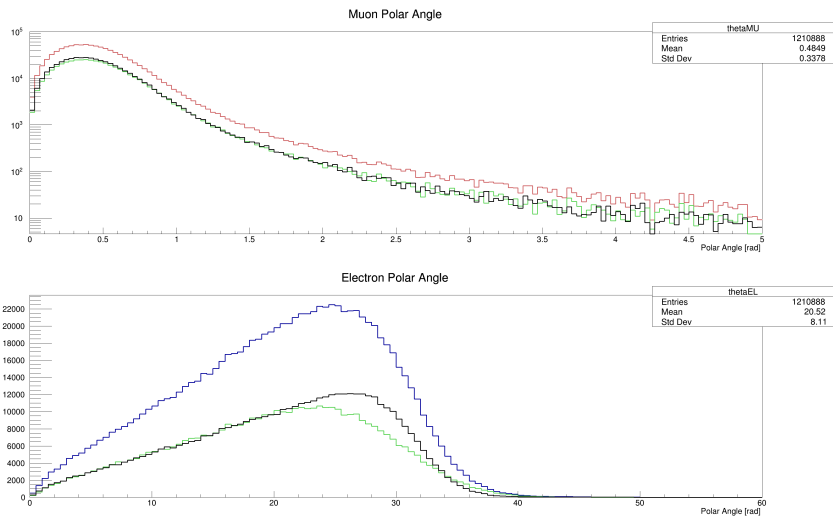

Figure 3.13: Distributions of the polar angle of muon (top panel) and electron (bottom panel) trajectories at the calorimeter entrance, after an energy cut $E_{ECAL} \geq 1$ GeV. The green histograms represent particles from Target 1, the black histograms from Target 2. The sum of the two contributions is in red for muons and in blue for electrons.

52

distributions produced at Target 1 and Target 2. The bottom plot, which refer to the electron distributions, illustrate the cut off of large angle electrons from Target 2.

Fig.(3.14) shows the impact positions of muons, electrons and photons on the front face

Figure 3.14: Distributions of the impact coordinates for muons (first row), electrons (second row) and photons (third row) on the front face of the calorimeter without any cut on the energy. The first column includes all the events, the second just the ones form Target 1 and the last from Target 2.

of the calorimeter. Because of MCS we expect electrons to have a wider distribution than muons. This is what can be observed in this figure, where the outgoing muons preserve the condition of being generated in a radius $r_\mu < 5$ cm, while the shape of the electron distribution is visibly altered by MCS. In particular, electrons from Target 1 have a wider spread as they have to traverse a bigger amount of material, thus are less concentrated in the center.

Fig.(3.15) shows the distribution of impact positions after imposing an energy cut. As expected, this is balancing the yield of electrons coming from Target 1 (second column)
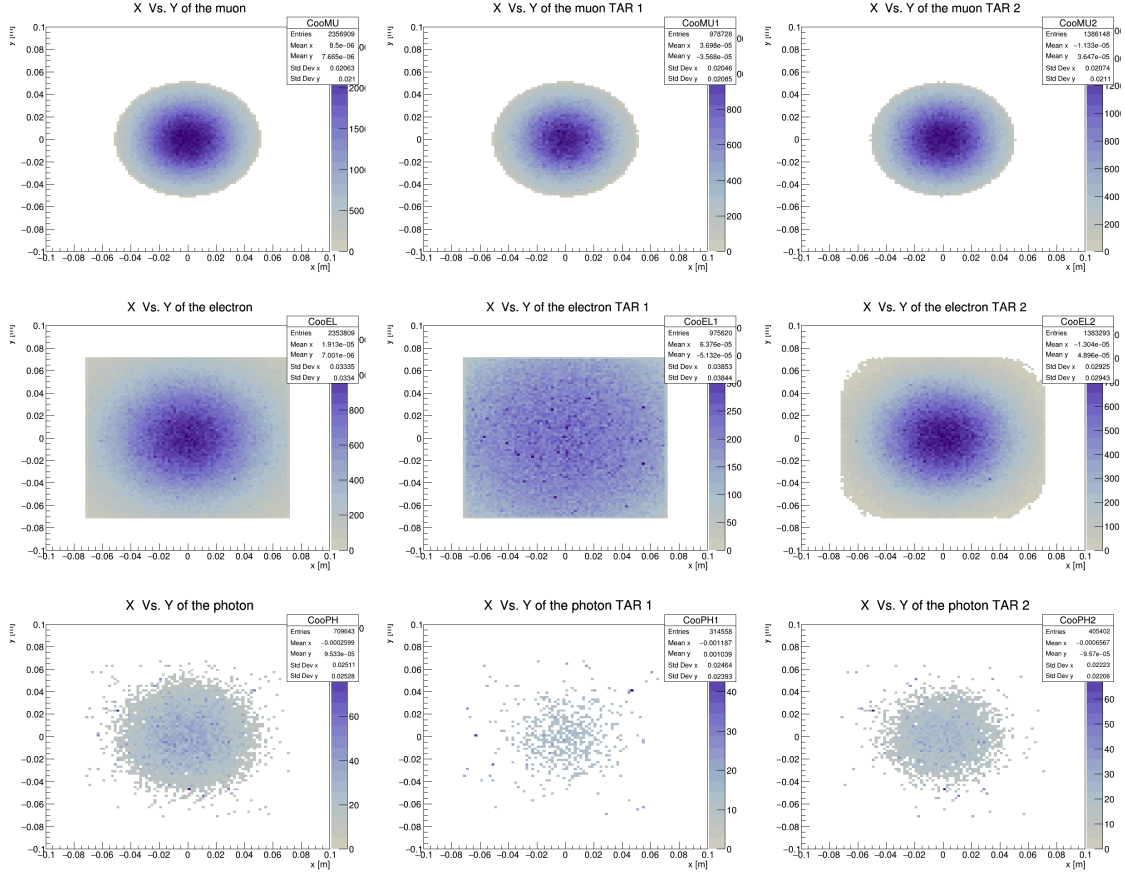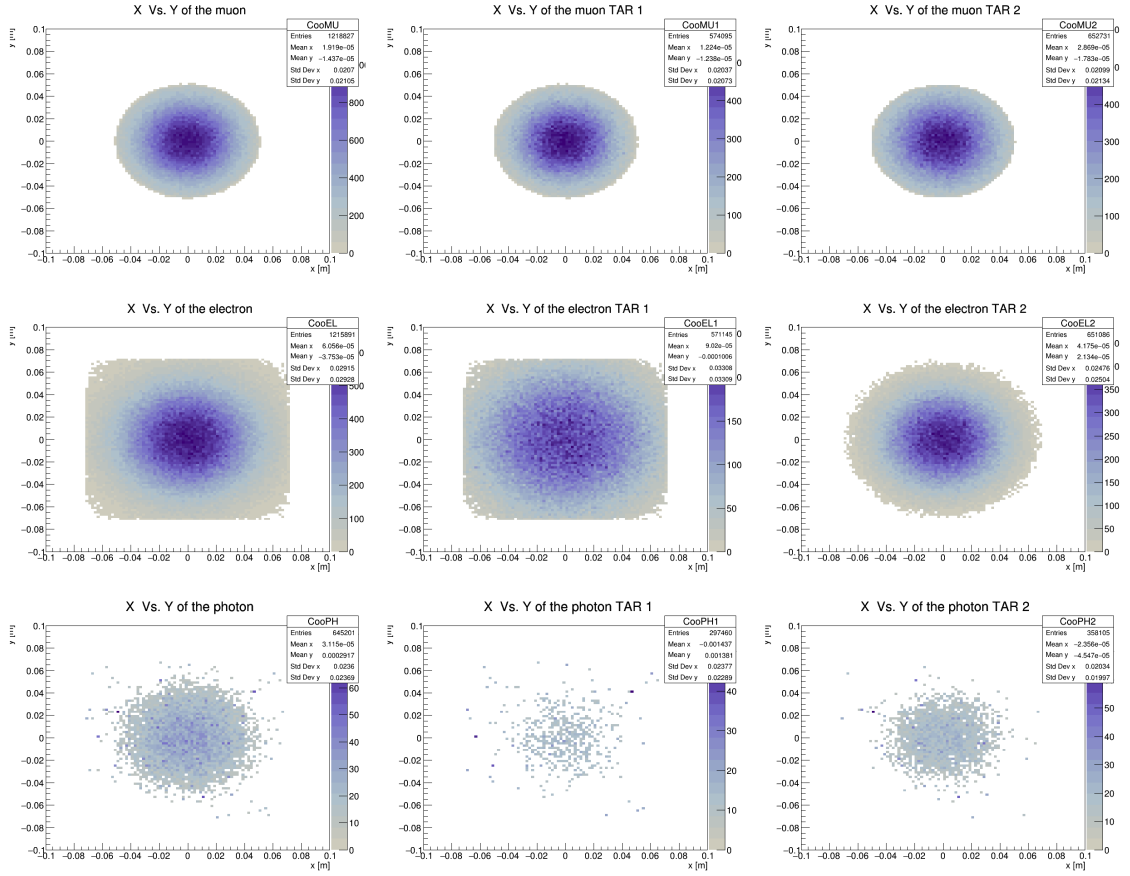
Figure 3.15: Distributions of the impact coordinates for muons (first row), electrons (second row) and photons (third row) with a cut on the energy $E_{ECAL} \geq 1$ GeV. The first column includes all the events, the second just the ones form Target 1 and the last from Target 2.

and from Target 2 (third column).

Finally, the true values of the energies of particles entering into the calorimeter acceptance are shown in Fig.(3.16). The calorimeter is needed to measure the energy of the electron, therefore an algorithm simulating the shower and giving a feedback on the response of the detector is fundamental for the analysis tool, in order to know how well the energy will be reconstructed.

Muons are m.i.p. (minimum ionising particle) and their energy deposition inside the calorimeter is quite independent from their energy. In the final analysis its contribution will be subtracted by the energy measurement of the ECAL, but in this first work it can be neglected.
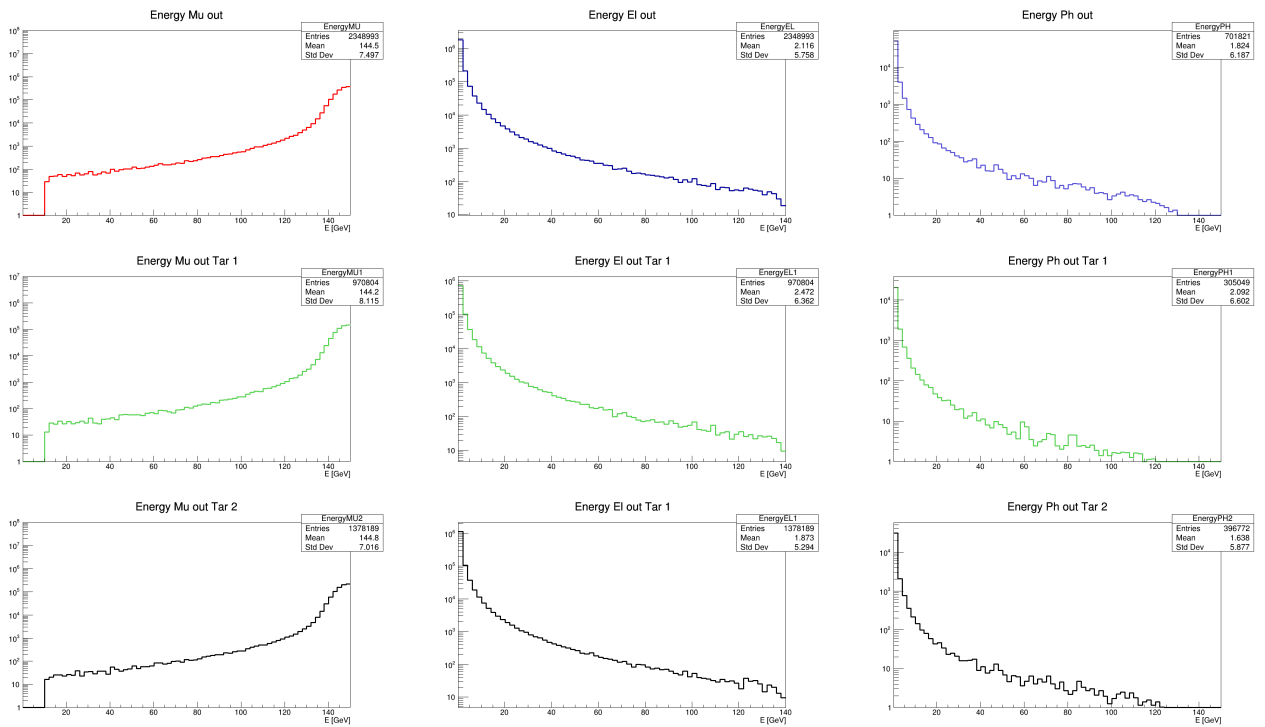
Figure 3.16: Distributions of the energy for muons (first column), electrons (second column) and photons (third column). The first row includes all the events, the second row the ones form Target 1 and the last from Target 2.

Chapter 4

Fast Simulation of the Electromagnetic Calorimeter Response

4.1 Electromagnetic Showers

Electromagnetic calorimeters are detectors used to measure the energy of a particle exploiting the process of electromagnetic showers. The principle is simple: if an electron or a photon enters in the calorimeter with enough energy, above few MeV, it starts to interact with the material's atoms through:

1. Bremsstrahlung (when it is an electron);

2. e^+e^- pair production (when it is a photon).

In this way the shower starts: the electron will radiate a photon which will then produce a pair and so on, while the photon will produce an electron and a positron which will then interact with matter via bremsstrahlung. This process will keep on until the produced particles reach the so called *critical energy E_C*. At this point, electrons will lose energy mainly via the ionization process, while photons through Compton or photoelectric effect, hence the energy loss would be slower.

As shown in Fig.(4.1), the development is characterized by the *radiation length X_0*, which strictly depends on the material and represents the mean free path before the electron radiates a photon. After each radiation length, the energy of the electron is reduced by a factor $1/e$. Differently, the path length after which the photon interacts via pair production is $\frac{9}{7}X_0$, slightly bigger than the one of the electron.
The radiation length is approximately given by:

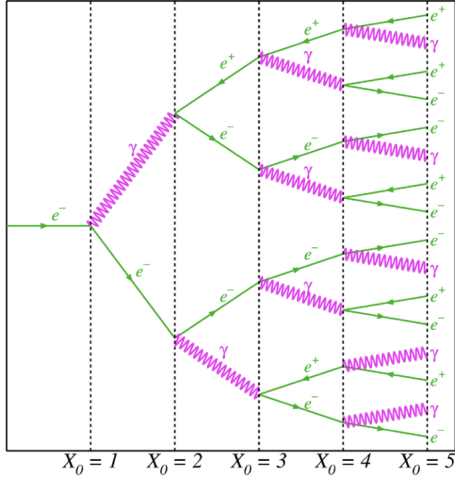$$\frac{1}{X_0} = \frac{4\alpha N_A Z(Z+1)r_e^2 \ln(183Z^{-1/3})}{A} \tag{4.1}$$

Figure 4.1: Simple model of the development of an electromagnetic shower.

where α is the fine structure constant, N_A is the Avogadro's number, r_e is the classical electron radius, Z is the atomic number and A is the atomic weight. The units of X_0 in Eq. 4.1 are [g/cm^2] which, if divided by the material density, can be expressed in units of [cm].

The critical energy E_C is defined as the energy at which the rates of energy loss by radiation and ionization become equal, it has an approximation related to X_0:

$$E_C = 2.66 \left(X_0 \frac{Z}{A} \right)^{1.1} \tag{4.2}$$

below that, ionization dominates.

A third important parameter is the *Moliere radius* R_M which expresses the transversal size of the shower:

$$R_M = X_0 \frac{21.2 \text{ MeV}}{E_C} \tag{4.3}$$

The 90% of the energy is contained within a radius of R_M, which has only a weak dependency on the material.

All those parameters define the development of the shower inside the calorimeter: the radiation length determines the longitudinal depth of the shower, the critical energy sets the value of the energy below which energy loss happens mainly through ionization and the Moliere radius determines the transverse development at different depths. In particular, the electromagnetic showers' evolution is generally parametrized by two profiles: the longitudinal and the transversal one. Those describe the deposition of energy all along the calorimeter. The shower gets wider at higher depths because particles become less energetic hence more subjected to MCS, if positrons or electrons, and Compton or photoelectric effects, if photons. While after the peak, where $E < E_C$, the longitudinal loss of energy gets slower because absorption of particles starts to dominate on creation of secondaries.

4.2 Shower Parametrization

In this study the electromagnetic showers have been modeled with the GFLASH parameterization, proposed by G. Grindhammer and S. Peters for electrons in homogeneous media [36][37]. This method is used in the fast simulation of the CMS ECAL, which is made of the same crystals as the MUonE one and similar readout electronics. The algorithm developed in this thesis work is built up starting from the CMS version. It was adapted for the MUonE geometry and modified to be implemented in the overall fast simulation code. A detailed description of the code is given in Appendix.

The energy distribution of the shower is factorized into three probability density functions (PDF):

$$dE(\vec{r}) = Ef(t)dt f(r)dr f(\phi)d\phi \qquad (4.4)$$

where E is the energy of the impinging particle in units of E_C, $f(t)$ represents the longitudinal profile as a function of t, the shower depth in units of X_0; $f(r)$ describes the radial profile as a function of r, the radial distance in units of R_M, and $f(\phi)$ is the azimuthal distribution which is assumed uniform. All the material-dependent quantities X_0, R_M and E_C are related to the development of the shower and it is possible to eliminate most of the material dependence in the GFLASH parameters by working in units based on those three.
CMS and MUonE ECALs have the same characteristics in terms of material and cells configuration, hence the properties in the next Table are in common:

$\rho = 8.28$ g/cm^3	$X_0 = 7.37$ g/cm$^2 = 0.89$ cm
$A_{eff} = 170.87$	$E_C = 8.74$ MeV
$Z_{eff} = 68.36$	$R_M = 2.19$ cm

A_{eff} and Z_{eff} are calculated by averaging the A and Z of the component elements in $PbWO_4$ weighted by their mass fractions. The length of the crystals is of 22 cm $= 24.7X_0$.

Starting from the relations which describe the average behavior of the parameterized quantities, the authors developed the parameterization for individual electromagnetic showers started by electrons in homogeneous calorimeters, taking fluctuations and correlations into account event-by-event. If the starting particle is a photon, it will be treated as an electron-positron pair, each one producing a shower starting after a random length d after the impact point, related to the photon mean free path.

4.2.1 Longitudinal Parametrization

The average longitudinal profile is described by a gamma distribution:

$$f(t) = \left\langle \frac{1}{E} \frac{dE(t)}{dt} \right\rangle = \frac{(\beta t)^{\alpha-1} \beta e^{-\beta t}}{\Gamma(\alpha)} \tag{4.5}$$

where α and β are respectively the shape and scaling parameters, which can be evaluated with MC full simulations. The center of gravity of the shower $\langle t \rangle$ and the depth of the maximum T are given by:

$$\langle t \rangle = \frac{\alpha}{\beta} \tag{4.6}$$

$$T = \frac{\alpha - 1}{\beta}. \tag{4.7}$$

The depth of the shower maximum is predicted to scale logarithmically with increasing energy, as:

$$T \propto \ln y = \ln \frac{E}{E_C}. \tag{4.8}$$

The shape parameter α depends on Z, being the only one with an explicit dependence on the material. For the other variables, the dependence is absorbed through the use of the quantity $y = \frac{E}{E_C}$ instead of E. In Fig.(4.2) the average depth of the shower maximum on top and α on bottom are plotted as a function of y. The left plots show results obtained by a GEANT full simulation of several homogeneous calorimeters, with the fitted parameterizations [37]:

$$T_{hom} = \ln y + t_1, \tag{4.9}$$

$$\alpha_{hom} = a_1 + (a_2 + a_3/T) \ln y, \tag{4.10}$$

where the values of the coefficients are given in Appendix. The plots on the right are obtained from the MUonE algorithm and are in agreement with the expectations.
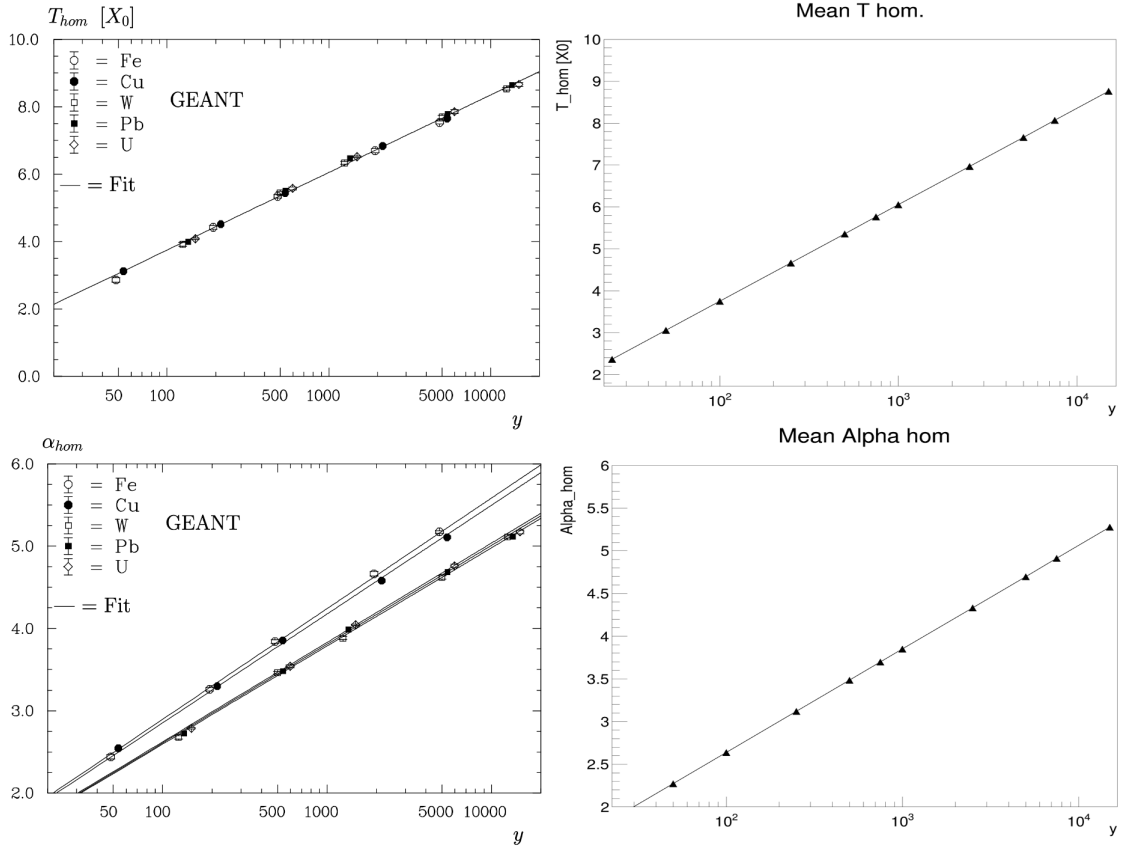
Figure 4.2: Depth of the shower maximum (top) and the shape parameter α (bottom) as a function of y. GEANT full simulation results are shown at left for several homogenous calorimeters [37], while on the right the results from the developed algorithm for the MUonE calorimeter ($PbWO_4$).

Also individual profiles are approximated with a gamma function, but to simulate the single shower event-per-event, fluctuations and correlations between the parameters need to be introduced.

Starting with the y-dependence of the fluctuations, it is defined the variable

$$\sigma = (s_1 + s_2 \ln y)^{-1}, \tag{4.11}$$

while the correlation between α_{hom} and T_{hom} is given by:

$$\rho(\ln T_{hom}, \ln \alpha_{hom}) = r_1 + r_2 \ln y. \tag{4.12}$$

The values for the parameters s_1, s_2, r_1, r_2 are reported in Appendix. The logarithms of T and α are used since they have approximately normal distributions. The variables
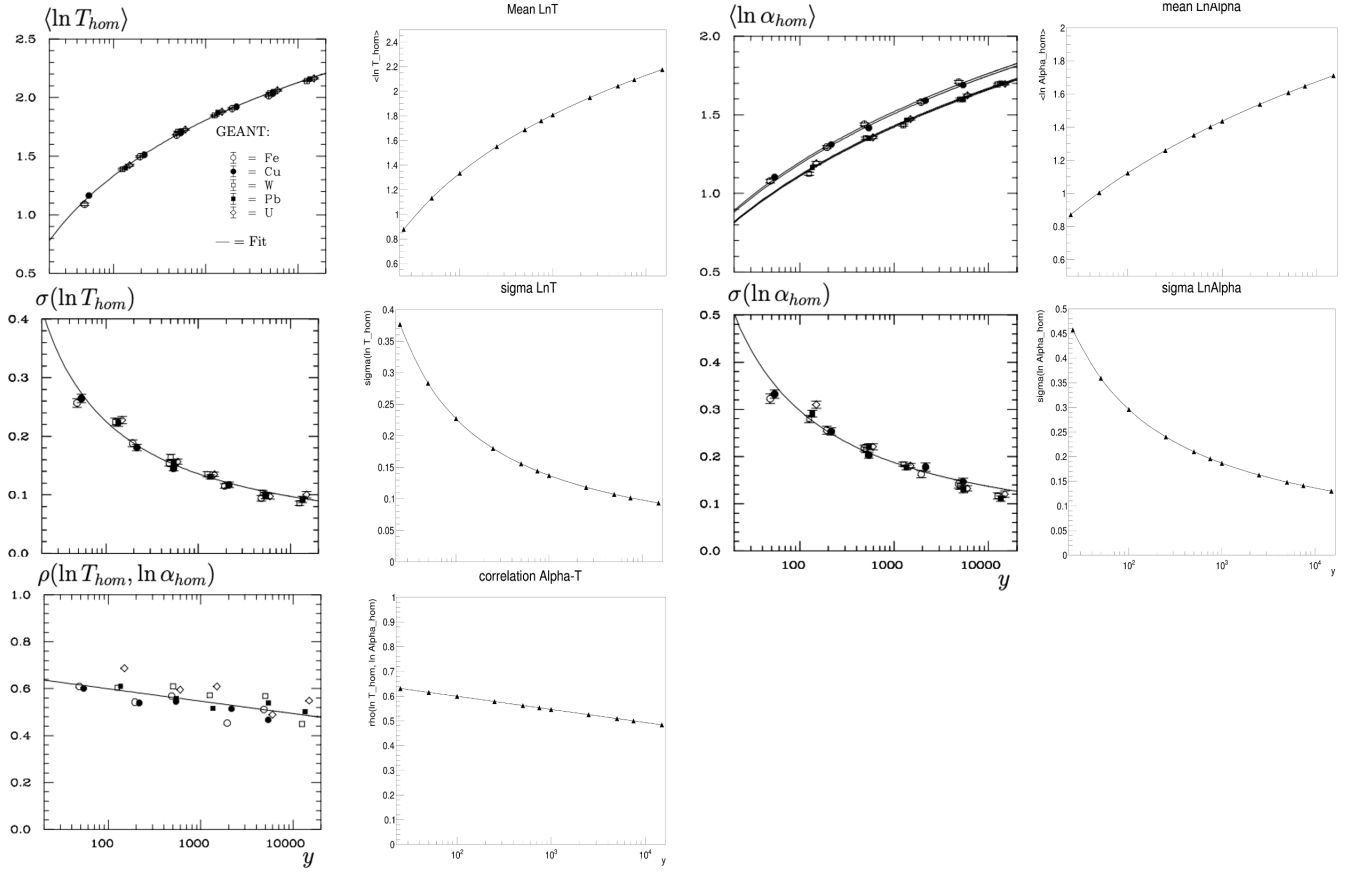
Figure 4.3: Parameters of the longitudinal profiles in homogeneous media: from GEANT in marked black boxes, from the developed algorithm according to MUonE calorimeter ($PbWO_4$) in light gray boxes.

σ and $\rho(\ln T_{hom}, \ln \alpha_{hom})$ will enter in the definition of the single shower parameters to introduce event-by-event characteristics. The energy dependence of these parameters is shown in Fig.(4.3). The results from the algorithm developed for MUonE is in agreement with the expected results from GEANT full simulation in [37].

The parameters α_i and $\beta_i = (\alpha_i - 1)/T_i$ for the individual shower profiles are defined as:

$$\begin{pmatrix} \ln T_i \\ \ln \alpha_i \end{pmatrix} = \begin{pmatrix} \langle \ln T \rangle \\ \langle \ln \alpha \rangle \end{pmatrix} + C \begin{pmatrix} z_1 \\ z_2 \end{pmatrix} \tag{4.13}$$

where $\langle \ln T \rangle$ and $\langle \ln \alpha \rangle$ are given by Eq. 4.9-4.10, z_1, z_2 are random numbers from a

gaussian centered in 0 and with $\sigma = 1$, while C:

$$C = \begin{pmatrix} \sigma(\ln T) & 0 \\ 0 & \sigma(\ln \alpha) \end{pmatrix} \begin{pmatrix} \sqrt{\frac{1+\rho}{2}} & \sqrt{\frac{1-\rho}{2}} \\ \sqrt{\frac{1+\rho}{2}} & -\sqrt{\frac{1-\rho}{2}} \end{pmatrix}. \qquad (4.14)$$

The energy deposited in a longitudinal step $\Delta t = t_j - t_{j-1}$, taken as $1 X_0$, can be evaluated through the integral

$$dE(t) = E \int_{t_{j-1}}^{t_j} dt \frac{(\beta_i t)^{\alpha_i - 1} \beta_i e^{-\beta_i t}}{\Gamma(\alpha_i)}. \qquad (4.15)$$

In Fig.(4.4) the longitudinal profiles from GEANT and from a parameterized simulation

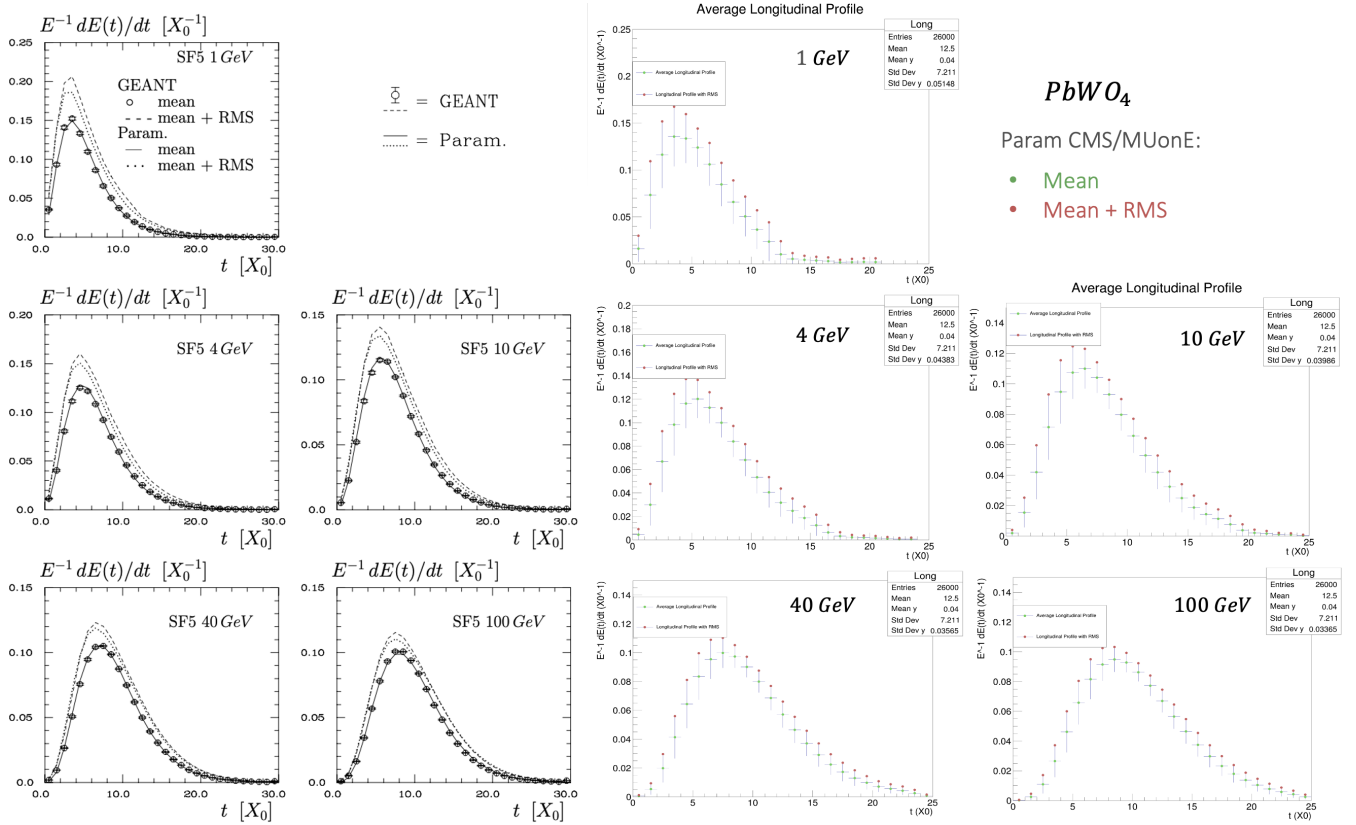Figure 4.4: Mean longitudinal profiles and their fluctuations in a lead glass calorimeter from GEANT and parametrized simulation on the left, from the parametrized simulation according MUonE calorimeter ($PbWO_4$) on the right.

in a lead glass ($SF5$) absorber are shown on the left, while on the right from the parameterized simulation in the MUonE ECAL. GEANT mean profiles agree very well with the

parameterizations. Fluctuations are also parameterized quite well at high energy while they are underestimated at low energies, indicating that the description of individual profiles by gamma distributions becomes a worse approximation with decreasing shower energy. The agreement between the longitudinal profile of a lead glass ($SF5$) calorimeter and the $PbWO_4$ one shows that the chosen parametrization is fairly independent of the used material.

4.2.2 Radial Parametrization

The average radial profile is parameterized with a function composed of two distinct pdfs

$$
\begin{aligned}
f(r) = \frac{1}{E} \frac{dE(t,r)}{dr} = \\
= p \frac{2r R_C^2}{(r^2 + R_C^2)^2} + (1-p) \frac{2r R_T^2}{(r^2 + R_T^2)^2} \,,
\end{aligned}
\tag{4.16}
$$

where the first one describes the core of the radial profile, while the second represents the
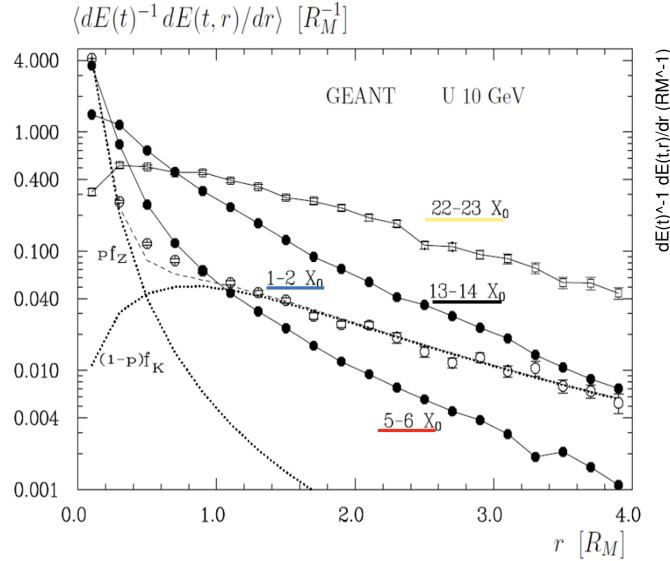
Figure 4.5: Average transverse profiles in an Uranium calorimeter from GEANT at different depths of the shower. It is shown how the tail and core pdfs contribute to the radial profile on the first longitudinal segment $1 - 2\,X_0$ [37].

tail (Fig.(4.5)). The distribution $f(r)$ is characterized by three parameters: i) R_C that is the median of the core, ii) R_T which is the median of the tail, iii) p which represents the weight of the core in the overall function.

  In Fig.(4.6) it is presented the behavior of the parameters increasing the shower depth
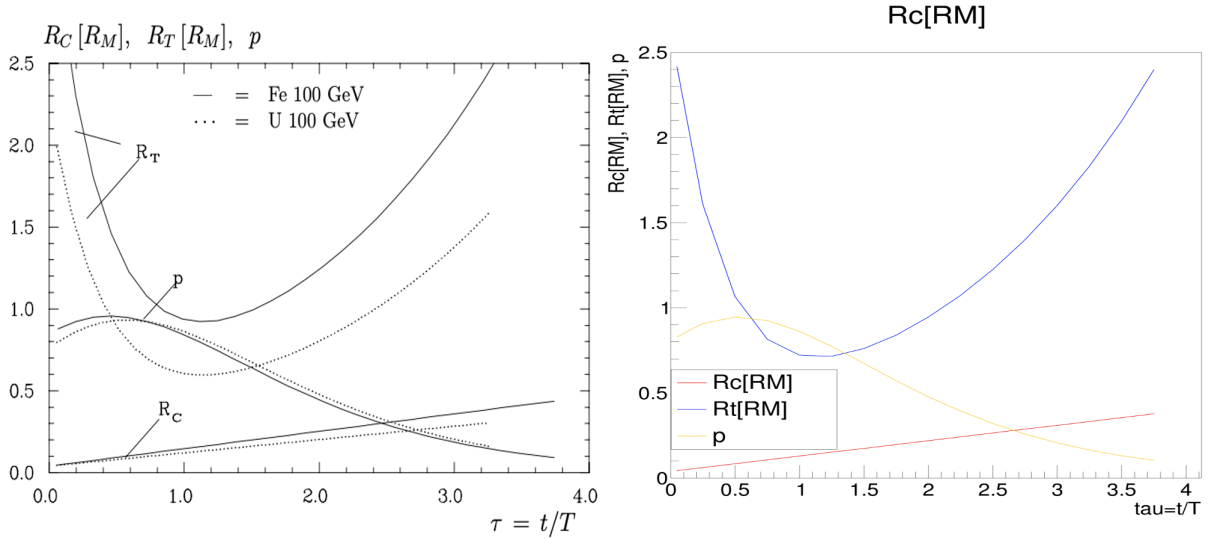
Figure 4.6: Dependency of radial shower parameters on the shower depth for a 100 GeV electron: for uranium and iron calorimeters on the left [37], for the MUonE PbWO4 calorimeter on the right.

in units of shower maximum ($\tau = t/T$) for different calorimeters: uranium and iron on the left and $PbWO_4$ on the right. For the radial profiles, the dependence on the material is apparent for the tail distribution.

For a given energy and material, the three parameters are modelled as function of the shower depth $\tau = t/T$ in this way:

$$
\begin{aligned}
R_C(\tau) &= z_1 + z_2\tau \\
R_T(\tau) &= k_1(e^{k_3(\tau - k_2)} + e^{k_4(\tau - k_2)}) \\
p(\tau) &= p_1 e^{\left(\frac{p_2 - \tau}{p_3} - e^{\left[\frac{p_2 - \tau}{p_3}\right]}\right)}
\end{aligned}
\tag{4.17}
$$

where $z_1, ..., p_3$ are constants or functions of $\ln E$ or Z, as given in Appendix.

In Fig.(4.7) the mean radial profiles and their fluctuations are shown for energies of 40 GeV in lead and 100 GeV in uranium. Parameterized simulations are compared with the GEANT full simulation in black, while in colors the corresponding plots are obtained for the MUonE ECAL.

The fluctuations of the radial profile are strictly related to the longitudinal ones: at a given depth t, the released energy $dE(t)$ is not always the same, it is itself subjected to fluctuations. Thus, the shower maximum T varies event-by-event and so does $\tau = t/T$

64
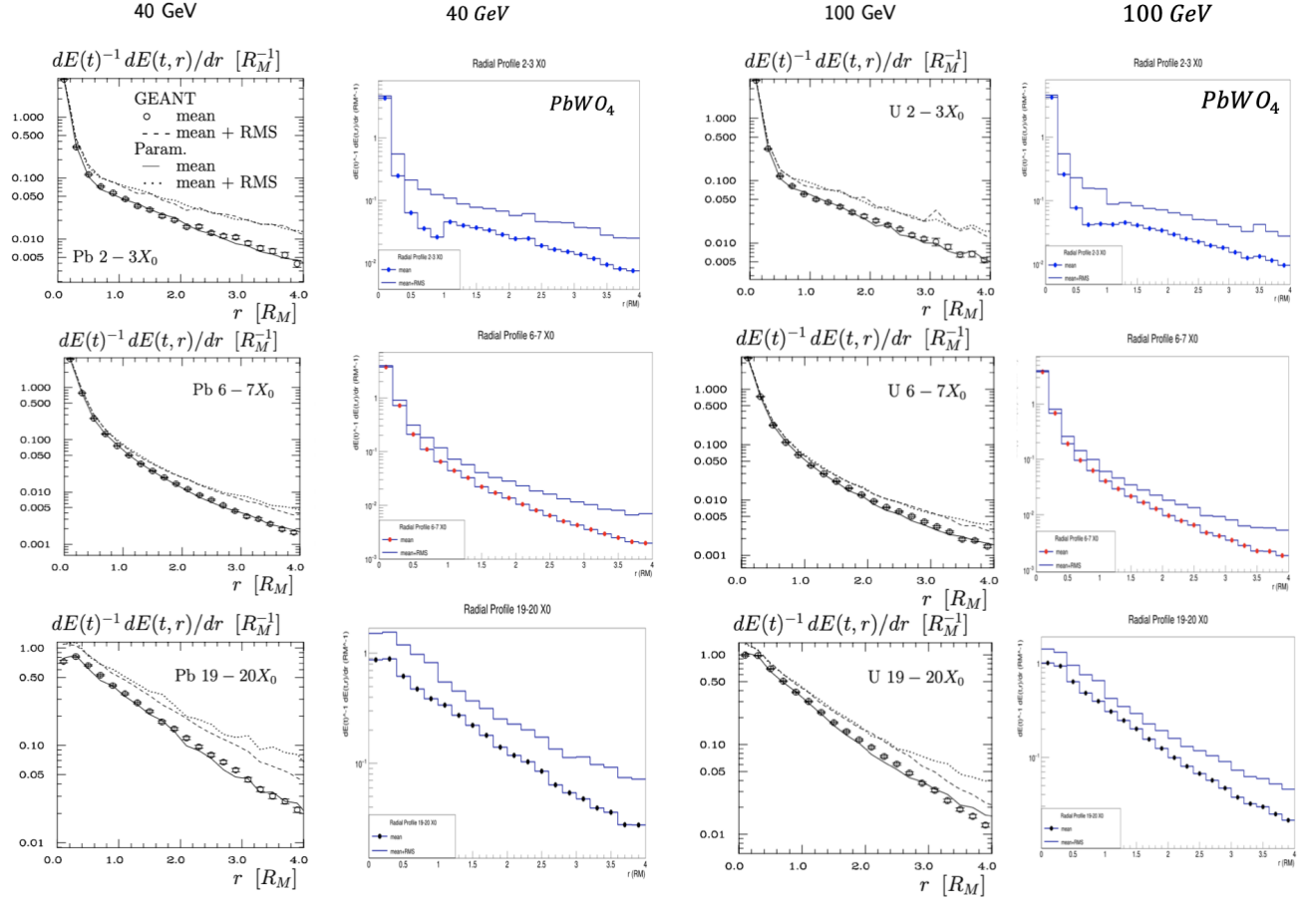
Figure 4.7: First and third columns show mean radial profiles and their fluctuations in lead (40 GeV) and uranium (100 GeV) [37]. In second and fourth obtained with the parametrized simulation for the MUonE calorimeter ($PbWO_4$).

at any given depth t. Therefore the radial energy profile changes at a given depth, as it depends on τ (Eq.4.17).

Having described all the parameters of the used shower model, the Monte Carlo event simulation proceeds as follows. Let's assume to divide the longitudinal profile in steps of $1X_0$. At each step t the deposited energy $\mathrm{d}E(t)$ can be evaluated through the integral in Eq. 4.15. This energy is divided into $N_s(t)$ energy spots which are distributed in the radial profile according to $f(r)$ and uniformly in t and ϕ. Each energy spot is given the same energy:

$$E_s(t) = \frac{\mathrm{d}E(t)}{N_s(t)} \tag{4.18}$$

The number of spots in the considered step $N_s(t)$ is evaluated starting from the total number of spots N_s all along the shower:

$$N_{spot} = 93 \ln(Z) E^{0.876}.$$ (4.19)

The position r of each energy spot is given by a Monte Carlo method, where Eq. 4.16 is integrated and inverted:

$$F(r) = \int_0^r \frac{2r'R^2}{(r'^2 + R^2)^2} dr' = \frac{r^2}{r^2 + R^2}$$

$$F^{-1}(u) = R\sqrt{\frac{u}{1-u}}.$$ (4.20)

Therefore, the generation of the random radius is done using the following expression:

$$r_i = \begin{cases} R_C \sqrt{\frac{v_i}{1-v_i}} & p < w_i \\ R_T \sqrt{\frac{v_i}{1-v_i}} & \text{else.} \end{cases}$$ (4.21)

where v_i and w_i are two normally distributed random numbers. Depending on the value of w_i, the point contributes to the *core* or to the *tail* region.

The number of spots in a longitudinal step is parametrized by a gamma function with parameters:

$$T_{Spot} = T(0.698 + 0.00212Z),$$
$$\alpha_{Spot} = \alpha(0.639 + 0.00334Z),$$ (4.22)

giving

$$N_s(t) = N_{Spot} \int_{t_{j-1}}^{t_j} \frac{(\beta_{Spot}t)^{\alpha_{Spot}-1} \beta_{Spot} e^{-\beta_{Spot}t}}{\Gamma(\alpha_{Spot})} dt$$ (4.23)

Additional correlation between the radial and longitudinal pdfs are introduced with the redefinition of the individual shower's center of gravity:

$$\langle t_i \rangle = \frac{\alpha_i}{\beta_i} = T_i \frac{\alpha_i}{\alpha_i - 1}.$$ (4.24)

To account for those, τ in Eq. 4.17 is replaced by τ_i:

$$\tau_i = \frac{t}{\langle t_i \rangle} \frac{e^{\langle \ln \alpha \rangle}}{e^{\langle \ln \alpha \rangle} - 1}.$$ (4.25)

Only the simulations using τ_i are able to predict the fluctuations observed with GEANT correctly.

To summarize, the steps of the algorithm are:

66

1. Segmentation of the longitudinal profile into slices of width $1X0$. For each one, the energy deposited $dE(t)$ is calculated with Eq. 4.15;

2. For each longitudinal interval, $N_s(t)$ energy spots are generated with a given energy $E_S(t)$;

3. Each spot is distributed in the radial profile according to $f(r)$ and uniformly in t and ϕ;

4. In the end, for every spot there are four variables $[E_s, t[X_0], r[R_M], \phi]$. The spatial coordinates are transformed into cartesian ones $[E_s, x, y, z]$ and the energy spot is set within the defined geometry of the calorimeter to study the energy deposition in each cell.

As an example, Fig.(4.8) shows a simulated event with an electron of 10 GeV impinging in the central cell of the MUonE calorimeter in $(x, y) = (0, 0)$.
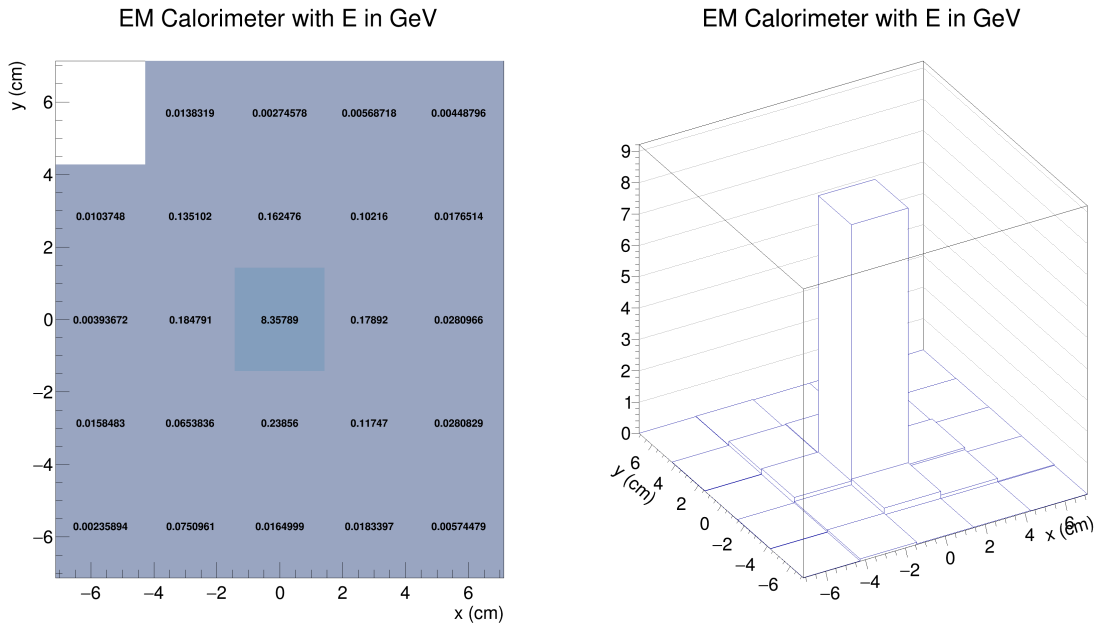

Figure 4.8: Example simulated event of a 10 GeV electron impinging on the centre of the ECAL. On the left the 2D grid of the deposited energies (in GeV) on all the cells; on the right the same event represented as a Lego-plot.

4.3 Energy distribution inside ECAL cells

After having developed the tool for the EM shower simulation, it is important to study the mean energy fraction released in each ECAL crystal. The analysis is focused on two main cases:

1. electron hitting the central region of the central cell (impact point: $(x, y) = (0, 0)$ on cell $N = 13$ in Fig.(3.9));

2. electron impinging on the ECAL in a random point generated according to the beam spot profile.

It is interesting to analyze the energy fraction deposited in:

- i) the cell with the maximum energy deposition (*seed* cell);

- ii) an array of 3×3 cells around the seed one.

The first case under study is when particles impact the calorimeter in the origin of the central cell. It represents the situation of maximum energy released inside a single cell, defining the dynamic range of the calorimeter. The test has been made with $E_e = 1.5, 10, 40, 75, 100, 150$ GeV. The fraction of energy is defined as $E_{frac} = \frac{E_{reco}}{E_{true}}$, where E_{reco} is the reconstructed energy and E_{true} is the true electron energy.

In Fig.(4.9), plots on the left show the distributions of the energy fraction inside one cell and on the right inside the 3×3 array. While for the first distributions the fit was made with a Gaussian, for the second ones a Crystal Ball function was chosen due to the presence of left tails, caused by shower fluctuations. Although clearly seen, these tails are not too large, thus the mean value of the histograms almost coincides with the mean value given by the fits. It results that the mean energy fraction released inside 3×3 cells averaged over the energies is 0.952.

Fig.(4.10) shows another validation plot for the algorithm, the energy containment as a function of the integration radius, in units of R_M. The plot on the left is the one from [37], while on the right is the result for the MUonE calorimeter. As it is expected, within a radius corresponding to the size of one cell, the contained energy is $\sim 82\%$, while for a radius corresponding to the 3×3 array, the containment is $\sim 95\%$, coherently with previous results.
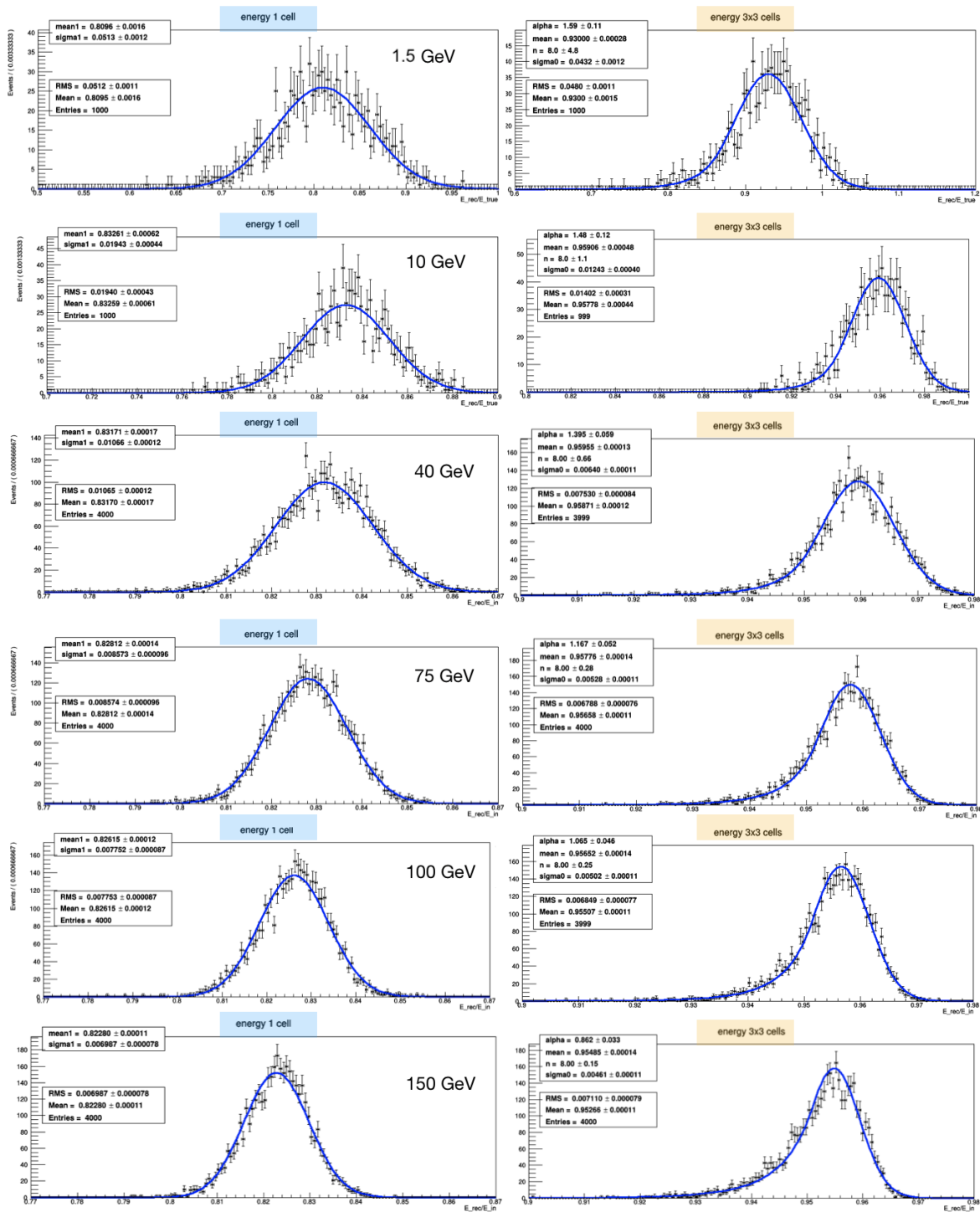
Figure 4.9: Reconstructed energy fraction inside the central cell and the 3×3 array when the impact point is in $(0, 0)$, for $E_{true} = 1.5, 10, 40, 75, 100, 150$ GeV. Top statistical boxes shows fit parameters (mean and sigma of the Gaussian on the left and of the Crystal Ball on the right) and bottom ones histograms mean and RMS.

69
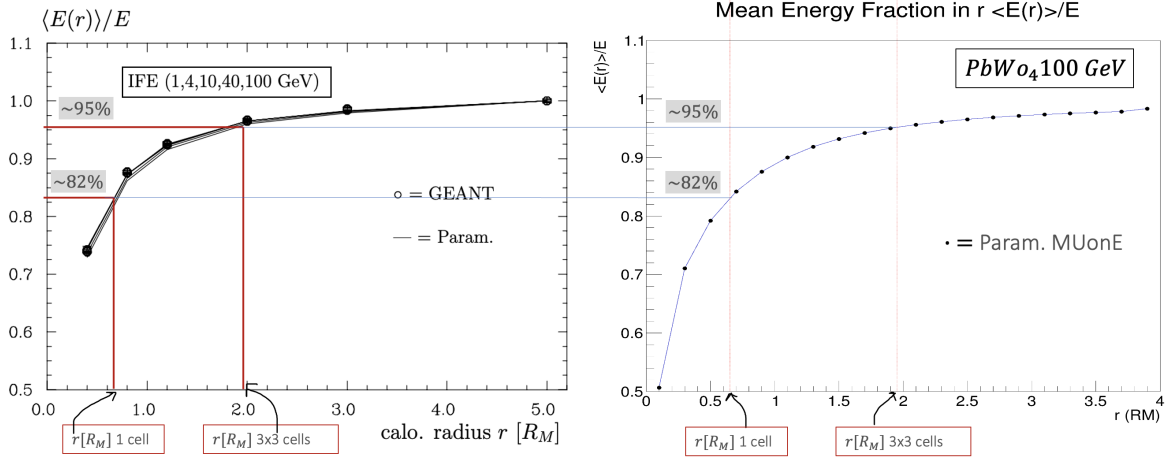
Figure 4.10: Mean energy containment $\langle E(r) \rangle / E$ as a function of the radius r in units of R_M. (Left) results from [37] of GEANT full simulation and the GFLASH parameterization; (Right) result for the MUonE calorimeter.

The second case is when the impact point has random coordinates generated according to the beam spot profile modelled as a 2D Gaussian centered at the origin $(x, y) = (0, 0)$ and with spread given by $\sigma_x = 2.6$ cm and $\sigma_y = 2.7$ cm. In Fig.(4.11) the distributions of the energy fractions in the single seed cell (on the left) and in the 3×3 array (on the right) have enhanced tails, in particular for the single crystal. This is due to the randomness of the impact point: if the particle impacts the cell near the edge, the fraction of energy inside it would be drastically reduced with respect to the case of central impact point. For this reason, both of the fits have been carried out with a Crystal Ball function. It results that the mean energy fraction released inside 3×3 cells averaged over the energies is 0.940.

The randomness of the impact point does not affect significantly the 3×3 reconstruction: the average mean value of the histogram is only $\sim 1\%$ lower with respect to the central impact; while for a seed cell, there is a reduction of $\sim 13\%$.
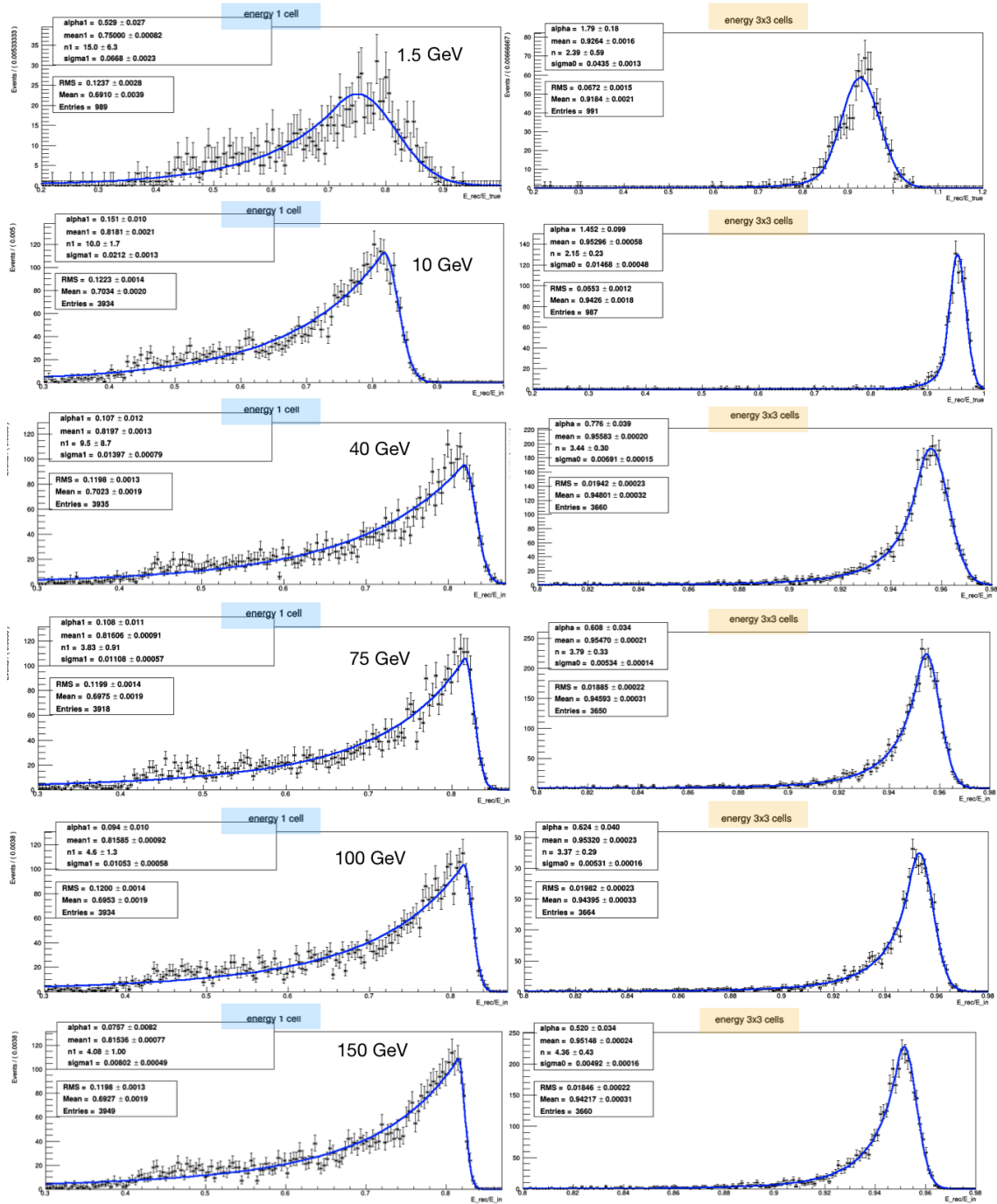
Figure 4.11: Reconstructed energy fraction inside the central seed cell and the 3×3 array around it for electrons with impact point corresponding to the beam spot profile, for $E_{true} = 1.5, 10, 40, 75, 100, 150$ GeV. Top statistical boxes show fit parameters (mean and sigma of the Gaussian on the left, while of the Crystal Ball on the right) and bottom ones mean and RMS of the histograms.

71
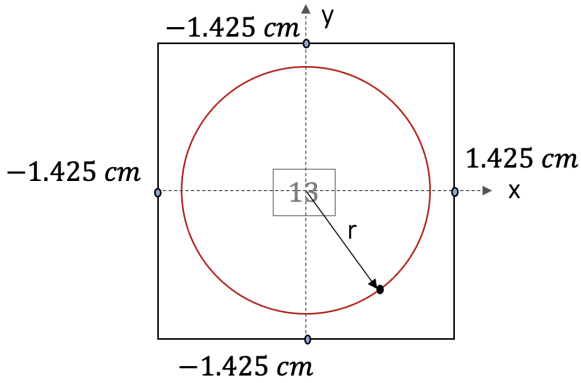
Figure 4.12: Example of a random impact point inside the central cell $N = 13$, used for the study on the dependence of the reconstructed energy fraction as a function of the impact point.
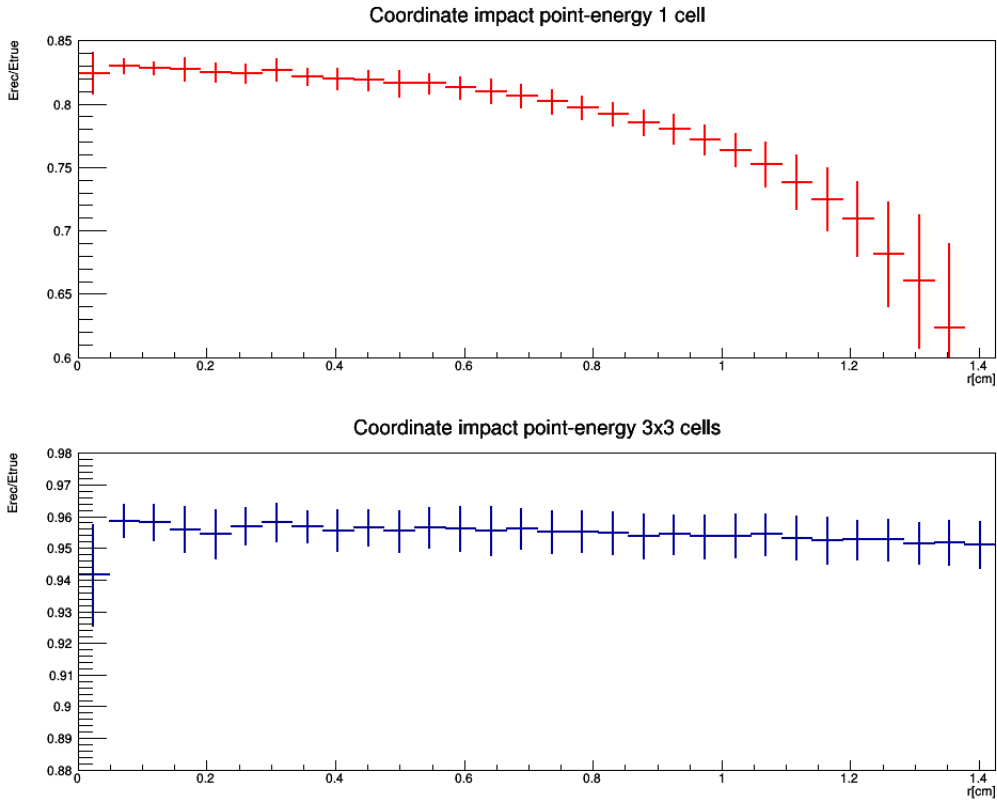
Figure 4.13: Average reconstructed energy fraction as a function of the distance of the impact point from the cell centre, for single cell (top) and the 3×3 array (bottom).

In order to study the dependence of the reconstructed energy on the impact point, let us consider the central crystal ($N = 13$) and particles impinging randomly inside it, as shown in Fig.(4.12). The reconstructed energy fraction E_{frac} as a function of the distance between the origin and the incidence point (r) is plotted in Fig.(4.13) both for

the single cell, in red, and for the 3×3 cells around it, in blue. As expected, the fraction in the single cell is strongly dependent on where the particle impacts, going from $\sim 82\%$ to $\sim 62\%$ at the edge; while it has a flat behavior considering 9 crystals.

Some events may impact the cells around the perimeter of the ECAL, as the ones not
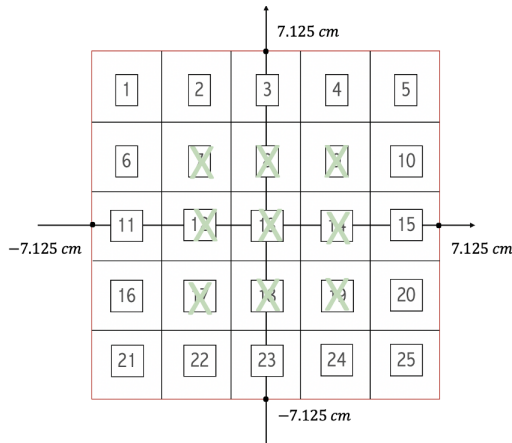
Figure 4.14: Picture of the calorimeter, the cells with a green cross are the ones for which the 3×3 array is totally included in the ECAL.

green crossed in Fig.(4.14). In this situation, the energy would not be reconstructed in the right way and this fact needs to be taken into account for the final analysis.

Fig.(4.15) shows the mean fractions of energy inside 3×3 arrays centered in each crystal.
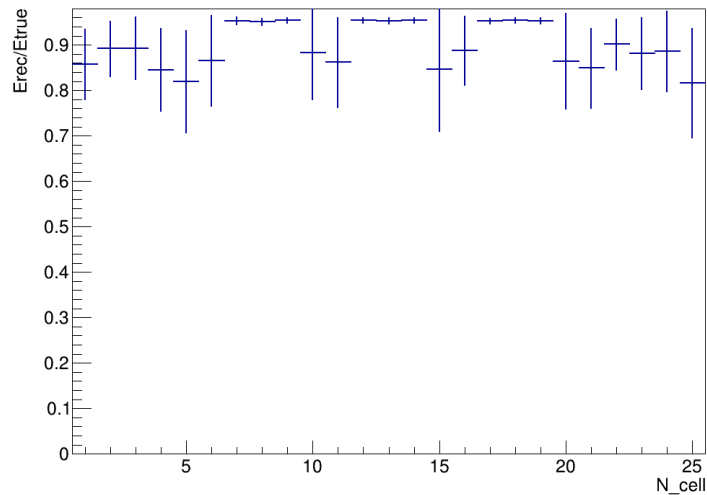
Figure 4.15: Mean fraction of energy inside 3×3 array for particles impinging in each cell of the calorimeter. The cell numbering corresponds to Fig.(4.14).

It is clear how stability persists only when the 9 crystals are all contained in the ECAL.

To sum up, in Fig.(4.16) the mean energy fraction and the RMS of the histograms respectively in the case of impact point $(0,0)$ and random point (x, y) are shown for the
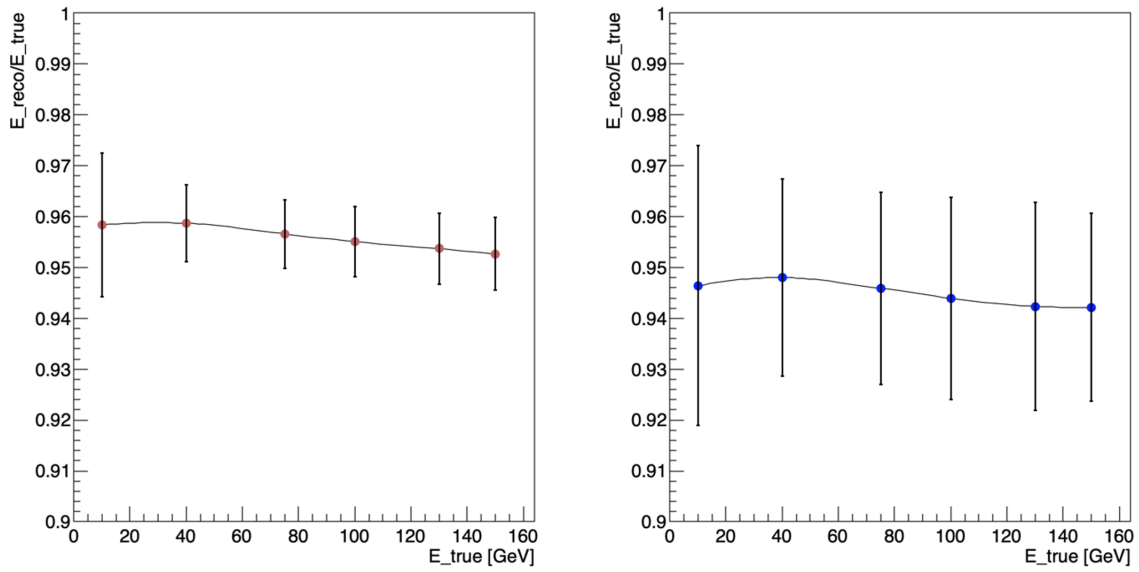
Figure 4.16: Mean fraction of energy inside 3×3 array for particles impinging in $(0, 0)$ on the left and in a random point on the right. The errors represent the RMS of the distribution.
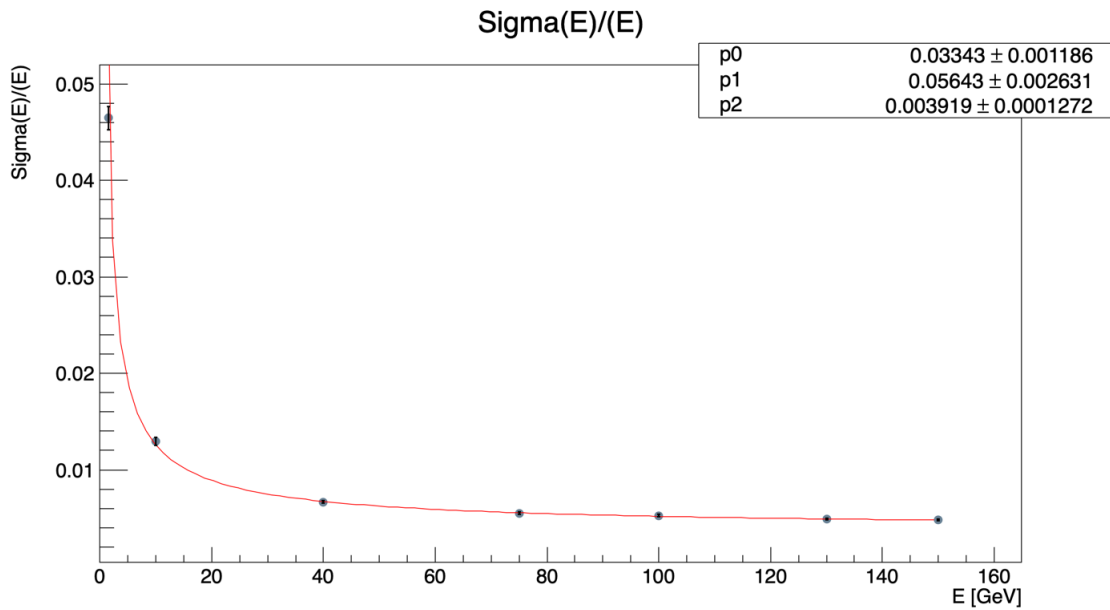
Figure 4.17: Calorimeter resolution as a function of E.

3×3 cell array as a function of the true energy. This plot demonstrates that the algorithm of reconstruction with nine cells is quite stable and the mean energy fraction released is

weakly dependent on the energy. It will be used for the final analysis of the thesis, but for future studies the correction of 5% on the reconstructed energy needs to be implemented. In Fig.(4.17) the energy resolution obtained for the 3×3 cell reconstruction algorithm is shown for the case of central impact. The points are fitted with the functional form:

$$\frac{\sigma(E)}{E} = \sqrt{\left(\frac{p_0}{\sqrt{E}}\right)^2 + \left(\frac{p_1}{E}\right)^2 + p_2^2} \qquad (4.26)$$

which gives p_0, p_1, p_2 parameters in Fig.(4.17). Due to the non-Gaussian tails, visible in the previous Fig.(4.9), the effective resolution is slightly worse than the plotted result. In the next chapter a selection is studied based on the expected energy resolution. To be conservative the RMS values have been used instead of the Crystal Ball core resolution.

Chapter 5

NLO events with the complete Fast Simulation

The simulation of the kinematical properties of the beam and the propagation of the events through the experimental setup help to figure out the picture of events expected in the Test Run 2021, while the simulation of the calorimeter response aims to understand its behavior and how it can be used in this context.

The two tools have been separately developed and need to be implemented in a single code in order to have a complete fast simulation of the Test Run 2021 setup. NLO events imply the possible presence of photons in the final state which will not be detected by the tracker, thus the ECAL may play an essential role. The fast simulation tool will help studying the identification of these radiative events.

5.1 Analysis

Chapter 4 shows how the reconstruction of an energy deposit can be effectively performed relying on a 3×3 matrix centered around the seed cell. However, in order to ensure the accurate reconstruction of the energy deposit, all the 9 matrix elements have to be contained in the calorimeter, as shown in Fig.(4.15). The condition of the full containment defines the fiducial surface for the impact points of the electrons. All the events which impinge on the ECAL in one of the cells at the borders (without the cross in Fig.(4.14)) will be excluded.

The area of the fiducial surface is 8.55×8.55 cm^2 (calorimeter core), appreciably smaller than the entire surface. Fig.(5.1) shows in black the events distribution as a function of the electron scattering angle, separately for both the targets. In green the same events requiring the electron inside the fiducial surface. The higher the electron scattering angle, the smaller the probability to be detected.
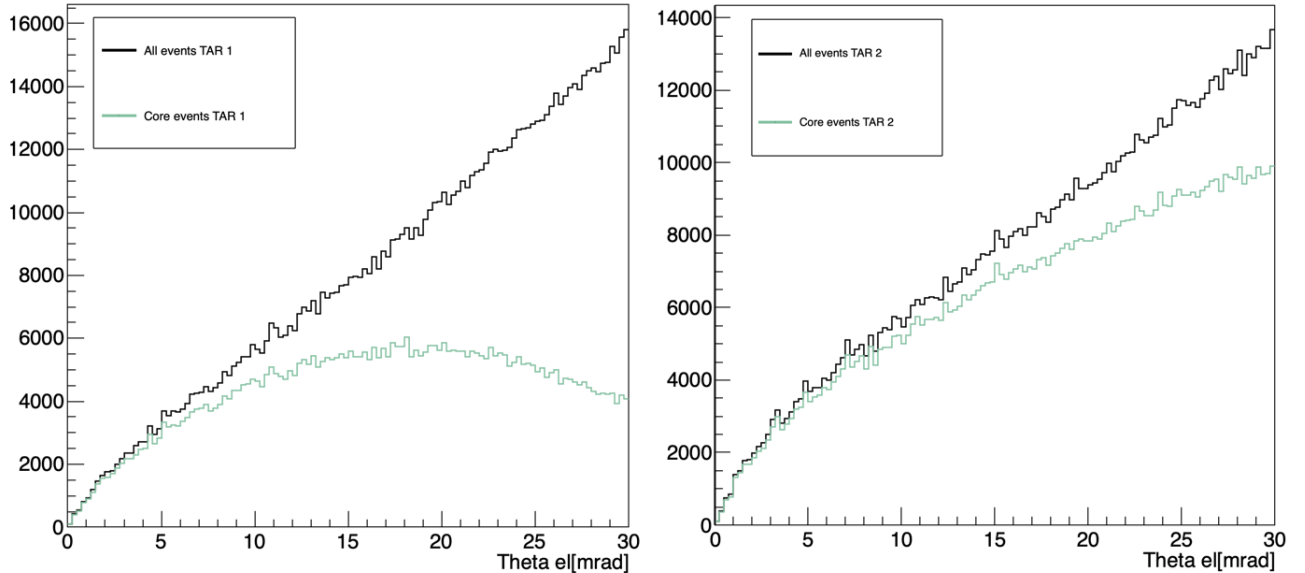
Figure 5.1: Scattering angle (mrad) of all the generated electrons in black and of the electrons which reach the fiducial volume of the calorimeter in green. On the left the events coming from Target 1 and on the right from Target 2.

In order to get the calorimeter acceptance flat, one needs to reduce the fiducial region of the beam such that all the generated events, within the foreseen scattering angular acceptance, effectively reach the calorimeter fiducial surface.

The efficiency is defined as $\epsilon = \frac{N_{core}}{N_{gen}}$ where N_{gen} is the number of generated events while N_{core} is the number of events with the scattered electron within the calorimeter core. Red histograms in Fig.(5.2) show the efficiency plots for electrons outgoing from Target 1 (top) and from Target 2 (bottom).

The fiducial cut on the beam is imposed requiring the impact point of the incoming muon on the target $r_\mu < r_{\mu\,cut}$. In addition, in order to increase the efficiency at large scattering angles, a threshold is applied to the reconstructed cluster energy $E_{3\times3}$.

The chosen combination is:

$$r_\mu < 1.7 \text{ cm}, \quad E_{3\times3} > 1 \text{ GeV}. \tag{5.1}$$

As it is shown in the right plots of Fig.(5.2), the selection cuts act remarkably well for electrons in the small angular region for both Target 1 and Target 2. The $\theta_e < 5$ mrad region is crucial, as the μ/e discrimination there is essential. Because of the geometrical acceptance the constant efficiency, over all the θ_e range, can be achieved only for collisions
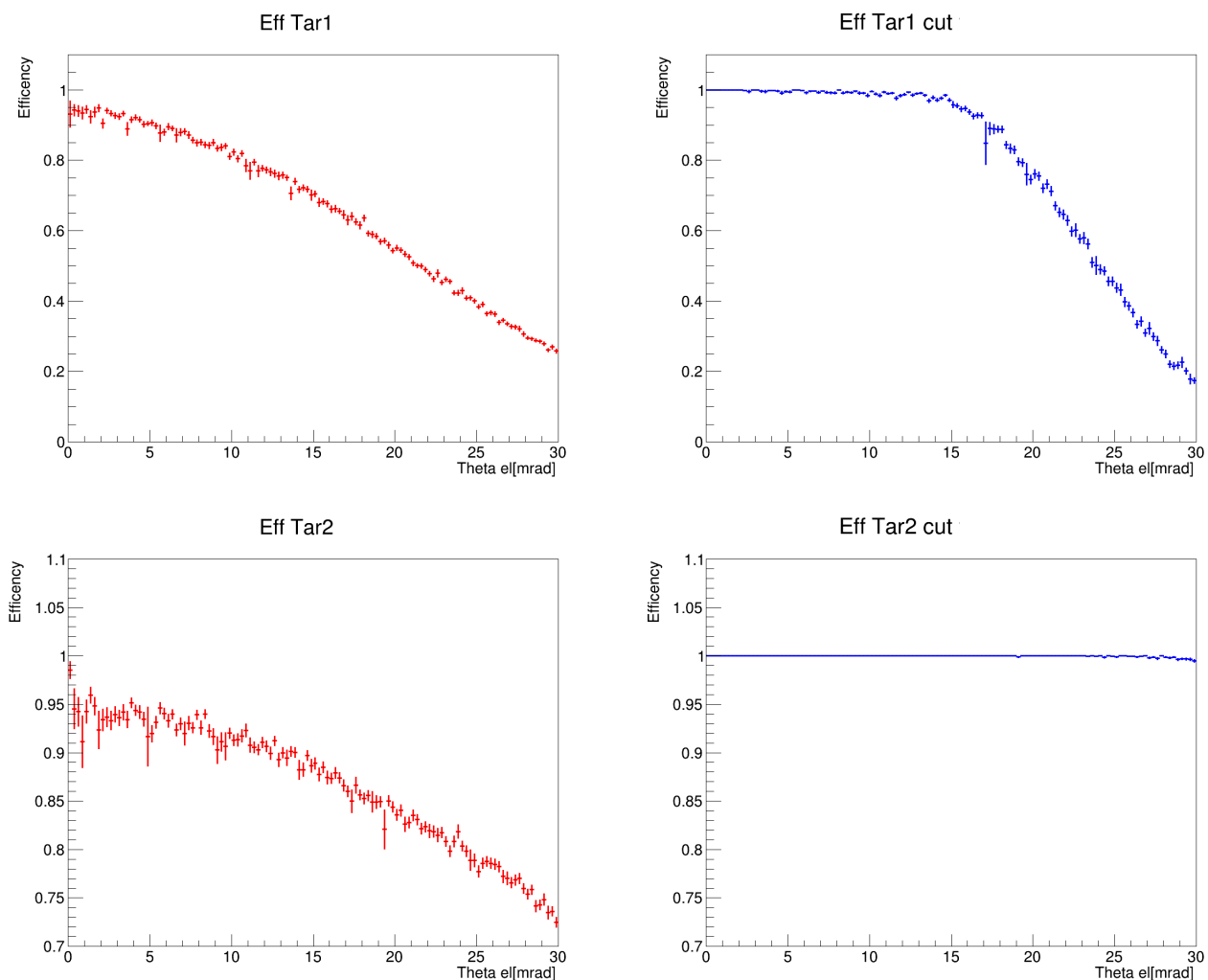
Figure 5.2: Calorimeter core acceptance as a function of the electron scattering angle. In red without any cut; in blue with the fiducial cut imposed. Plots on the top correspond to events when collisions occurred at Target 1, plots on the bottom to events when collisions occurred at Target 2.

occurring at Target 2. For this reason the analysis has been restricted to events generated at Target 2, closer to the calorimeter. The preselection cut on the electron scattering angle is from now on set to 35 mrad.

There are two useful plots which help in the study of a first event classification:

1. The (θ_e, θ_μ) in Fig.(5.3), where θ_i is the generation angle of the lepton;

78
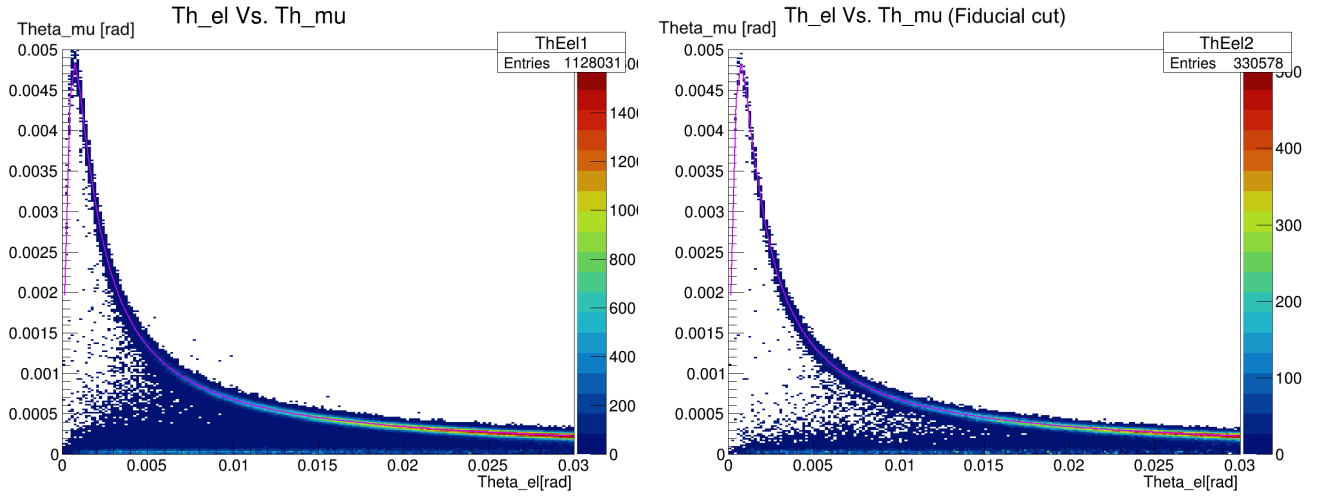
Figure 5.3: Correlation between the muon and electron scattering angles. The superimposed violet line represents the expected correlation for perfectly elastic events.
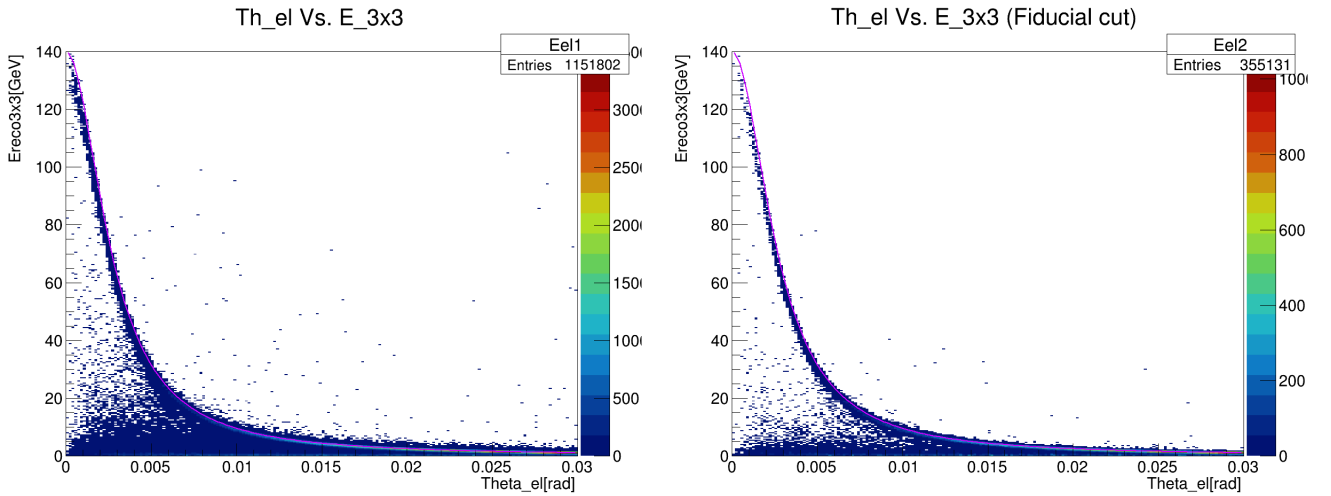
Figure 5.4: Correlation between the reconstructed calorimeter energy $E_{3\times3}$ and the electron scattering angle. The superimposed violet line represents the expected correlation from perfectly elastic events.

2. The $(\theta_e, E_{3\times3})$ in Fig.(5.4), where $E_{3\times3}$ is the reconstructed energy.

Avoiding the correction of 5% on the reconstructed energy, the points on the $(\theta_e, E_{3\times3})$ are slightly displaced with respect to the violet elastic curve. For future analysis this

79

correction should be taken into account.

Left plots in Fig.(5.3) and Fig.(5.4) are shown without any cut, while right plots have the fiducial cut $r_\mu < 1.7$ cm applied. The fiducial cut starts to thin out some of the events far from the violet elastic curves (given by Eq.2.19 and Eq.2.21), even if not sufficiently. In this way almost half of the TR2021 events are thrown away, nevertheless it is important to study the tracking and ECAL combination in the best possible situation, with the nearest station to the calorimeter, to establish the possible usage of the ECAL in the event identification. For the other stations and different applications, more analysis are needed, also taking into account that in the experiment the ECAL will be bigger.

The most useful calorimeter information which will be used for the next analysis are:

- The reconstructed energy in the 3×3 array $E_{3\times3}$;

- The centroid of the EM shower $\vec{r}_C$, estimating the impact position of the showering particle.

5.1.1   Effect of the cut on the $E_{3\times3}$ reconstructed energy

Using the calorimeter it is possible to select events with a $E_{3\times3}$ reconstructed energy greater than 1 GeV. As already seen, this allows to equalize the efficiency curve. Moreover it reduces the high θ_e events thinning out the band at low muon angle in (θ_e, θ_μ) plot, as shown in Fig.(5.5). Those ones are not interesting for the final analysis of the experiment as strongly affected by experimental perturbations and do not give important information for the running of the coupling. Among them there are electrons that, radiating soft photons, scatter at an angle smaller than the predicted elastic one, populating the low θ_μ region. In addition there is the contribution from feedthrough of low energy electrons undergoing large multiple scattering deviations from higher scattering angles. Using the MC truth, it is possible to study some of the variables of the radiated photons as the energy E_γ, the emitted angle θ_γ, the angular distance with the electron $\Delta\theta_{e-\gamma}$ and the distance of their impact points on the ECAL face $\Delta r_{e-\gamma}$. Fig.(5.6) shows in blue the photon distributions in the events passing the fiducial cut $r_\mu < 1.7$ cm, while in red the distributions for events cut off by the $E_{3\times3} > 1$ GeV threshold. Soft photons at large angle are mostly affected by this energy cut and the majority of those impact the calorimeter at a distance from one to several centimeters form the electrons.

5.1.2   Second cut: energy fraction

The first cut is not enough to have a clean sample of elastic events. The second method adopted is based on the mean energy fraction expected for an elastic event E_{reco}/E_{el}^{th}, where E_{el}^{th} is the predicted energy from Eq.2.21 at the corresponding scattering angle θ_e, known event-by-event.

Chapter 4 describes how the simulation of EM showers enables to study the mean fraction
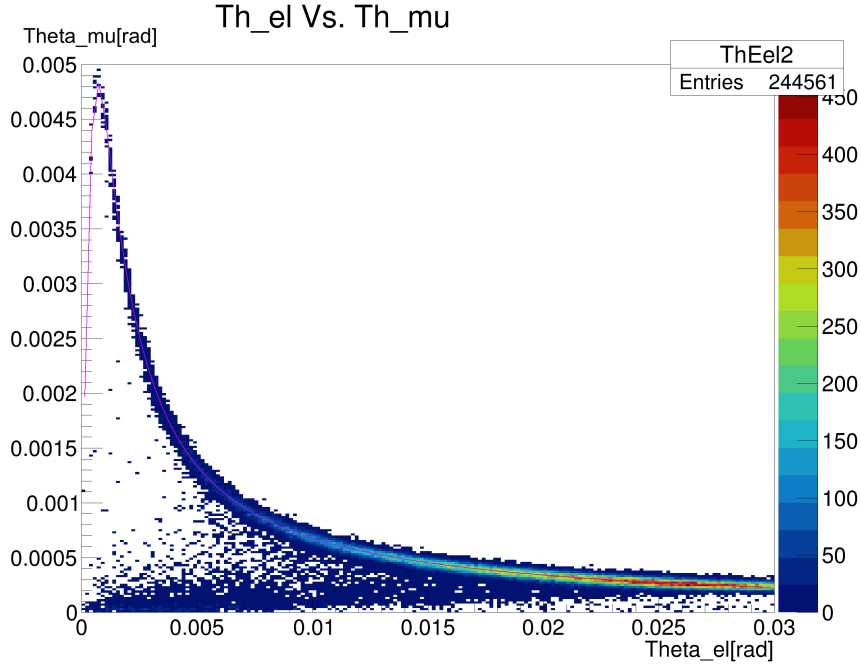
Figure 5.5: Correlation between the muon and electron scattering angles for Target 2 events, after the application of the fiducial cut on the distance of the beam muon from the axis and a cut on the reconstructed electron energy $E_{3\times3} > 1$ GeV. The superimposed violet line represents the expected correlation from perfectly elastic events.

of energy released in a 3×3 array for a given energy E_{true}. When this algorithm can be applied, the reconstructed energy fraction is stable, not depending on the impact point of the electron (bottom plots in Fig.(4.13)). The only dependence is on the energy of the impinging particle, shown in Fig.(4.16), which is quite weak but need to be taken into account.

Starting from this study, it is possible to define the variable:

$$\mathrm{D}E(\theta_e) = \frac{E_{3\times3}^{meas}}{E_{el}^{th}(\theta_e)} - 0.952 \tag{5.2}$$

where 0.952 is the simulated mean energy fraction averaged on different impact energies $\left\langle \frac{E_{3\times3}}{E_{true}} \right\rangle$. If the event is elastic, $\frac{E_{3\times3}^{meas}}{E_{el}^{th}(\theta_e)}$ should be compatible with the average, within resolution effects. If not, the true energy of the event does not correspond within the limits to the predicted elastic one and the event is likely to be a radiative event. The cut on $\mathrm{D}E(\theta_e)$ is defined according to the expected energy resolution, discussed in the previous chapter. To minimise the fraction of elastic events that could be rejected due to extreme shower fluctuations, which are observed in the tails, the cut has been conservatively taken at four times the RMS of the resolution function. Below an energy of

81
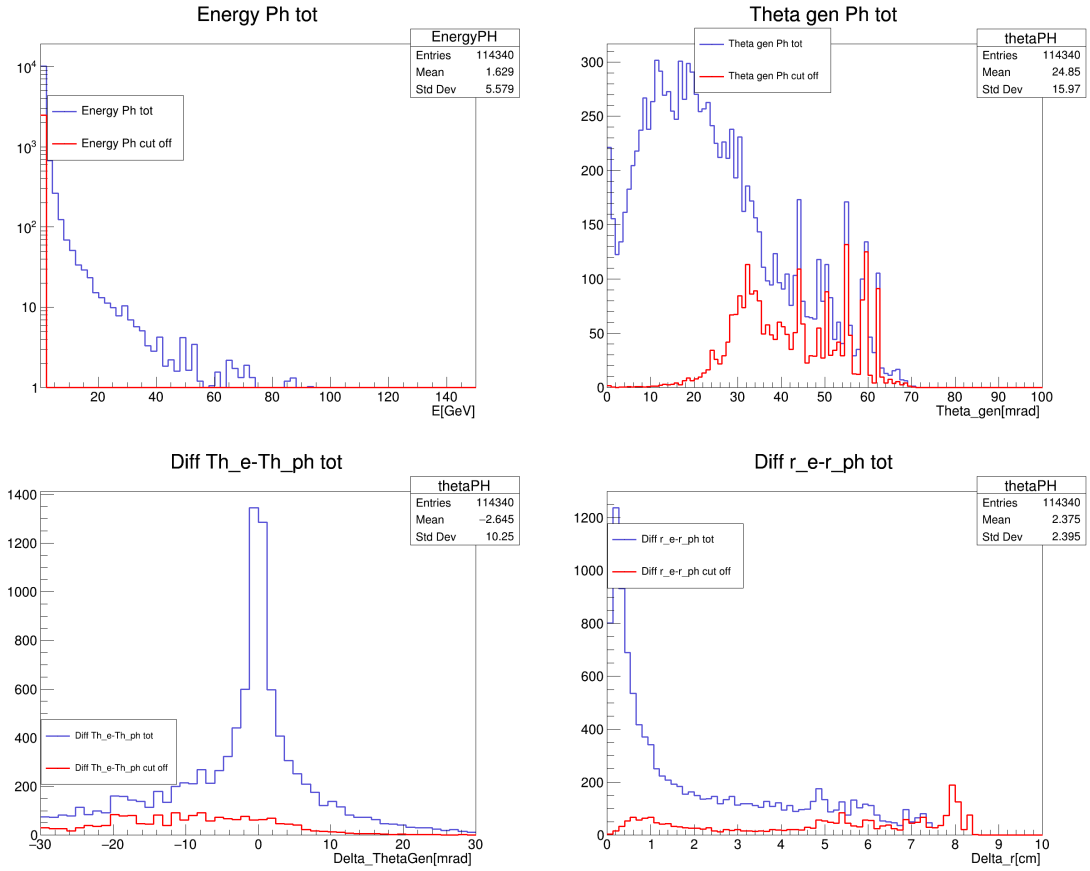
Figure 5.6: MC truth distributions of photon energy and generation angle on top and distance in angle and in cm from the electron on bottom. Blue histograms represent the photon distributions in events passing the fiducial cut $r_\mu < 1.7$ cm, while the red ones correspond to the events cut off by the condition $E_{3\times3} > 1$ GeV.

5 GeV this method would not be effective in terms of good classification, hence will not be applied.

Fig(5.7) and Fig(5.8) show the 2D plots with the additional application of the $\mathrm{D}E(\theta_e)$ cut. It is clear how this latter is effective in terms of radiative events rejection, the ones which have an energy far from the one predicted by the elastic curve are discarded. Those represent electrons which have an angle smaller than what is expected because of radiation.

MC truth distributions are shown in Fig.(5.9) where discarded photons are shown in red after the two subsequent cuts. It is evident how this second cut works on all type of photons, from high to low energy with small and large emission angle θ_γ. The combination of the two cuts allows to reject almost all the events with photons which impact
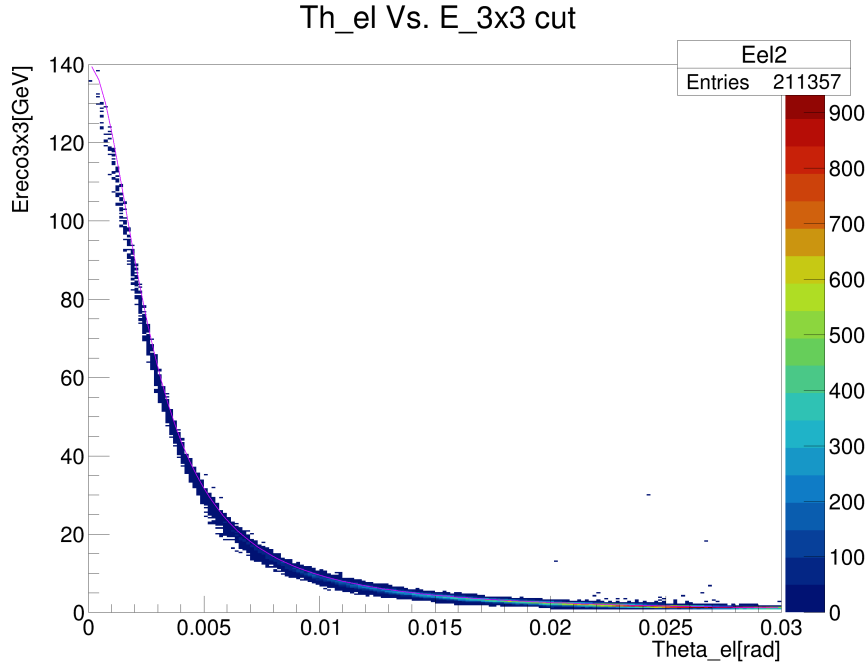
Figure 5.7: Correlation between the reconstructed calorimeter energy $E_{3\times3}$ and the electron scattering angle with the cuts on 1 GeV and on $\mathrm{D}E(\theta_e)$. The superimposed violet line represents the expected correlation from perfectly elastic events.

the calorimeter at a distance $d > 5$ cm from the electron, corresponding to large θ_γ.

5.1.3   Third cut: shower centroid

A useful variable which can be constructed from the shower information is the centroid. It is the particle impact position estimated by the ECAL and based on the distribution of energy within the calorimeter cells. The useful definition for MUonE calorimeter is taken from [38]:

$$x = \frac{\sum_i w_i x_i}{\sum_i w_i}, \quad w_i = \max\left\{0, \left[W_0 + \ln\left(\frac{E_i}{E_T}\right)\right]\right\}, \tag{5.3}$$

where i stands for the index of the crystal considered inside the 3×3 array around the seed cell, E_i the deposited energy inside it, x_i the one dimensional coordinate of its center and E_T is the total energy $E_{3\times3}$ inside the cluster, while $W_0 = 4.0$ is an adimensional parameter. The centroid coordinates (x_C, y_C) are separately evaluated with Eq.5.3.

Without any bias, it is expected that the differences

$$\Delta X = x_C - x_{track}, \quad \Delta Y = y_C - y_{track} \tag{5.4}$$

83
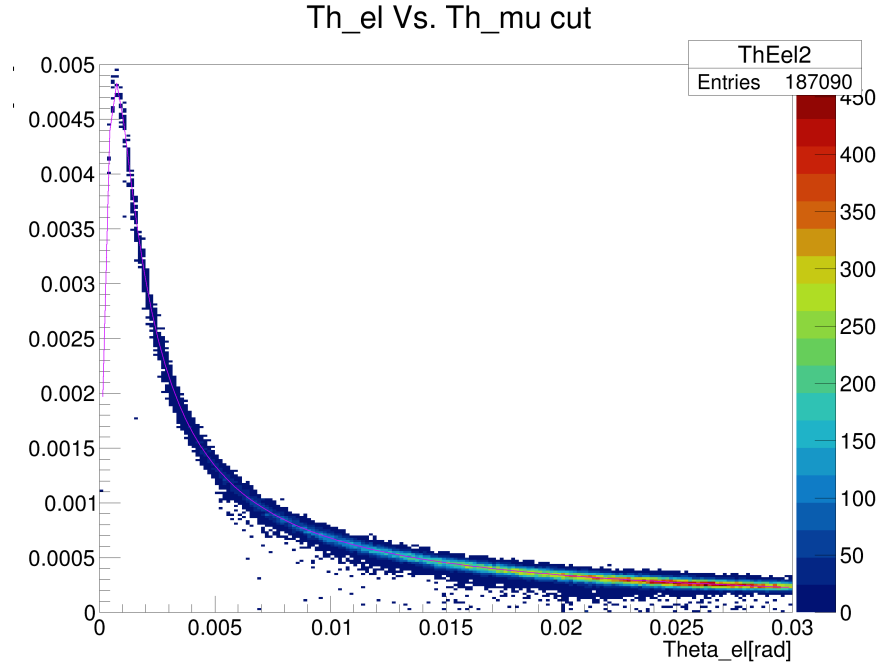
Figure 5.8: Correlation between the muon and electron scattering angles with the cuts on 1 GeV and on $DE(\theta_e)$. The superimposed violet line represents the expected correlation from perfectly elastic events.

between the centroid coordinates and the impact point of the extrapolated track propagated from the production vertex through the detector material, (x_{track}, y_{track}), are centered in zero. The width of these distributions represents the position resolution of the calorimeter respectively on the x and y coordinates. The resolution study can be done simulating monochromatic electrons with different energies, one example is shown in Fig.(5.10) for $E_e = 50$ GeV. Given the centroid position, the distance between this and the extrapolated track is defined as

$$\vec{R} = \vec{r}_C - \vec{r}_{track} \tag{5.5}$$

and its resolution results in:

$$\delta R = \sqrt{\delta x^2 + \delta y^2}. \tag{5.6}$$

The dependence of the resolution δR on the energy of the impinging particle is shown in Fig.(5.11). An empirical fit has been done with the form:

$$\delta R(E) = \sqrt{\left(\frac{p_0}{\sqrt{E}}\right)^2 + p_1^2,} \tag{5.7}$$
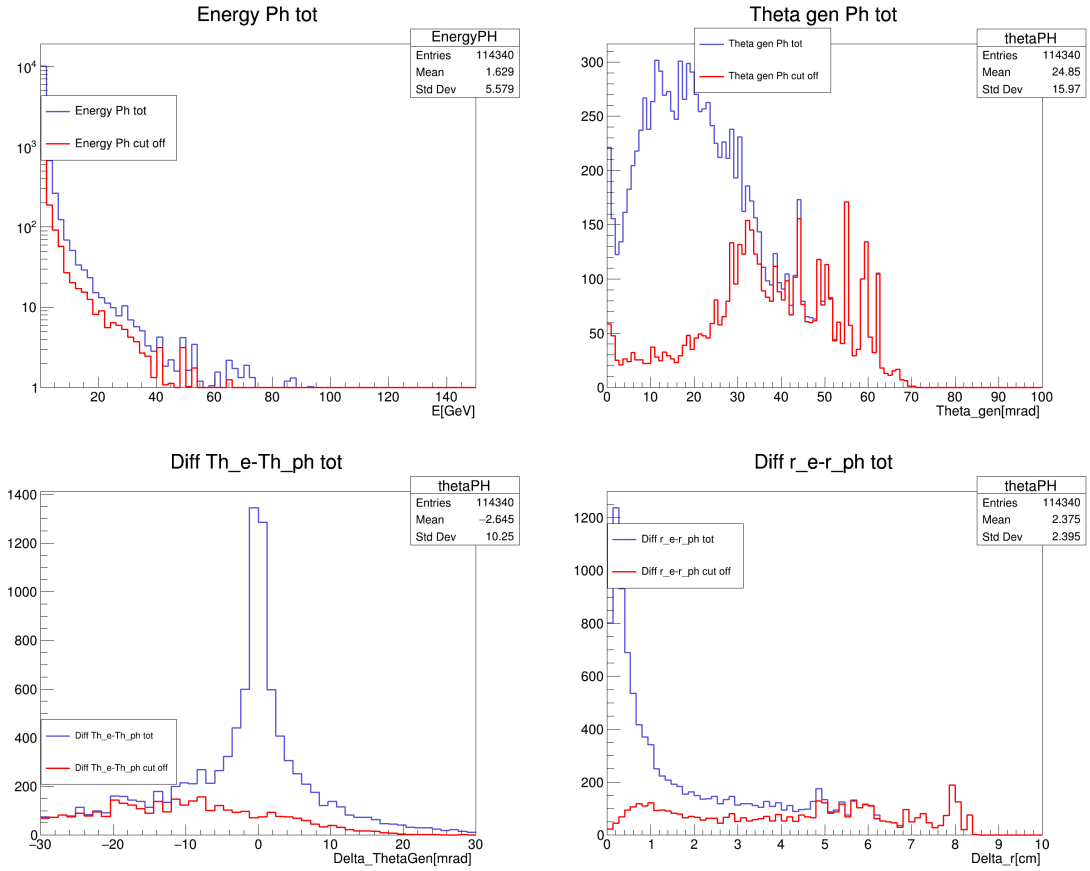
Figure 5.9: MC truth distributions of photon energy and generation angle on top and distance in angle and in cm from the electron on bottom. Blue histograms represent the photon distributions in events passing the fiducial cut $r_{mu} < 1.7$ cm, while the red ones correspond to the events cut off by the conditions $E_{3\times3} > 1$ GeV and the D$E(\theta_E)$ cut.

where fit parameters p_0 and p_1 are given in Fig.(5.11). The presence of a photon, contributing with its own shower, could displace the centroid from the electron impact point. The cut is imposed on the module of $\vec{R}$, discarding events with R larger than $4\,\delta R(E)$, where $\delta R(E)$ is given by Eq.5.7).

Fig.(5.12) and Fig.(5.13) show the 2D plots with the addition of the cut on $|\vec{R}|$. In the $(\theta_e, E_{3\times3})$ plot, the centroid cut helps in cleaning events at large electron angles which stand above the elastic curve, corresponding at small θ_μ events in the (θ_e, θ_μ) plane. Looking at Fig.(5.14) those are mostly hard photons events at small θ_γ, as a matter of fact the E_γ curve is now almost completely saturated at high energies. It also increases the number of discarded $e - \gamma$ pairs impacting the ECAL at small relative distances. The centroid method is effective when photon energy is high enough to shift significantly the
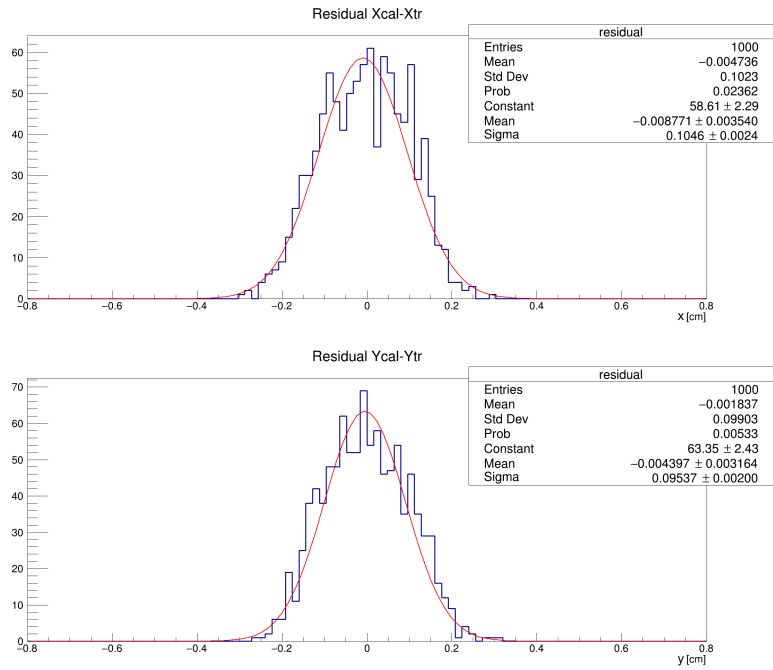
Figure 5.10: Difference between centroid coordinates and real impact point for 50 GeV electrons.
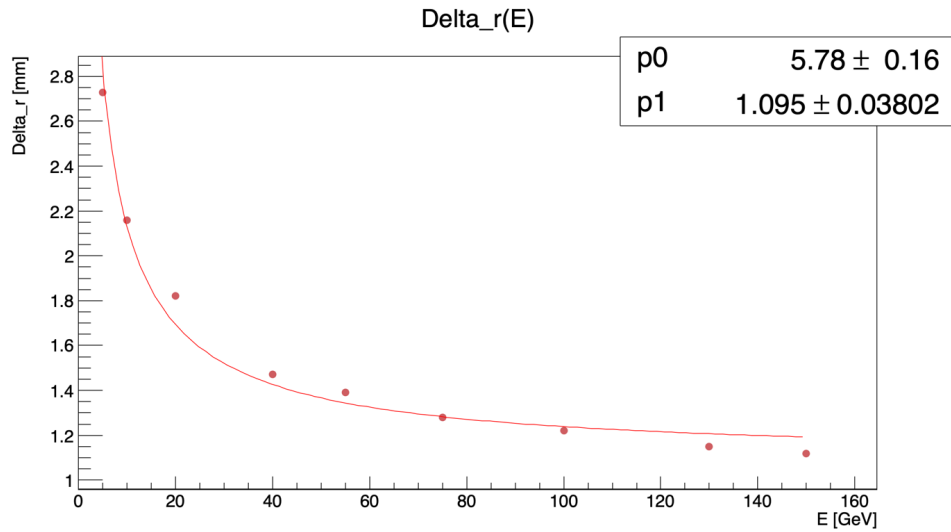
Figure 5.11: Resolution of the position determined by the ECAL shower centroid as a function of the particle energy.
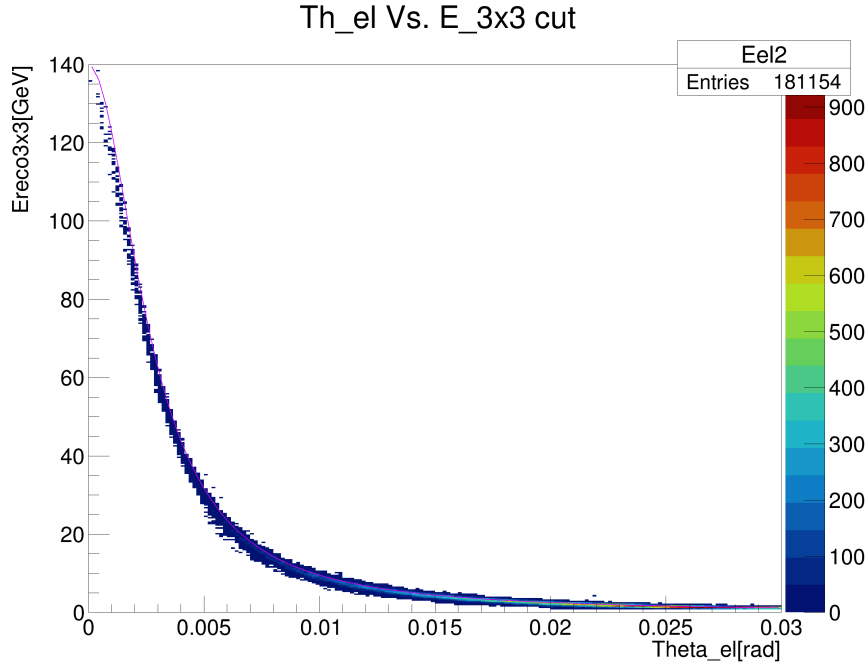
Figure 5.12: Correlation between the reconstructed calorimeter energy $E_{3\times3}$ and the electron scattering angle with the 1 GeV, $DE(\theta_e)$ and $|\vec{R}|$ cuts. The superimposed violet line represents the expected correlation from perfectly elastic events.

shower centroid from the electron impact point. Some of these events include the case where the photon is more energetic than the electron, thus the centroid of the shower is nearer to the photon impact position than to the electron one.

5.2   Final results

The three selection cuts help in cleaning up the 2D kinematical plots, as evident in Fig.(5.12) and (5.13).
Fig.(5.15) shows MC truth distributions for the outgoing electron and muon, obtained for the events after the full selection, including the fiducial cut on the incoming muon and the calorimeter cuts. The plots show the true particle angles and energies at the production vertex for all the events and after the full selection. The LO prediction for purely elastic events is also shown. It is interesting to notice that the application of the selection criteria moves the event distributions towards the LO ones, in particular the electron angle. Here it is evident that the muon scattering angle is a robust observable even in radiative events, as mentioned in Chapter 2; as a matter of fact the NLO distributions after the selection cuts mostly overlap with the LO ones. The calorimetric
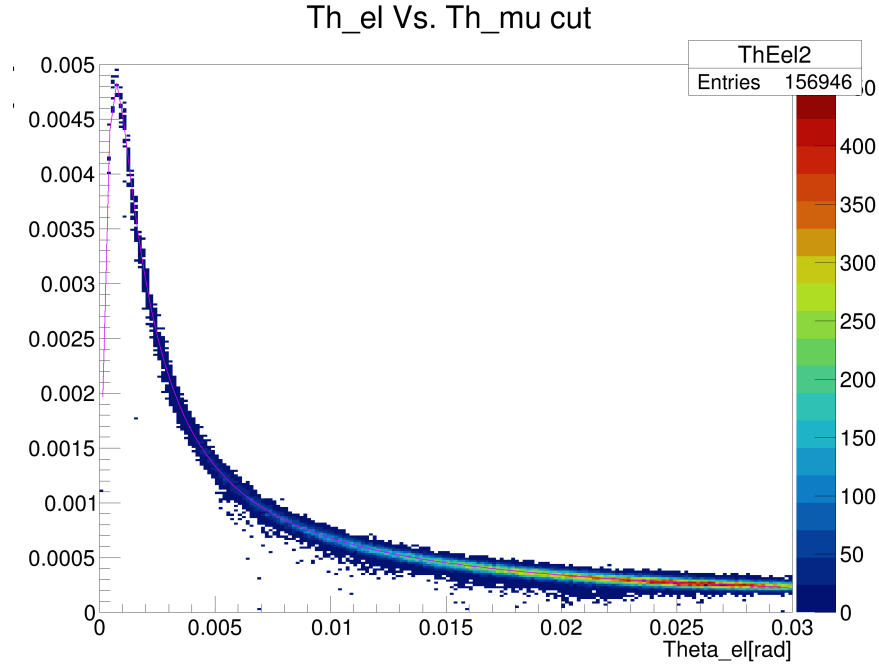
Figure 5.13: Correlation between the muon and electron scattering angles with the 1 GeV, $DE(\theta_e)$ and $|\vec{R}|$ cuts. The superimposed violet line represents the expected correlation from perfectly elastic events.

selection cuts mostly muons with low scattering angle, as it is clear from Fig.(5.15). Fig.(5.16) shows the individual effect of each selection cut applied in sequence. In Fig.(5.17) MC truth variables are shown for the remaining photons after the calorimetric selection. The majority of them are soft photons with impact point in the ECAL at a distance $d < 3$ cm from the electron, meaning that they are basically collinear with the electron and will be merged in the same energy cluster.

The selection discussed here is mainly based on the ECAL and appears to be effective in discarding radiative events. Additional criteria can be applied on the remaining events with an analysis based on the tracker and kinematical variables as the polar angles, acoplanarity and the χ^2 of the tracks.
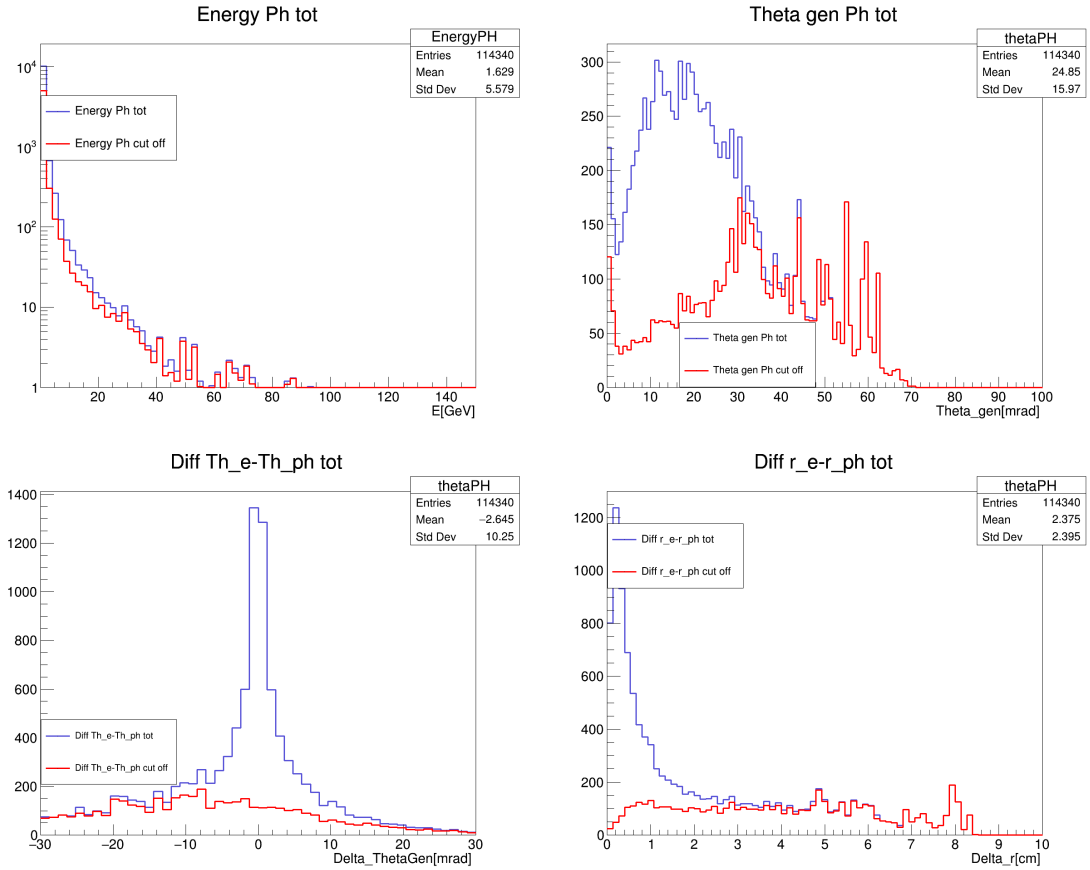
Figure 5.14: MC truth distributions of photon energy and generation angle on top and distance in angle and in cm from the electron on bottom. Blue histograms represent the photon distributions in events passing the fiducial cut $r_\mu < 1.7$ cm, while the red ones correspond to the events cut off by the full set of conditions: $E_{3\times3} > 1$ GeV, the D$E(\theta_E)$ cut and the cut on $|\vec{R}|$.
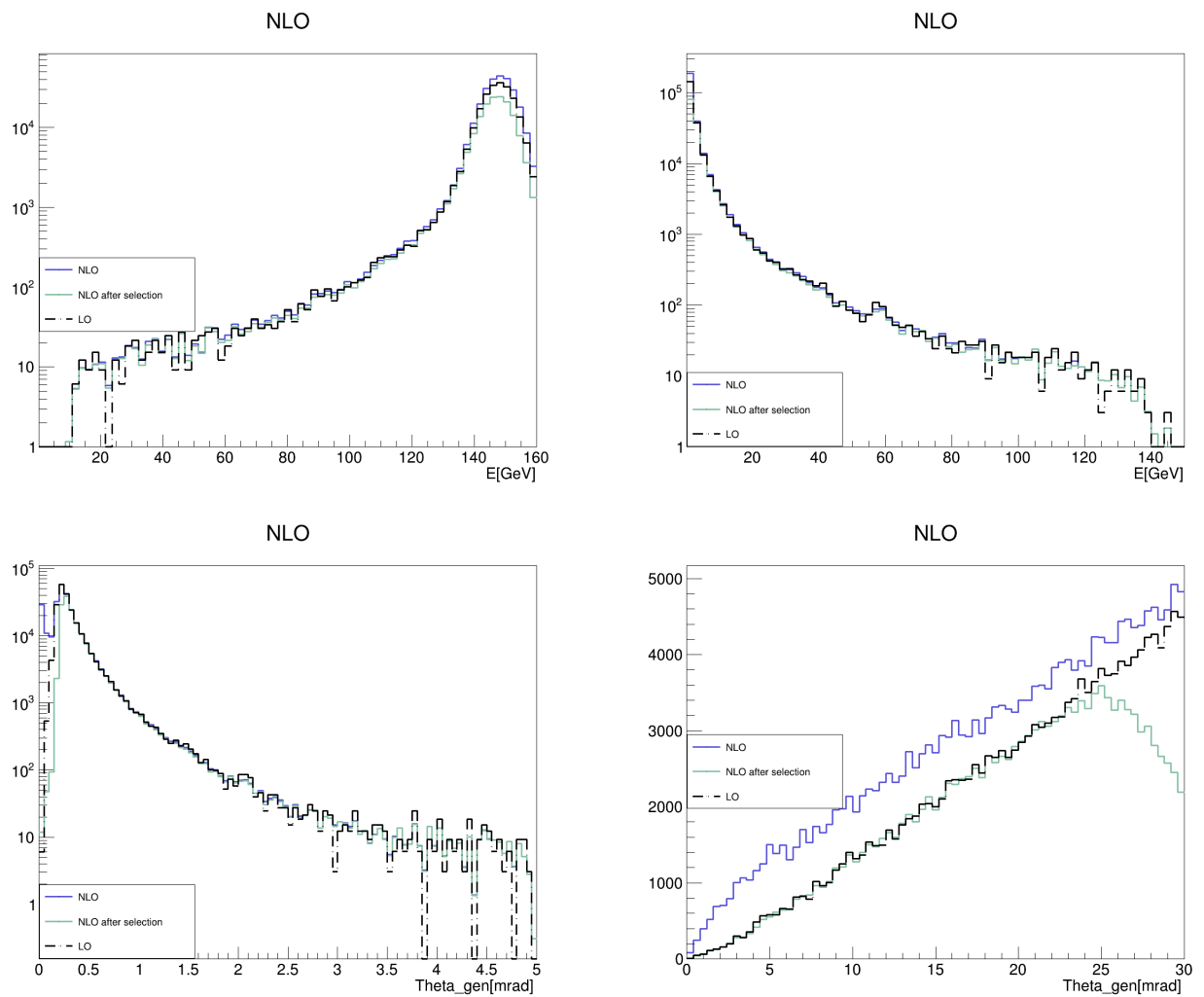
Figure 5.15: MC truth distributions of muons (left, in red) and electrons (right, in blue) energy and scattering angle before the calorimetric selection. The effect of the selection is shown by the green histograms. The black histograms show the LO prediction.
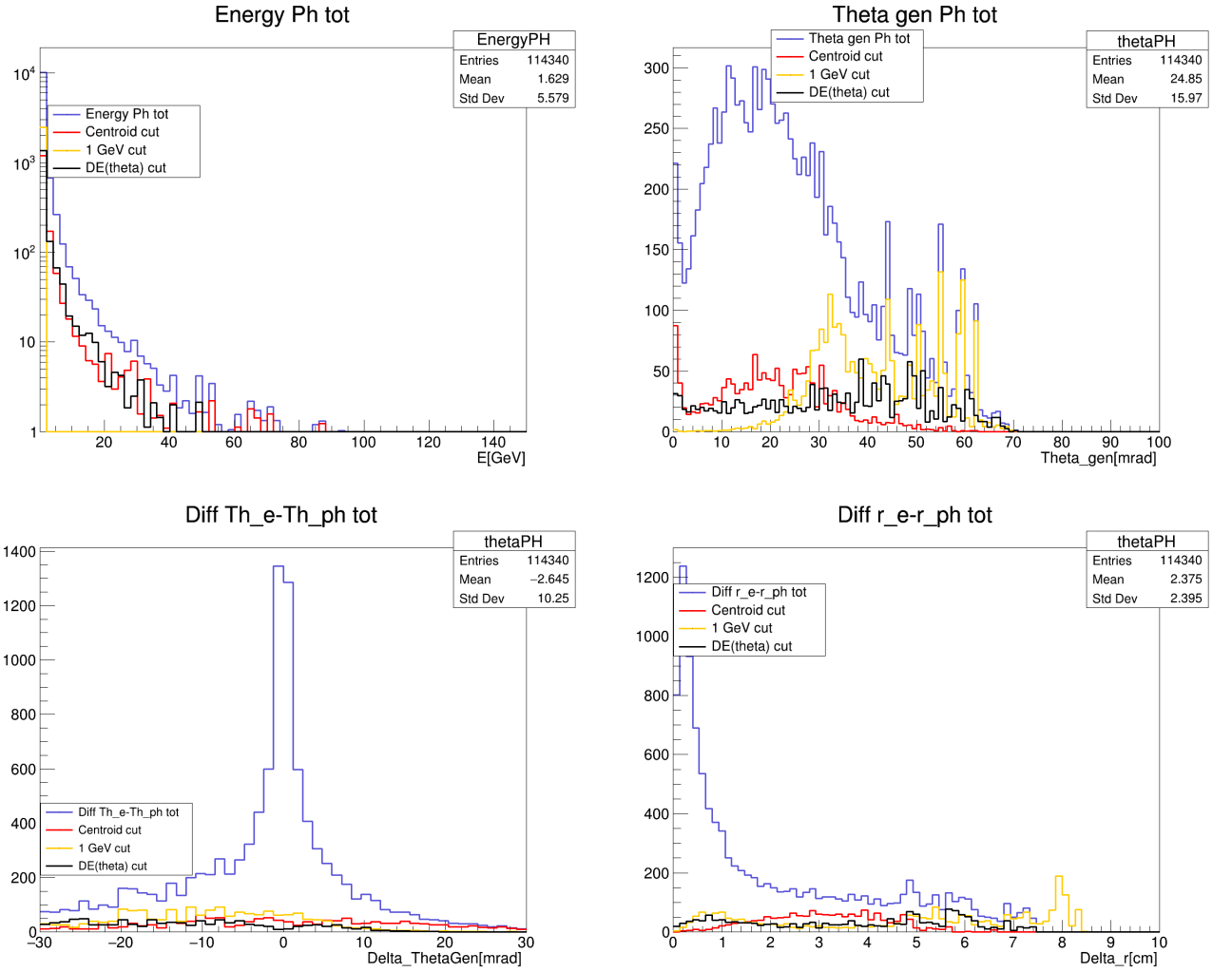
Figure 5.16: MC truth distributions of photon energy and generation angle on top and distance in angle and in cm from the electron on bottom. Blue histograms represent the photon distributions in events passing the fiducial cut $r_\mu < 1.7$ cm, while in yellow, black and red the events cut off by the sequential application of the cuts, respectively $E_{3\times3} > 1$ GeV, the D$E(\theta_E)$ cut and the centroid cut.
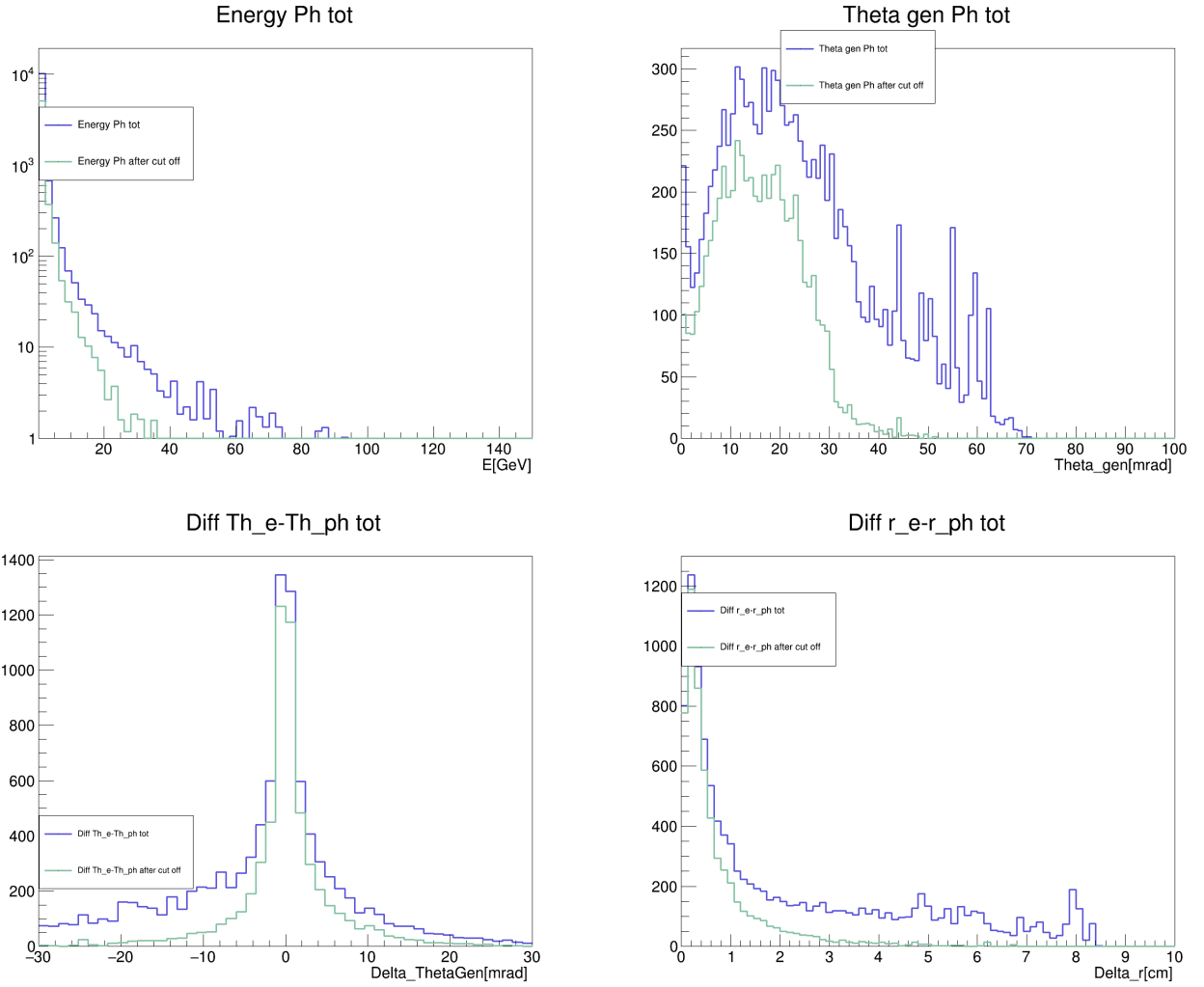
Figure 5.17: MC truth distributions of photon energy and angle on top and distance in angle and in cm from the electron on bottom. The green histograms represent the remaining events after the selection cuts, while the blue ones correspond to all the events with real photon emission.

Conclusions

The present thesis aims to evaluate the performance and possible role of the calorimeter in the MUonE Test Run planned in 2021.

A fast simulation tool has been developed on this purpose to simulate the running conditions. By considering the kinematical beam properties, already existing NLO Monte Carlo events have been processed throughout the TR2021 setup. Particles have been propagated up to the electromagnetic calorimeter surface taking into account the effects of multiple scattering in the detector material. The response of the calorimeter has been simulated by means of a fast simulation algorithm that has been developed relying on an existing parametrization also used by CMS. The validation of the algorithm has been performed comparing the simulation results to the available literature.

The fast simulation has been used then to study radiative events, which are generated together with the elastic ones.

The thesis demonstrates that radiative events can be spotted relying on three selection cuts. The first one requires the total energy measured by the calorimeter to be greater than 1 GeV. It contributes in discarding electrons with large scattering angles, which are not interesting for the analysis and are highly affected by experimental perturbations. It turns out that the majority of photons with large scattering angles are thrown away. The second cut is based on the ratio of the reconstructed energy with respect to the energy of the elastic events. An empirical fit function has been introduced to describe the RMS dependence on the energy and has been then exploited to tune the cut. This criterium allows to reject the majority of radiative events in an efficient way, either being soft or hard photons at any distance from the electron cluster.

The last selection cut takes into account the position of the shower centroid provided by the calorimeter. It acts on the distance between the centroid of the shower and the electron position extrapolated to the calorimeter surface using tracker information. The resolution on the impact point has been fitted with an empirical fit function, used to tune the cut values. This last criterium reveals to be very selective against hard photons, which, in some cases, may contribute to the electromagnetic shower more than the electrons themselves.

The thesis proves that the calorimeter can play a fundamental role in the MUonE data analysis, in particular in the Test Run 2021, allowing to select elastic events with high

efficiency, just relying on the information it can provide. It is an important result since the tracking reconstruction can be then applied to the restricted sample of the elastic candidates.

Appendices

Appendix A

Constants and Formulae

A.1 Homogeneous Media

A.1.1 Average longitudinal profiles

$$
\begin{aligned}
T_{hom} &= \ln y - 0.858 \\
\alpha_{hom} &= 0.21 + (0.492 + 2.38/Z) \ln y
\end{aligned}
\tag{A.1}
$$

A.1.2 Fluctuated longitudinal profiles

$$
\begin{aligned}
\langle \ln T_{hom} \rangle &= \ln(\ln y - 0.812) \\
\sigma\left(\ln T_{hom}\right) &= (-1.4 + 1.26 \ln y)^{-1} \\
\langle \ln \alpha_{hom} \rangle &= \ln(0.81 + (0.458 + 2.26/Z) \ln y) \\
\sigma(\ln \alpha_{hom}) &= (-0.58 + 0.86 \ln y)^{-1} \\
\rho(\ln T, \ln \alpha_{hom}) &= 0.705 - 0.023 \ln y
\end{aligned}
\tag{A.2}
$$

A.1.3 Average radial profiles

$$
\begin{aligned}
R_{C,hom}(\tau) &= z_1 + z_2 \tau \\
R_{T,hom}(\tau) &= k_1(e^{k_3(\tau - k_2)} + e^{k_4(\tau - k_2)}) \\
p_{hom}(\tau) &= p_1 e^{\frac{p_2 - \tau}{p_3} - e^{\frac{p_2 - \tau}{p_3}}}
\end{aligned}
\tag{A.3}
$$

with

$$z_1 = 0.0251 + 0.00319 \ln E$$
$$z_2 = 0.1162 + -0.000381Z$$
$$k_1 = 0.659 + -0.00309Z$$
$$k_2 = 0.645$$
$$k_3 = -2.59 \qquad \text{(A.4)}$$
$$k_4 = 0.3585 + 0.0421 \ln E$$
$$p_1 = 2.632 + -0.00094Z$$
$$p_2 = 0.401 + 0.00187Z$$
$$p_3 = 1.313 + -0.0686 \ln E$$

A.1.4 Fluctuated radial profiles

$$\tau_i = \frac{t}{\langle t \rangle_i} \frac{e^{\langle \ln \alpha \rangle}}{e^{\langle \ln \alpha \rangle} - 1}$$
$$N_{Spot} = 93 \ln(Z) E^{0.876} \qquad \text{(A.5)}$$
$$T_{Spot} = T_{hom}(0.698 + 0.00212Z)$$
$$\alpha_{Spot} = \alpha_{hom}(0.639 + 0.00334Z)$$

Appendix B

Detailed CMS Algorithm

Several modification have been done to the CMS Algorithm, presented in the next pages, in order to work in the MUonE code. As an example, the geometry class was adapted to a rectangular shape calorimeter of 25 crystals. The RawParticles class or gammaFunctionGenerator classes were modified in order to fit with our code. Many functions have been redefined as in the CMS version called methods where spread all over the CMS Fast Simulation composed by hundreds of files.

In addition, CMS has different steps in the detector: 2 preshowers, an EM calorimeter and an hadronic one. Therefore, all the additional steps different from the EM calorimeter have been cut off.

Algorithm

This algorithm which i am going to describe is needed for the understanding of how the energy of a particle (electron, positron or photon) impinging and showering in the calorimeter spreads inside its crystals.

The CMS class is the **EMShower** in which all the parameters needed for the evaluation of the individual shower profiles are defined; the two main methods in the class are:

1. PrepareSteps: it defines the steps for the integration of the longitudinal profiles, preparing the energy's slices step by step, before the real computation;

2. compute: given the longitudinal slices, placed at a certain depth in the calorimeter, it evaluates shower's longitudinal and lateral development through the definition of $N_s(t)$ energy spots per slice, which are randomly distributed on the radial profile. As a result, it collocates the energy spots in the calorimeter, giving the total energy deposited.

The showers are the individual profiles, hence fluctuations are taken into account in the algorithm.

EMShower

```
EMShower::EMShower(const RandomEngineAndDistribution* engine,
                   GammaFunctionGenerator* gamma,
                   EMECALShowerParametrization* const myParam,
                   vector<const RawParticle*>* const myPart,
                   EcalHitMaker* const myGrid,
                   PreshowerHitMaker* const myPresh,
                   bool bFixedLength)

    : theParam(myParam),
```

↪ Shower's parameters from EMECALShowerParametrization.h;

```
        thePart(myPart),
```

↪ Particles showering inside the calorimeter (electron if the starting particle is the electron, electron and positron if the starting particle is the photon);

```
        theGrid(myGrid),
```

↪ Set up for the calorimeter's geometry;

```
        thePreshower(myPresh),
        random(engine),
        myGammaGenerator(gamma),
        bFixedLength_(bFixedLength)
```

$\hookrightarrow$ Boolean variable which define how to prepare the steps: if **False** the overall ECAL length is divided into steps of $5\,\chi_0$, if **True** the steps are made $1\,\chi_0$ per $1\,\chi_0$. A for cycle is made on all the showering particles (1 or 2) in the calorimeter:

```
for (unsigned int i = 0; i < nPart; ++i) {
    // The particle and the shower energy

    Etot.push_back(0.);
    E.push_back(((*thePart)[i])->e());
    totalEnergy += E[i];

    double lny = std::log(E[i] / theECAL->criticalEnergy());
```

All the parameters for the evaluation of the longitudinal and lateral profiles depend on the impact energy of each individual particle, hence from the definition of $\ln y = \frac{E_i}{E_C}$ all the useful parameters are defined: $<T>$, $<\alpha>$, $<\ln T>$, $<\ln \alpha>$, $\sigma \ln T$, $\sigma \ln \alpha$, ρ, N_{spots}. Fluctuations start to be accounted and enters in the definition of some parameters in this way:

```
    // The longitudinal shower development parameters
    //   embedding fluctuations of alpha, T and beta

    double z1 = 0.;
    double z2 = 0.;
[...]
        z1 = random->gaussShoot(0., 1.);
        z2 = random->gaussShoot(0., 1.);
```

remembering that:

$$\begin{pmatrix} \ln T_i \\ \ln \alpha_i \end{pmatrix} = \begin{pmatrix} <\ln T> \\ <\ln \alpha> \end{pmatrix} + C \begin{pmatrix} z_1 \\ z_2 \end{pmatrix} \tag{1}$$

which defines the development of the lateral shower profile

$$f_i(t) = \frac{(\beta_i t)^{\alpha_i - 1}\, \beta_i\, e^{(\beta_i t)}}{\Gamma(\alpha_i)} \tag{2}$$

where $\beta_i = (\alpha_i - 1)/T_i$.
Also the parameters needed for the definition of the energy spots per longitudinal step t are defined:

```
    // The parameters for the number of energy spots
    TSpot.push_back(theParam->meanTSpot(theMeanT));
    aSpot.push_back(theParam->meanAlphaSpot(theMeanAlpha));
    bSpot.push_back((aSpot[i] - 1.) / TSpot[i]);
```

remembering

$$N_s(t) = N_{spot} \int_{t_{j-1}}^{t_j} \frac{(\beta_{spot}t)^{\alpha_{spot}-1}\, \beta_{spot}\, e^{(\beta_{spot}t)}}{\Gamma(\alpha_{spot})}. \tag{3}$$

All the parameters are vectors which are filled up cycle by cycle with the values of the parameters which, as already mentioned, are different for each particle because of their depenence on the energy E_i.

PrepareSteps( )

This method prepares the steps which need to be made for the integration before the real computation takes place. In CMS there are 5 general steps:

- preshower layer 1: step 0;

- preshower layer 2: step 1;

- ECAL: step 2;

- HCAL: step 3;

- vfcal: step 4;

- gap: step 5.

the last two will not be considered. The main parameters which are defined are:

```
double dt;
```

↪ length of the step;

```
double radlen;
```

↪ length of the detector in radiation length;

```
int stps;
```

↪ number of steps

```
  int first_Ecal_step = 0;
  int last_Ecal_step = 0;
// The maximum is in principe 8 (with 5X0 steps in the ECAL)
steps.reserve(24);

 [...]

  radlen = -theGrid->x0DepthOffset();

  // Preshower Layer 1
  radlen += theGrid->ps1TotalX0();
  if (radlen > 0.) {
    steps.push_back(Step(0, radlen));
    radlen = 0.;
  }

  // Preshower Layer 2
  radlen += theGrid->ps2TotalX0();
  if (radlen > 0.) {
    steps.push_back(Step(1, radlen));
    radlen = 0.;
  }

  // add a step between preshower and ee
  radlen += theGrid->ps2eeTotalX0();
  if (radlen > 0.) {
    steps.push_back(Step(5, radlen));
```

```
        radlen = 0.;
    }
```

As it can be seen, *radlen* is the total lengths in χ_0 of the different detectors. The vector *steps* is filled up with all of these.

```
// ECAL
radlen += theGrid->ecalTotalX0();
```

Now the boolean variable *bFixedLength_* is taken into account:

```
if (radlen > 0.) {
```

If *bFixedLength_*= **False**, the ECAL step is divided into N steps=*stps* of 5 χ_0

```
    if (!bFixedLength_) {
        stps = (int)((radlen + 2.5) / 5.); //
        if (stps == 0)
            stps = 1;
```

The width of the step is given by *dt*

```
        dt = radlen / (double)stps;
        Step step(2, dt);
        first_Ecal_step = steps.size();
```

for each step in the calorimeter ($N = stps$), the vector *steps* is filled up with the *for* cycle below. The steps in *steps* which represent the first and last ones in the calorimeter are registered.

```
        for (int ist = 0; ist < stps; ++ist)
            steps.push_back(step);
        last_Ecal_step = steps.size() - 1;
        radlen = 0.;
    }
```

If *bFixedLength_*= **True**, the ECAL step is divided into N steps *stps* of one χ_0

```
    else {
        dt = 1.0;
        stps = static_cast<int>(radlen); //
        if (stps == 0)
            stps = 1;
        Step step(2, dt);
        first_Ecal_step = steps.size();
        for (int ist = 0; ist < stps; ++ist)
            steps.push_back(step);
```

Now the last step is given by the fact that radlen is not integer hence it can remain a final ECAL part, which is covered by the last step with width *dt*:

```
        dt = radlen - stps;
        if (dt > 0) {
            Step stepLast(2, dt);
            steps.push_back(stepLast);
        }
        last_Ecal_step = steps.size() - 1;
```

```
        radlen = 0.;
    }
  }
```

Now that the steps have been prepared, each one need to include the fraction of the energy which is deposited in this longitudinal slice (*ESliceTot*) and the center of gravity (*MeanDepth*) of each slice, both are respectively pushed in *depositedEnergy* and *meanDepth*.

```
  nSteps = steps.size();
  if (nSteps == 0)
    return;
  double ESliceTot = 0.;
  double MeanDepth = 0.;
  depositedEnergy.resize(nSteps);
  meanDepth.resize(nSteps);
  double t = 0.;
```

At each step of the overall length t, a for cycle on the number of particle *nPart* is made, in which the method *deposit* is called for the evaluation of the deposited energy and the mean depth in each slice. The variable *realTotalEnergy* is the sum up of the energy released by all the particles in this step.

```
  int offset = 0;
  for (unsigned iStep = 0; iStep < nSteps; ++iStep) {
    ESliceTot = 0.;
    MeanDepth = 0.;
    double realTotalEnergy = 0;
    dt = steps[iStep].second;
    t += dt;
    for (unsigned int i = 0; i < nPart; ++i) {
      depositedEnergy[iStep].push_back(deposit(t, a[i],
        b[i], dt));
      ESliceTot += depositedEnergy[iStep][i];
      MeanDepth += deposit(t, a[i] + 1., b[i], dt) / b[i] * a[i];
      realTotalEnergy += depositedEnergy[iStep][i] * E[i];
    }
```

The method *deposit* is defined as

```
 {
  myIncompleteGamma.a().setValue(a);
  double b1 = b * (t - dt);
  double b2 = b * t;
  double result = 0.;
  double rb1 = (b1 != 0.) ? myIncompleteGamma(b1) : 0.;
  double rb2 = (b2 != 0.) ? myIncompleteGamma(b2) : 0.;
  result = (rb2 - rb1);
  return result;
}
```

where *myIncompleteGamma* is a function defined as

$$\int_0^x \frac{t^{\alpha-1} e^{-t}}{\Gamma\alpha} dt \tag{4}$$

and represents the integration needed for the evaluation of the energy $dE(t)$ deposited in the region $(t; t + dt)$. From the paper it results:

$$dE(t) = E_i \int_{t_{j-1}}^{t_j} \frac{(\beta_i t)^{\alpha_i - 1} \beta_i\, e^{(\beta_i t)}}{\Gamma(\alpha_i)}. \tag{5}$$

```
    if (ESliceTot > 0.)
      MeanDepth /= ESliceTot;
```

which represents $< t > = \frac{\alpha}{\beta}$.

```
    else
      MeanDepth = t - dt;

    meanDepth[iStep] = MeanDepth;
  [...]
  }
  [...]
  stepsCalculated = true;
}
```

The boolean variable *stepsCalculated* needs to be **True** in order to enable the method *compute*(), needed for the final computation of the longitudinal and lateral profile.

compute( )

```
void EMShower::compute() {
  double t = 0.;
  double dt = 0.;
  if (!stepsCalculated)
    prepareSteps();
```

EcalHitMaker is a class which permits the creation and addition of the hit in the geometry of the detector. It collocates the hit in a given region and with a given energy. The element *theGrid* belongs to this class, hence represents the geometry of the calorimeter.

```
  // Prepare the grids in EcalHitMaker
[...]
  bool status = false;

  // Loop over all segments for the longitudinal development
  double totECalc = 0;

  for (unsigned iStep = 0; iStep < nSteps; ++iStep) {
    // The length of the shower in this segment
    dt = steps[iStep].second;

    // The elapsed length
    t += dt;

    // In what detector are we ?
    unsigned detector = steps[iStep].first;
```

The following indicators are the ones defined in the previous section, hence those are the numbers of the step related to the different detectors.

```
    bool presh1 = detector == 0;
    bool presh2 = detector == 1;
    bool ecal = detector == 2;
    bool hcal = detector == 3;
    bool vfcal = detector == 4;
    bool gap = detector == 5;
[...]
```

What is done now is to identify at which depth the energy of the slice will be deposited, the variable which is used to govern this settlement is the boolean *usePreviousGrid*, it is **True** if the amount of energy released in the slice is lower than 1 MeV. Therefore, if it is **False**, the particle is energetic enough to release the energy in the grid at the depth *tt*. In this case, the boolean variable *status* is switched to **True** through the call of the method *getPads* belonging to the class *EcalHitMaker*.

getPads is defined as

```
// if it 's not possible to go at such a depth, the result is
false bool getPads(double depth, bool inCm = false);
```

and it is true when at the depth *depth* is it possible to release the energy. The depth at which the energy is released is the one defined in the previous section for each step as *meanDepth*.

```
    // Build the grid of crystals at this ECAL depth
    // Actually, it might be useful to check if this grid is
    // empty or not. If it is empty (because no crystal
    // at this depth), it is of no use (and time
    // consuming) to generate the spots

    // middle of the step
    double tt = t - 0.5 * dt;

    double realTotalEnergy = 0.;
    for (unsigned int i = 0; i < nPart; ++i) {
      realTotalEnergy += depositedEnergy[iStep][i] * E[i];
    }

    // If the amount of energy is greater than 1 MeV, new grid
    // otherwise put in the previous one.
    bool usePreviousGrid = (realTotalEnergy < 0.001);

    // If the amount of energy is greater than 1 MeV, new grid
    // otherwise put in the previous one.

    // If less than 1 kEV. Just skip
    if (iStep > 2 && realTotalEnergy < 0.000001)
      continue;

    if (ecal && !usePreviousGrid) {
      status = theGrid->getPads(meanDepth[iStep]);
    }
    [...]
```

It is important to highlight that now no energy is collocated in any place of the grid, it is just a way to understand until which depth the shower keeps on showering. If the energy is lower than 1 keV, the cycle is skipped and directly jumps to the beginning of the loop for next iteration (hence to the next step).

Now, it is evaluated the energy deposited, recalling the one evaluated with the method *PrepareSteps( )*.

```
    // The particles of the shower are processed in parallel
    for (unsigned int i = 0; i < nPart; ++i) {

        //  integration of the shower profile between t−dt and t
        double dE = (!hcal) ? depositedEnergy[iStep][i] :
                        1. − deposit(a[i], b[i], t − dt);

// no need to do the full machinery if nothing to distribute)
        if (dE ∗ E[i] < 0.000001)
            continue;
```

Fluctuations of the energy deposited are taken into account, its value is extracted randomly from a gaussian centered in *dE*:

```
        if (ecal && !theECAL−>isHom()) {
            double mean = dE ∗ E[i];
            double sigma = theECAL−>resE() ∗ sqrt(mean);

            double dE0 = dE;

            dE = random−>gaussShoot(mean, sigma) / E[i];

            if (dE ∗ E[i] < 0.000001)
                continue;
            photos[i] = photos[i] ∗ dE / dE0;
        }
         totECalc += dE;

        // The number of energy spots (or mips)
        double nS = 0;
```

Here also the fluctuations related to photostatistics in the shower are taken into account:

```
// ECAL: Account for photostatistics and long'al non−uniformity
        if (ecal) {
            dE = random−>poissonShoot(dE ∗ photos[i]) / photos[i];
            double z0 = random−>gaussShoot(0., 1.);
            dE ∗= 1. + z0 ∗ theECAL−>lightCollectionUniformity();
```

The number of spots is now evaluated with the usage of Eq. (3):

```
            // Expected spot number
            nS = (theNumberOfSpots[i] ∗ gam(bSpot[i] ∗ tt,
            aSpot[i]) ∗ bSpot[i] ∗ dt / tgamma(aSpot[i]));

        } else if (hcal) { [...]
```

```
    } else if (presh1) { [...]
    } else if (presh2) { [...]
    }   [...]
```

Each spot as an energy defined as $E_s = dE(t)/Ns(t)$, hence it is fixed for each spot (NB: dE is the fraction of energy from *depositedEnergy*, thus $dE(t) = dE \times E_i$).

```
// The lateral development parameters

    // Energy of the spots
    double eSpot = (nS > 0.) ? dE / nS : 0.;
    double SpotEnergy = eSpot * E[i];
[...]
    int nSpot = (int)(nS + 0.5);
```

The lateral development is represented by the equation

$$f_i(r) = p_i \frac{2R_{Ci}^2 r}{(r^2 + R_{Ci}^2)^2} + (1 - p_i) \frac{2R_{Ti}^2 r}{(r^2 + R_{Ti}^2)^2} \tag{6}$$

where all the parameters are defined in EMECALShowerParametrization.h and are functions of τ_i and E_i.

```
    double taui = tt / Ti[i];
    double proba = theParam->p(taui, E[i]);
    double theRC = theParam->rC(taui, E[i]);
    double theRT = theParam->rT(taui, E[i]);
```

Once we have the longituginal step computed and, in each longitudinal step, a given number of spots with a given energy, it is necessary to distribute these spots radially in a random way such that radial fluctuations are accounted. The way through which they manage to do that is to divide in two sets the number of spots per slice: one set in the core region and one set in the tail region. The number of spots in the core, thus in the tail, is extracted randomly by a gussian centered on $p \times N_s(t)$ where p is the weight of the core: this is the definition of *dSpotsCore* which will define *nSpots_core* and consequently *nSpots_tail* .

```
    double dSpotsCore = random->gaussShoot(proba * nSpot,
    std::sqrt(proba * (1. - proba) * nSpot));

    if (dSpotsCore < 0)
      dSpotsCore = 0;

    unsigned nSpots_core = (unsigned)(dSpotsCore + 0.5);
    unsigned nSpots_tail = ((unsigned)nSpot > nSpots_core) ?
    nSpot - nSpots_core : 0;
```

Let's now cycle on a variable *icomp* which assumes two values:

- 0, and represents the core;

- 1, and represents the tail.

For each case, an object of the class *RadialInterval* is defined: it is an interval in the radial direction, of width R, with $N = ncompspots$ as the number of spots which it contains, of energy *SpotEnergy*.

9

```
    for (unsigned icomp = 0; icomp < 2; ++icomp) {
      double theR = (icomp == 0) ? theRC : theRT;
      unsigned ncompspots = (icomp == 0) ?
      nSpots_core : nSpots_tail;

      RadialInterval radInterval(theR, ncompspots,
      SpotEnergy, random);
            if (ecal) {
        if (icomp == 0) {
          setIntervals(icomp, radInterval);
        } else {
          setIntervals(icomp, radInterval);
        }
      }
      [...]
```

Now the method *setInterval* is called, it is defined as

```
{ const std::vector<double>& myValues((icomp) ?
    theParam−>getTailIntervals() : theParam−>getCoreIntervals());

  unsigned nvals = myValues.size() / 2;
```

where *nvals* is 1 (hence nvals=0) for the Core and 2 (hence nvals=0,1) for the Tail, it represents the different regions which compose the two radial profiles. Now a cycle on these regions is made:

```
  {
    rad.addInterval(myValues[2 * iv], myValues[2 * iv + 1]);
  }
}
```

where again another method of the class *RadialInterval* is called: *addInterval*. The variables which it needs are

which are the radius of the internal interval taken into account and the percentage of spots in this specific region of the radial profile.
To sum up:

1. there are two radial intervals 1) the tail ($icomp = 0$), 2) the core ($icomp = 1$);

2. for each radial interval the method *setIntervals* is called: it defines in how many regions the radial interval (core or tail) is divided. The Core has just one region ($iv = 0$), while the Tail has two regions ($iv = 0, 1$) which are (definition in Calorimetry_cff.py): i) where $r < 1 \times R_{Moliere}$ and ii) where $r > 1 \times R_{Moliere}$. Hence here the method *addInterval* plays this rule of dividing internally the radial interval.

```
      radInterval.compute();
      // irad = 0 : central circle; irad=1 : outside

      unsigned nrad = radInterval.nIntervals();
```

with $nrad = 1$ for the Core and $nrad = 2$ for the Tail. The energy of the spots in the internal interval is extrpolated through *getSpotEnergy* and added at the given depth tt in the Grid which represents the ECAL.

```
          for (unsigned irad = 0; irad < nrad; ++irad) {
            double spote = radInterval.getSpotEnergy(irad);
            if (ecal)
              theGrid->setSpotEnergy(spote);
          [...]
```

Now the distribution of the $N_{spots}(t)$ at a given depth need to be done, the maximum and minimum extremities of the internal interval are taken and used for the definition of z_3: a random number which enable the definition of the position r_i where the spot will be placed. Once that *phi* is randomly extrapolated too, the coordinates of all the energy spots are assigned through the *for* cycle on the number of spots in the internal interval.

```
          unsigned nradspots = radInterval.getNumberOfSpots(irad);
          double umin = radInterval.getUmin(irad);
          double umax = radInterval.getUmax(irad);

          // Go for the lateral development
          for (unsigned ispot = 0; ispot < nradspots; ++ispot) {
            double z3 = random->flatShoot(umin, umax);
            double ri = theR * std::sqrt(z3 / (1. - z3));

            // Generate phi
            double phi = 2. * M_PI * random->flatShoot();
```

Only now the hit is added in the calorimetry geometry, given the precise coordinates:

```
          // Add the hit of each Nspot in the crystal
          if (ecal) {
          theGrid->addHit(ri, phi);
          }
            [...]
```

For each spot of the internal interval there is the energy *spote*. *Etot* defines the energy in all the Radial Interval (tail or core), as it is included in the *for* cycle made on *nrad*, deposited by the particle i at the depth i.

```
            Etot[i] += spote;
          } // finish cycle on ispot
        } // finish cycle on irad
      } // finish cycle on icomp
    } // finish cycle on nPart
  } // finish cycle on nSteps
  double Etotal = 0.;
  for (unsigned i = 0; i < nPart; ++i) {
    Etotal += Etot[i];
  }
}
```

where *Etotal* is the total energy which all the *nPart* release inside all the calorimeter, as is cycled on the number of steps *nSteps*.

This object EMShower and the method compute() are called in the file CalorimetryManager.cc, where, for each event, the hit are simulated and extrapolated from the Grid.

Bibliography

[1] S.H. Neddermeyer, and C.D. Anderson; *Note on the Nature of Cosmic-Ray Particles*, Phys. Rev. 51 (**1937**) 884, `https://doi.org/10.1103/PhysRev.51.884`

[2] J.C. Street, and E.C. Stevenson; *New Evidence for the Existence of a Particle of Mass Intermediate Between the Proton and Electrons*, Phys. Rev. 52 (**1937**) 1003, `https://doi.org/10.1103/PhysRev.52.1003`

[3] J.M. Conversi, E. Pancini, O.Piccioni ; *On the Disintegration of Negative Mesons*, Phys. Rev. 71 (**1947**) 209, `https://doi.org/10.1103/PhysRev.71.209`

[4] C. Latters, H. Muirhead, G. Occhialini et al. ; *Process Involving Charged Mesons*, Nature 159 (**1947**) 694?697, `https://doi.org/10.1038/159694a0`

[5] G. Uhlenbeck and S. Goudsmit ; *Spinning Electrons and the Structure of Spectra*, Nature 117 (**1926**) 264?265, `https://doi.org/10.1038/117264a0`

[6] W. Gerlach, O. Stern; *Der experimentelle Nachweis des magnetischen Moments des Silberatoms*, Zeitschrift fr Physik 8 (**1922**) 110-111, `https://doi.org/10.1007/BF01329580`

[7] P.A.M. Dirac; *The quantum theory of the electron*, Royal Society 117 (**1928**) 778

[8] J. Shwinger; *On Quantum-Electrodynamics and the Magnetic Moment of the Electron*, Phys. Rev. 73 (**1947**) 516, `https://doi.org/10.1103/PhysRev.73.416`

[9] P. Kusch and H. M. Foley; *The Magnetic Moment of the Electron*, Phys. Rev. 74 (**1948**) 250, `https://doi.org/10.1103/PhysRev.74.250`

[10] F. Jegerlehner and A. Nyffeler, *The Muon g-2*, Phys. Rept. 477 (**2009**) 1, [`arXiv:0902.3360`].

[11] P.A. Zyla; *Particle Data Group*, Prog. Theor. Exp. Phys. (**2020**) no.8, 083C01, `https://doi:10.1093/ptep/ptaa104`

[12] D. Hanneke, S. Fogwell, G. Gabrielse, *New Measurement of the Electron Magnetic Moment and the Fine Structure Constant* Phys. Rev. Lett. 100 (**2008**), 120801, `https://link.aps.org/doi/10.1103/PhysRevLett.100.120801`

[13] T. Aoyama et al., *The anomalous magnetic moment of the muon in the standard model*, (**2020**) `arXiv:2006.04822`

[14] A. Keshavarzi, D. Nomura, and T. Teubner *$g - 2$ of charged leptons, $\alpha(M_Z^2)$, and the hyperfine splitting of muonium.* Phys. Rev. D 101 (**2020**) `https://link.aps.org/doi/10.1103/PhysRevD.101.014029`

[15] F.Jegerlehner, *The Anomalous Magnetic Moment of the Muon*, Springer Tracts Mod. Phys. 274 (**2017**) 1 `https://link.springer.com/book/10.1007%2F978-3-319-63577-4`

[16] G. Colangelo, M. Hoferichter, M. Procura and P. Stoffer *Hadronic light-by-light scattering and the muon $g - 2$* Nuovo Cim.C 38 (**2016**) 4, 135 `https://doi:10.1393/ncc/i2015-15135-9`

[17] F. Jegerlehner *The Muon g-2 in Progress* Acta Physica Polonica Series B 49 (**2018**) 6 `https://arxiv.org/abs/1804.07409`

[18] Muon $(g - 2)$Collaboration *Final Report of the Muon E821 Anomalous Magnetic Moment Measurement at BNL* Phys. Rev. D 73 (**2006**) `https://arxiv.org/pdf/hep-ex/0602035.pdf`

[19] A. T. Fienberg (for the Muon $g - 2$ Collaboration) *The Status and Prospects of the Muon $g - 2$ Experiment at Fermilab* FERMILAB-CONF-19-207-E (**2019**) pag. $163 - 166$ `https://arxiv.org/abs/1905.05318v1`

[20] M. Abe et al., *A New Approach for Measuring the Muon Anomalous Magnetic Moment and Electric Dipole Moment* Prog. Theor. Exp. Phys. (**2015**) `https://arxiv.org/pdf/1901.03047.pdf`

[21] A. Keshavarzi, M. Passera, W. J. Marciano and A. Sirlin; *Muon $g - 2$ and $\Delta\alpha$ connection*, Phys. Rev. D 102 (**2020**) no.3, 033002 `https://link.aps.org/doi/10.1103/PhysRevD.102.033002`

[22] Sz. Borsanyi, Z. Fodor, J. N. Guenther, C. Hoelbling, S. D. Katz, L. Lellouch, T. Lippert, K. Miura, L. Parato, K. K. Szabo, F. Stokes, B. C. Toth, Cs. Torok, L. Varnhorst; *Leading hadronic contribution to the muon magnetic moment from lattice QCD*, (**2020**), `https://arxiv.org/abs/2002.12347`

[23] A. Crivellin, M. Hoferichter, C. Andrea Manzari and M. Montull; *Hadronic vacuum polarization: $(g?2)_\mu$ versus global electroweak fits*, Phys. Rev. Lett. 125, (**2020**) 091801 https://arxiv.org/abs/2003.04886

M. Passera, W. J. Marciano and A. Sirlin, *The muon g-2 discrepancy: errors or new physics?* AIP Conference Proceedings 1078, 378?381 (**2008**). https://arxiv.org/pdf/0809.4062.pdf

[24] C.M. Carloni Calame, M. Passera, L. Trentadue, G. Venanzoni *A new approach to evaluate the leading hadronic corrections to the muon $g - 2$*, Physics Letters B, Vol. 746, (**2015**), Pag. 325-329 https://doi.org/10.1016/j.physletb.2015.05.020

[25] G. Abbiendi et al., *Letter Of Intent: The MUonE Project*, CERN-SPSC-2019-026 (**2019**), https://cds.cern.ch/record/2677471

[26] G. Abbiendi et al. [OPAL Collaboration], *Measurement of the running of the QED couplingin small-angle Bhabha scattering at LEP*, Eur. Phys. J. C 45 (**2006**) 1, https://doi.org/10.1140/epjc/s2005-02389-3

[27] G. Abbiendi et al., *Measuring the leading hadronic contribution to the muon g-2 via μe scattering*, Eur. Phys. J. C 77 (**2017**) 139, https://doi.org/10.1140/epjc/s10052-017-4633-z

[28] M. Alacevich, C. M. Carloni Calame, M. Chiesa, G. Montagna, O. Nicrosini and F. Piccinini, *Muon-electron scattering at NLO*, JHEP 02 (**2019**) 155 https://arxiv.org/pdf/1811.06743.pdf.

[29] M. Fael and M. Passera, *Muon-Electron Scattering at Next-To-Next-To-Leading Order: The Hadronic Corrections*, Phys. Rev. Lett. 122 (**2019**) 192001 https://amslaurea.unibo.it/14194/1/tesi_magistrale_Luca_Pagani.pdf.

[30] L. Pagani, *A new approach to muon g-2 with space-like data: analysis and fitting procedure*, Master Degree in Physics (**2017**) University of Bologna https://journals.aps.org/prl/pdf/10.1103/PhysRevLett.122.192001.

[31] P. Banerjee, C. M. Carloni Calame, M. Chiesa, S. Di Vita, T. Engel, M. Fael, S. Laporta, P. Mastrolia, G. Montagna, O. Nicrosini, G. Ossola, M. Passera, F. Piccinini, A. Primo, J. Ronca, A. Signer, W. J. Torres Bobadilla, L. Trentadue, Y. Ulrich and G. Venanzoni , *Theory for muon-electron scattering @ 10 ppm*, The European Physical Journal C volume 80, (**2020**) 591 DOI:https://doi.org/10.1140/epjc/s10052-020-8138-9.

[32] Pierpaolo Mastrolia, Massimo Passera, Amedeo Primo and Ulrich Schubert, *Master integrals for the NNLO virtual corrections to ?e scattering in QED: the planar*

graphs, Journal of High Energy Physics, (**2017**) 198 DOI:`https://doi.org/10.1007/JHEP11(2017)198`.

[33] P. Mastrolia, M. Passera, A. Primo, U. Schubert and W. J. Torres Bobadilla *On µe-scattering at NNLO in QED*, EPJ Web of Conferences 179, (**2018**) 01014 DOI:`https://doi.org/10.1051/epjconf/201817901014`.

[34] Stefano Di Vita, Stefano Laporta, Pierpaolo Mastrolia, Amedeo Primo and Ulrich Schubert *Master integrals for the NNLO virtual corrections to ?e scattering in QED: the non-planar graphs*, Journal of High Energy Physics, 16 (**2018**) DOI:`https://doi.org/10.1007/JHEP09(2018)016`.

[35] H. A. Bethe, *Moliére's Theory of Multiple Scattering*, Phys. Rev. 89, (**1953**) p. 1256, `https://link.aps.org/doi/10.1103/PhysRev.89.1256`

[36] G. Grindhammer, M. Rudowicz and S. Peters, *The Fast Simulation of Electromagnetic and Hadronic Showers*, Nucl. Instrum. Meth. A 290 (**1989**) p. 469, `https://doi.org/10.1016/0168-9002(90)90566-O`

[37] G. Grindhammer and S. Peters, *The Parameterized Simulation of Electromagnetic Showers in Homogeneous and Sampling Calorimeters*, International Conference on Monte Carlo Simulation in High-Energy and Nuclear Physics - MC 1993 `https://arxiv.org/abs/hep-ex/0001020`

[38] T.C. Awes, F.E. Obenshain, F. Plasil, S. Saini, S.P. Sorensen and G.R. Young *A simple method of shower localization and identification in laterally segmented calorimeters*, Nuclear Instruments and Methods in Physics Research Section A: Accelerators, Spectrometers, Detectors and Associated Equipment, Vol. 311, Issues $1-2$ (**1992**), Pages 130-138,`https://doi.org/10.1016/0168-9002(92)90858-2`

Ringraziamenti

Da quando ho cominciato la magistrale, ho atteso con ansia ed entusiasmo il periodo di tesi. Mi immaginavo un momento pieno di fermento, la possibilità di andare per qualche settimana in un laboratorio e toccare con mano l'ambiente della ricerca, conoscere gente nuova, dialogare e confrontarsi, sulla fisica e chissà che altro. Ma sappiamo tutti com'è andato quest'anno e come la maggior parte di queste aspettative non abbiano retto il confronto con la realtà.
Sicuramente è stato diverso, seduta alla mia scrivania nei peggiori momenti o in biblioteca quando le restrizioni ce lo permettevano, quasi fosse un esame come tanti. Tantissime volte mi sono abbattuta pensando a come sarebbe potuto essere e come invece è stato, ma ora posso guardarmi indietro e rendermi conto di come invece abbia imparato cose nuove e avuto occasioni, anche se in modo diverso, di dialogo e confronto.

Nel fare ciò, non posso non ringraziare Giovanni Abbiendi e Umberto Marconi. Mi hanno seguita dal primo all'ultimissimo momento, con attenzione, umanità e una disponibilità davvero non comune. Hanno sempre preso sul serio ogni mia considerazione, senza farmi mai sentire inadeguata anche quando dicevo o facevo sciocchezze (e ne ho dette e fatte). Li ringrazio per avermi insegnato ad approcciare certi problemi, ad osservare il dato, farmi domande e trarre conclusioni. In più è stato certamente stimolante poter partecipare ai meeting settimanali di MUonE e aver, nel mio piccolo (piccolissimo), dato un contributo. È sicuramente una proposta affascinante e che richiede delle attenzioni al particolare non banali. Chissà forse in un futuro potrò assistere a come tutto questo andrà a finire e scoprire se davvero il calorimetro sarà importante..
Ad ogni modo, per questo e altro provo una sincera gratitudine e spero di poter aver presto un'occasione d'incontro non dietro ad un computer o una mascherina..!
Ringrazio anche Il prof. Domenico Galli per le correzioni estetiche che il mio essere frettolosa mi avrebbe fatto trascurare.

Sono stati anni incredibili, non voglio essere lunga (so già che lo sarei) ma ho in mente almeno un centinaio di volti che in questi anni mi hanno accompagnata, dal caffè alla macchinetta (decisamente peggiorato negli anni), alle studiate infinite in acquario o ai pranzi sotto il caro Augusto. È anche grazie a questo ambiente che l'entusiasmo per la

fisica e per la ricerca hanno preso posto in me. Ho in particolare in mente Anna, Rebecca, e poi Valentina, Sara e Maria Vittoria; tutte persone con cui ho potuto condividere ogni cosa di questo lungo percorso. Alle mie tre compagne di magistrale, ringrazio per le avventure e il supporto di questi ultimi anni, rimarrà sempre il ricordo di Lisbona e di come abbiamo fregato il lockdown per tre incredibili giorni. Sono sicura (o comunque lo spero vivamente) che continueranno negli anni queste nostre vacanzine tra fisiche, aspetto con ansia di mangiare con voi una pizza a Napoli.

A Rebe, che se anche siamo state lontane in questi ultimi anni, è stata parte fondamentale dei miei primi anni (in particolare terzo) di triennale; un supporto e un dialogo continuo, con momenti faticosi per entrambe, ma di grande compagnia per quel momento così particolare. Sono certa che prima o poi riusciremo a farci uno di quei giretti di cui abbiamo sempre parlato negli anni.

Ad Anna in particolare va il mio grazie, per il supporto davvero costante e affettuoso, per le chiacchierate sui temi più disparati, agli immancabili pranzi a base di riso e minestrone e per il confronto sempre vero sulle domande che abbiamo più a cuore. Abbiamo passato alti e bassi ma sono sicura che sia uno dei rapporti fondamentali che da questo momento universitario, non so in che modo e forma, continuerà nel tempo con la stessa verità.

Non posso non nominare Benfe senza cui probabilmente avrei studiato la gran parte degli esami della magistrale con un livello di precisione decisamente inferiore (classicista non mente). Anche se ci incagliavamo nei ragionamenti più metafisici, siamo sempre riusciti a cogliere il meglio di quello che studiavamo, checcè tu possa dirne..

I miei amici '96 che sono sempre stati una costante in questi anni e con cui sono cresciuta e cambiata: i confronti sui libri e sulla vita con Anto, so che prima o poi condivideremo insieme anche racconti di vita campestre.. ; i passaggi universitari importanti sempre fatti insieme a Giovo, che, anche se con alti e bassi, in questi cinque anni sei stato un compagno fondamentale; le discussioni più strane con Albi, da cui mi aspetterò sempre una domanda ingarbugliata sulla fisica ; e infine il trio del brio, che anche se negli anni ha perso un po' di briosità.., è stato una compagnia importante per l'inizio di questo percorso.

Ovviamente immancabile citare la mia compagna di opposizioni e polemiche Ale, con cui ho sempre avuto la possibilità di esprimere i miei giudizi senza sentirmi giudicata o moralizzata. Ecco, sono sempre libera di dire quello che penso, poi al massimo lei ci ride sù.

Chiadi, Ire, Elo invece sono state le tre figure femminili che in questi anni mi hanno accompagnata e accolta nei loro appa fin dai tempi della matricoletta spocchia Bolo (che non sono mai stata, potete anche ammetterlo adesso). Non sentirsi quotidianamente non vuol dire avere meno a cuore l'altro e io sono certa di questo vedendo il rapporto con voi. È sempre una gioia, dopo tanto tempo senza vederci, poter chiacchierare e dialogare, pranzare o fare una gita fuori porta insieme, con la serietà che si mischia sempre molto bene alla leggerezza.

Vorrei ricordare e nominare tutti, le Scimmiette (costante dagli ultimi anni del liceo e immancabili in ogni situazione), tutti gli amici del clu (Iddu! Cito te come rappresentanti di tutti loro, che so che altrimenti, da vero calabrese, te la legheresti al dito e chissà quando mi riparleresti amichevolmente..), le mie amiche storiche di Bologna (come le amiche del giardino Sha, Ali che grazie alla cene multietniche e pizzate mi hanno permesso di staccare ogni tanto dalla fisica e dallo studio.. o le amiche delle medie che continuo a vedere e con cui spero possa continuare, se non di più, un'amicizia), e per tutti dire una parola, ma mi dilungherei troppo (e già l'è lunga arrivar fin questa pagina..), quindi mi fermo qui. Non con meno tenerezza e affetto li ricordo.

Un grazie particolare va a Matteo, che in questi ultimi mesi mi ha pazientemente sopportata senza chiedere mai niente in cambio.

Ogni mattina in questo ultimo periodo cominciavo quasi sempre con una chiamata alla mia nonna, che a modo suo, da lontano, mi ha accompagnata in questo percorso.. quindi un grazie va anche a lei, con tanto affetto. Mentre più vicina la Croce, che con il suo pane e i taralucci accompagnavano le studiate di qualsiasi ora; grazie per tutti i pensieri che mi rivolgi.

E in ultimo, ma perchè fondamentali, ringrazio la mia famiglia. Mia mamma per motivarmi ogni volta a perseverare nei miei obiettivi e perchè non perde mai l'entusiasmo. Siamo diverse, diametralmente opposte (ancora sogno gli spaghetti che so che non mangerò oggi per festeggiare..), ma ad ogni decisione presa ho sempre sentito la necessità di chiedere consiglio a te; anche se poi spesso faccio di testa mia.. A mio papà per la passione alla conoscenza e allo studio che mi ha trasmesso. A volte cozziamo perchè siamo uguali, ma non manca mai il supporto per ogni mia decisione (a parte per i vestiti e per i pigiami..). Ed infine a mio fratello per la costante disponibilità che si rivela avere in ogni situazione. Anche se abbiamo idee diverse praticamente su tutto e spesso di tirerei volentieri un piatto in testa, non sarei sicuramente riuscita a laurearmi senza che facessi tu le faccende che assegnavano a noi figli (con faccende si esclude il lavaggio piatti, a quello ho sempre contribuito anche io, checchè ne dica il popolo di casa).
Inutile dire che senza di voi questo percorso non sarebbe stato possibile.

E come dice la poesia di Mariangela Gualtieri, la natura e le sue leggi (per quanto controverse e a volte avverse) hanno intrinseci in sé una bellezza che esiste anche senza chiederlo. È importante, di tanto in tanto, ricordarsene e lo studio della fisica rinnova e richiama alla mente questa nascosta meraviglia.